Tungsten coatings effects on hydrogen isotopes bi-directional permeation through the first wall of a magnetic fusion power reactor

XU YUE

Doctor of Philosophy

Department of Fusion Science
School of Physical Sciences
The Graduate University for Advanced Studies
(SOKENDAI)

-2017-

Abstract

Reduced activation ferritic steel alloys (RAFSs) such as F82H (Fe-8Cr-2W) are the candidate materials for the first wall of DEMO reactors. In this PhD thesis work, one of the technical issues related to hydrogen isotopes permeation through the first wall has been studied.

For the blankets employing self-cooled breeder, the first wall is supposed to be subjected to bi-directional hydrogen isotopes permeation: in one direction by edge plasma-driven permeation (PDP) of deuterium as well as tritium into blankets, and in the other direction by bred tritium gas-driven permeation (GDP) into the edge plasma. It is important to note that deuterium PDP will hinder the recovery efficiency of tritium from the breeder and will probably necessitate isotopes separation as well. On the other hand, tritium GDP, essentially the same effect as gas-puff for fueling except that it is uncontrollable, will lead to an unwanted increase of the particle recycling in the first wall region, which could even affect core confinement performance as well as isotopes mixture imbalance.

Tungsten has been proposed as a candidate plasma-facing material for the divertor of the International Thermonuclear Experimental Reactor (ITER). For a DEMO reactor, surface coatings made of tungsten are necessary to protect the plasma-facing wall made of RAFSs such as F82H. The characterization of hydrogen isotopes PDP and GDP through tungsten coated F82H is of crucial importance to evaluate major reactors design issues including tritium retention, breeding feasibility and first wall particle recycling. There is a number of experimental data of hydrogen isotopes transport and retention behavior in bulk polycrystalline tungsten. However, only limited experimental investigations aimed at understanding that for tungsten coatings. In particular, there have been no experimental studies reported on hydrogen isotopes PDP through tungsten coated RAFSs, which is important to the plasma-wall interaction studies for a DEMO reactor. In this PhD thesis research, hydrogen isotopes PDP and GDP through F82H coated with two different types of tungsten coatings, i.e., vacuum plasma-sprayed tungsten (VPS-W) and sputter-deposited

tungsten (SP-W) have been studied. The purposes of this PhD thesis research are: (1) to demonstrate experimentally the hydrogen isotopes (H/D) bi-directional permeation predicted for the first wall of a fusion power reactor, (2) to investigate tungsten coatings effects on GDP and PDP behavior, (3) to investigate the isotopic effects on hydrogen transport, and (4) to establish a fundamental database on hydrogen and deuterium transport parameters for designing the first wall of fusion power reactors.

Hydrogen isotopes (H/D) PDP and GDP through F82H has been investigated in a steady-state laboratory-scale plasma device: VEHICLE-1 under some of the reactor-relevant conditions. For PDP experiments, the plasma density is of the order of 10^{10} cm^{-3} and the electron temperature is ~5.5 eV measured by a Langmuir probe in front of the sample. The particle bombarding energy is set at -100 V by a negative DC bias applied on the membrane. Taking into account the ion species mix and surface particle reflection, the net implantation flux is estimated to be ~1×10^{16} atoms cm^{-2} s^{-1}, relevant to the first wall environment of DEMO reactors. For GDP experiments, the upstream gas pressure is in the range of 10^{3}-10^{5} Pa measured by an absolute pressure gauge. The samples made of F82H and α-Fe are prepared in the same dimensions as those commercially available conflat flanges with an outer diameter of 70 mm, except that a circular area of 35 mm in diameter inside the knife-edge is machined down to thicknesses of 0.5-2 mm. A resistive heater is set beneath the membrane and the sample temperature varies from 150 ℃ to 550 ℃.

The hydrogen transport parameters data taken for α-Fe have been found to be in good agreement with the literature data, which validates the experimental setup in VEHICLE-1 for the evaluation of other first wall candidate materials. Both the GDP and PDP data taken for F82H show thickness dependence, suggesting that hydrogen permeation through F82H is diffusion-limited. The hydrogen and deuterium transport parameters such as permeability, diffusivity, solubility and surface recombination coefficient have been successfully measured for F82H. In particular, the surface recombination coefficient of deuterium on F82H, which is essential to correctly predict the hydrogen isotopes permeation flux through the first wall, has been experimentally measured for the first time. Isotopic effects on hydrogen transport parameters have been discussed. It has been found

that the permeability and diffusivity show isotopic mass effect which is predicted by the classical rate theory relating hydrogen diffusion to the atomic jumping frequency. The solubility, however, is governed by the heat of solution, exhibits no isotopic mass effect.

Simultaneous bi-directional hydrogen isotopes (H/D) permeation has been demonstrated experimentally for the first time under controlled experimental conditions. For bi-directional permeation experiments, the thickness of F82H membrane is 0.5 mm and the membrane temperature is set at ~500 ℃. The electron temperature is raised up to ~10 eV for the improved sensitivity of H_α spectroscopy. Experiments indicate that gas-driven hydrogen permeation takes place in the counter direction of plasma-driven deuterium permeation, which then results in an unwanted increase in edge plasma density. Plasma-driven deuterium flows into hydrogen gas has been detected as well. Both the D_2 and HD partial pressures increase after an extended accumulation period of ~2 h for PDP deuterium pressure build-up, meaning that PDP deuterium flows into the hydrogen gas side.

Hydrogen isotopes GDP and PDP experiments have been performed for VPS-W and SP-W coated F82H. This is the first report of experimental studies on hydrogen PDP through tungsten coated RAFSs. The VPS-W coatings are deposited at the temperature of ~600 ℃. The average size of tungsten powder particles is ~25 μm. The thickness of VPS-W coatings used in this work varies from 40 μm to 200 μm. VPS-W coatings have an inhomogeneous microstructure, i.e., a mixture of disorganized areas composed of large unmelted tungsten particles, fine randomly melted tungsten and pores. The average density is evaluated to be ~90% of bulk polycrystalline tungsten. The coatings have been found to be porous and have an open system of connected pores. The observed hydrogen GDP flux through VPS-W coated F82H is reduced compared to that through bare F82H. The main effect of VPS-W coatings on hydrogen permeation is to reduce the incoming flux at the W/F82H interface owing to pore diffusion in the coatings and to reduce the effective surface area for hydrogen dissolution in the substrate. PDP experiments indicate that VPS-W coatings reduce PDP fluxes by more than one order of magnitude relative to that for bare F82H from 300 ℃ to 550 ℃. Reduced PDP fluxes are attributed to the complex microstructure and a substantial surface-connected porosity of the coatings.

SP-W coatings are prepared by argon ion sputtering at the temperature of ~300 ℃ and gas pressure of ~0.19 Pa. The density of SP-W coatings is evaluated to be ~99.5% of bulk polycrystalline tungsten. The thickness of SP-W coatings used in this work varies from 0.5 μm to 4 μm. The surface of SP-W coatings is well organized with an average crystal size of ~100 nm. Columnar tungsten grains are observed from the cross-section view and the W/F82H interface is sharp without voids, cracks or other visible defects. Hydrogen isotopes GDP fluxes are reduced significantly by SP-W coatings. The hydrogen and deuterium transport parameters for SP-W coatings have been evaluated by the gas permeation technique in the temperature range from 200 ℃ to 550 ℃ employing a diffusion-limited permeation model. The permeability is comparable to the literature data of bulk polycrystalline tungsten. However, the effective solubility and diffusivity are different from that of bulk polycrystalline tungsten by several orders of magnitude, which is attributed to the presence of trapping sites resulting from the characteristic microstructure of SP-W coatings. The trapping effects on hydrogen migration have been discussed. For PDP experiments, it has been found that SP-W coatings tend to enhance PDP compared to that through bare F82H which is attributed to the surface recombination characteristics of SP-W. Static deuterium retention has been measured by the thermal desorption spectroscopy (TDS) after steady-state plasma exposure. Increased deuterium retention in SP-W coated F82H has been observed. The deuterium depth concentration profile by the secondary ion mass spectrometry (SIMS) shows a good agreement with the retention data and exhibits a sign of “uphill diffusion” of deuterium in the W/F82H bi-layer structure.

As a proof-of-principle experiment, first wall particle flux measurements in the QUEST spherical tokamak at Kyushu University have been conducted using a SP-W coated F82H permeation probe. The thicknesses of tungsten coatings and F82H substrate are 0.5 μm and 0.25 mm, respectively. The permeation area is 35 mm in diameter. The permeation probe is installed inside the closed port at the mid-plane and the membrane is ~15 cm recessed from the radiation shield. A resistive heater is set behind the membrane to keep the sample temperature in the range of 300-350 ℃. The hydrogen PDP data have

been taken for the probe exposed to a steady-state wall conditioning discharge. The plasma is produced by the 2.45 GHz ECR system with an input power of 7.5 kW. The steady-state hydrogen permeation flux for the SP-W coated F82H membrane has been evaluated by taking into account the effects of the radiation shield and the present data have been compared with our previous results for bare F82H. A much longer PDP breakthrough time and higher steady-state permeation flux have been observed for SP-W coated F82H. It is concluded, therefore, SP-W coatings enhance hydrogen PDP not only in the VEHICLE-1 linear plasma device but also in the QUEST spherical tokamak.

Acknowledgement

My deepest gratitude goes first and foremost to Prof. Yoshi Hirooka, my supervisor, for his instructive advice and useful suggestions on my PhD thesis. I am deeply grateful to have this opportunity to learn the subject of plasma-wall interactions under the guidance of Prof. Yoshi Hirooka. I learned a lot of valuable knowledges and skills in this field under his insightful guidance in the past three years. And, I learned a lot from his scientific attitude as an experimental physicist. I will cherish all the moments we worked together.

I am deeply grateful to Dr. Takuya Nagasaka and Dr. Naoko Ashikawa for their supports on my experiments. They taught me a lot of experimental techniques, shared with me many precious experimental experiences and gave me a lot of guidance on scientific papers publication.

I want to express my gratitude to the rest of my thesis committee, Prof. Katsuyoshi Tsumori, Prof. Kazuaki Hanada and Prof. Takashi Muto for their insightful comments, which are extremely important to improve my thesis.

I am very grateful to Prof. Takeo Muroga, Prof. Akio Sagara, Prof. Izumi Murakami, Prof. Junichi Miyazawa, Prof. Nagato Yanagi, Dr. Juro Yagi, Dr. Daiji Kato, Dr. Yoshimitsu Hishinuma, Dr. Masayuki Tokitani, Dr. Takuya Goto, Dr. Sadatsugu Takayama, Dr. Miyuki Yajima, Dr. Daisuke Nagata, Ms. Shinobu Shimizu and Ms. Shihomi Kato for their helps and caring.

I would like to express my thanks to Prof. Kazuaki Hanada, Prof. Hideki Zushi, Dr. Arseniy Kuzmin, Mr. Zhengxing Wang and the QUEST group of Kyushu University for their assistance with the QUEST experiments.

I would like to express my gratitude to all staffs of the Graduate University for Advanced Studies (SOKENDAI) and the National Institute for Fusion Science (NIFS) for their kind supports during my PhD study.

I would like to thank Japan Atomic Energy Agency, Seinan Industry Co. Ltd and Japan Coating Center Co. Ltd for the material and specimen preparation.

I would like to express my heartfelt gratitude to my friends, Mr. Hailin Bi, Dr. Haishan Zhou, Dr. Hongming Zhang, Dr. Haiying Fu, Dr. Hao Wang, Dr. Xiang Ji, Dr. Shaofei Geng, Dr. Xianli Huang, Dr. Shuyu Dai, Dr. Xiaodi Du, Mr. Gaowei Zhang, Mr. Yang Liu, Mr. Jie Huang, Dr. Bo Huang, Mr. Neng Pu, Mr. Theerasarn Pianpanit and Dr. Botz Huang for their constant encouragements and helps.

A special thanks goes to Mr. Ippei Watanabe, Mr. Junki Morimoto and Mr. Norihiro Ikemoto for their generous assistance with my personal life in Japan.

Dedicated to my families.

Love you all.

Contents

List of figures

List of tables

Chapter 1

Introduction

1.1 Nuclear fusion research

1.1.1 Fundamentals of nuclear fusion

Nuclear fusion has the potential of providing an essentially inexhaustible source of energy for the future. The primary energy source for stars is hydrogen fusion, which is also considered to be one of the most promising candidate sources to provide safe, environment friendly and economical energy for human beings [1-3]. Of all the possible fusion reactions the deuterium-tritium (D-T) reaction is the most attractive one. If a nucleus of deuterium fuses with a nucleus of tritium, an α-particle (He) is produced and a neutron (*n*) is released (shown as Eq. (1.1)). The nuclear rearrangement results in a reduction in total mass and a consequent release of energy in the form of the kinetic energy of the reaction products ($E=(\Delta m)c^2$). The energy released is 17.6 MeV per reaction. In macroscopic terms, just 1 kg of this fuel would release 10^8 kWh of energy and would provide the requirements of a 1 GW (electrical) power station for a day [1].

$$ {}_1^2\mathrm{D} + {}_1^3\mathrm{T} \rightarrow {}_2^4\mathrm{He}\ (3.5\ \mathrm{MeV}) + {}_0^1n\ (14.1\ \mathrm{MeV}) \qquad (1.1) $$

The reaction is induced in collisions between the particles, and the cross-section for the reaction is therefore of fundamental importance. The nuclear cross-section [4-5] of a nucleus is used to characterize the probability that a nuclear reaction will occur. The cross-section at low impact energies is small because of the Coulomb barrier which prevents the nuclei from approaching to within nuclear dimensions as is required for fusion to take place. Because of quantum mechanical tunneling, D-T fusion occurs at energies somewhat less than that required to overcome the Coulomb barrier. Shown in figure 1.1 is the fusion cross-sections for various fusion reactions as a function of kinetic energy of an incident D [1]. It is shown that the maximum cross-section for D-T fusion reaction occurs at just over 100 keV, which is the most efficient fusion reaction to carry out in present magnetic fusion

devices such as tokamaks. The reason the D-T reaction is preferred to other reactions is clear from figure 1.1 where the cross-sections for

$$^{2}_{1}\mathrm{D} + {}^{2}_{1}\mathrm{D} \rightarrow {}^{3}_{2}\mathrm{He}\ (0.82\ \mathrm{MeV}) + {}^{1}_{0}n\ (2.45\ \mathrm{MeV}) \tag{1.2}$$

$$^{2}_{1}\mathrm{D} + {}^{2}_{1}\mathrm{D} \rightarrow {}^{3}_{1}\mathrm{T}\ (1.01\ \mathrm{MeV}) + {}^{1}_{1}p\ (3.02\ \mathrm{MeV}) \tag{1.3}$$

$$^{2}_{1}\mathrm{D} + {}^{3}_{2}\mathrm{He} \rightarrow {}^{4}_{2}\mathrm{He}\ (3.6\ \mathrm{MeV}) + {}^{1}_{1}p\ (14.7\ \mathrm{MeV}) \tag{1.4}$$

are also shown [6]. The D-T fusion reactivity is much greater than that for other potential fusion reactants, which is the reason why achieving the necessary conditions for D-T fusion is the principal goal of the present phase of fusion research.

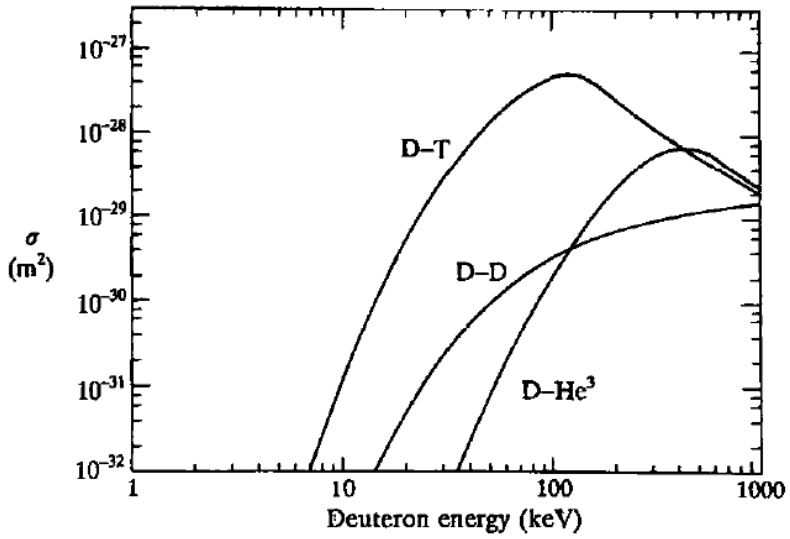

Figure 1.1 Fusion cross-sections for the reactions D-T, D-D and D-He^3 as a function of kinetic energy of an incident D. The curve for D-D represents a sum over the cross-sections of the reaction branches [1].

The D-T reaction (Eq. (1.1)) gives the total energy output of 17.6 MeV, in which the kinetic energy of α-particle, 3.5 MeV, is basically used for the maintenance of steady-state discharge of the fusion plasma and the neutron energy, 14.1 MeV, can be used for output electric energy. In order to realize the fusion reactor, the fusion plasma has to be sufficiently hot and dense and the plasma energy in the toroidal device has to be confined as long as possible [7]. These critical conditions on the plasma performance necessary for the fusion reactor can be quantified by the fusion triple product, $nT\tau_E$. The fusion triple product has to satisfy the following condition well known as Lawson criterion [8] to obtain self-sustaining (ignition):

$$n \cdot T \cdot \tau_E > \sim 5\times10^{21}\ \mathrm{m^{-3}\ keV\ s}, \tag{1.5}$$

where n ($\mathrm{m^{-3}}$) is the plasma density, T (keV) is the plasma temperature and τ_E (s) is the energy confinement time.

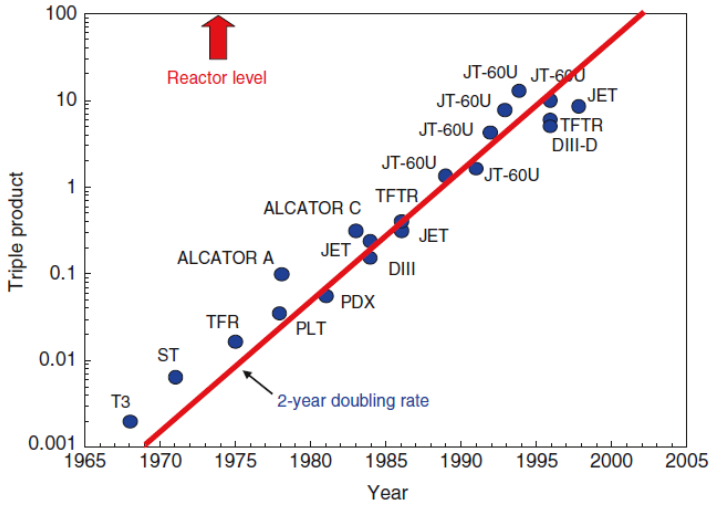

Figure 1.2 Evolution of the triple product $nT\tau_E$ with year. The points are labeled with the names of the fusion devices. The units for triple product are $10^{20}\ \mathrm{m^{-3}\ keV\ s}$ [7].

To achieve ignition, the high-temperature, high-density plasma must be confined in a relatively long time. Over the past half century, the value of $nT\tau_E$ has been significantly improved. Some of these are plotted in figure 1.2 as a function of year [7]. It is clearly shown that the fusion triple product has increased over 10,000 times during past four decades.

1.1.2 Magnetic confinement fusion and inertial confinement fusion

In the star, the plasma is confined by the force of gravity due to the huge amount of matter. On the earth, two leading ideas are proposed to obtain usable energy from fusion reactions: magnetic confinement fusion (MCF) and inertial confinement fusion (ICF).

i) Magnetic confinement fusion (MCF)

In MCF systems, the plasma is confined by magnetic field in desired configurations. The core plasma density is kept at ~10^{20} m^{-3} for several seconds of confinement time to meet Eq. (1.5). From 1950s, various ideas of MCF have been proposed, among which tokamak and stellarator are considered to be the most promising concepts to yield commercial fusion reactors.

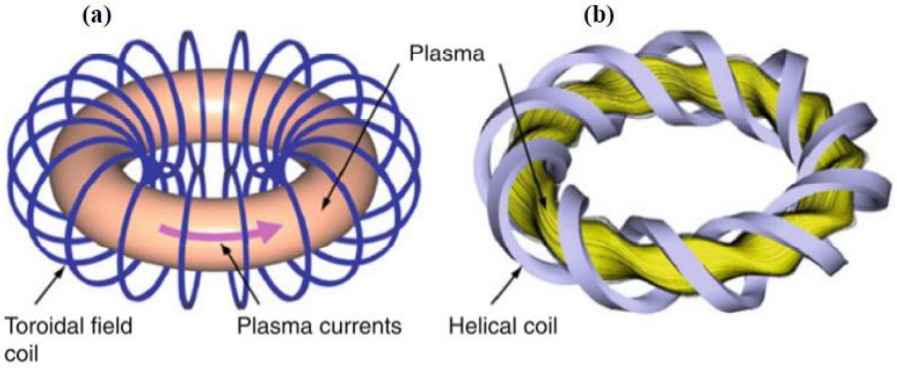

Figure 1.3 Two concepts of magnetic confinement fusion:
(a) tokamak and (b) stellarator [9].

Figure 1.3 shows two concepts of magnetic confinement fusion [9]. For tokamak-type MCF, the plasmas with currents are confined by the toroidal field coils, and then heated to high temperature to meet the self-sustaining ignition condition for fusion reaction. For stellarator -type MCF, it utilizes helical coils to generate magnetic field to confine plasmas. The stellarator-type MCF system has advantages of steady-state and stable operation compared with tokamak-type MCF system, because it does not need currents in plasmas to generate helical magnetic field for confinement. Over the past decades, many large and medium size MCF devices have been built, e.g., JET [10], JT-60 [11], DIII-D [12], ASDEX-U [13], EAST [14], KSTAR [15], QUEST [16] of tokamak-type MCF devices and LHD [17], W7-X [18] of stellarator-type MCF devices. Shown in figure 1.4 is the design of International Thermonuclear Experimental Reactor (ITER) [19], which is under construction in Cadarache, France, by the joint cooperation of seven leading parties, i.e., China, EU, Japan, India, Korea, Russia, and the USA. The goal of ITER is to demonstrate extended burning D-T plasmas at a few hundred MWs of fusion power and engineering feasibility essential to a reactor in an integrated system [20-21], and to test nuclear components required to utilize fusion energy for practical purposes [22]. The ITER first D-T operation is estimated at 2027 [23].

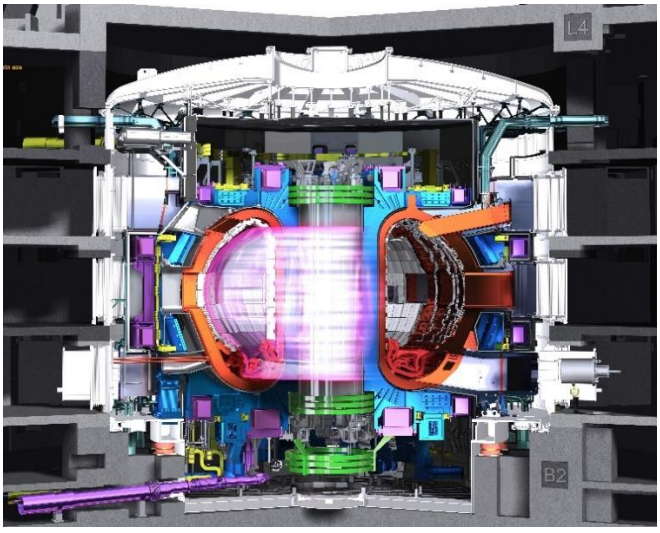

Figure 1.4 The design of ITER tokamak [19].

The MCF device beyond ITER will aim to demonstrate electricity production, i.e., DEMO reactor and then eventually to build fusion power plants. A schematic diagram of a fusion reactor is shown in figure 1.5 [9]. The energy source of a fusion reactor is the burning plasma in the core. SlimCS [24], PPCS-A to PPCS-D [25] and ARIES-AT [26] are several examples for tokamak-type DEMO concepts. Stellarator-type reactor concepts have also been proposed, for example the Force-Free Helical Reactor (FFHR) series concepts being developed by National Institute for Fusion Science (NIFS) in Japan [27]. Recently, some researchers suggested that a test reactor between ITER and DEMO may be necessary in the roadmap to the realization of fusion energy. These concepts include the Chinese Fusion Engineering Test Reactor (CFETR) [28-29] and the Fusion Nuclear Science Facility (FNSF) [30], which aim to provide an integrated, continuous nuclear fusion environment that can be used to investigate plasma material interactions, tritium fuel management, and power extraction, etc.

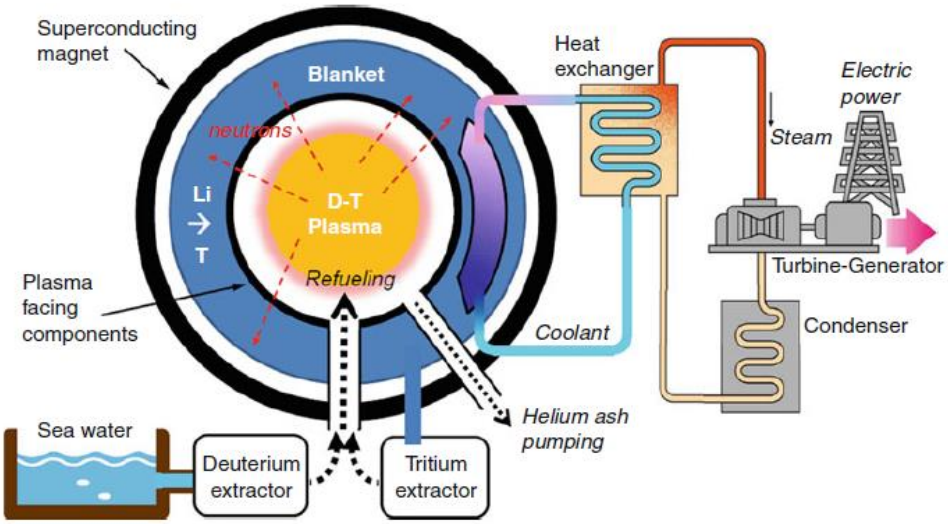

Figure 1.5 Conceptual schematic view of a fusion power plant [9].

ii) Inertial confinement fusion (ICF)

In contrast to MCF, ICF goes a different way to fill the Lawson criterion [8]. Fuel targets containing a mixture of deuterium and tritium are heated and compressed by high-energy laser lights or laser-produced X-rays to generate high-temperature, high-density plasmas [31]. For the ICF plasmas, the density is usually larger than ~10^{31} m^{-3} while the confinement time is shorter than 10^{-10} s [32]. At present, the largest and most energetic ICF device built is the National Ignition Facility (NIF) located at the Lawrence Livermore National Laboratory in Livermore, USA [33]. Recently a fuel capsule gave off more energy than was applied to it in NIF, which is an important milestone towards commercialization of ICF [34]. Besides, the Fast Ignition Realization EXperiment (FIREX) project [35-36] in Japan is another important undergoing ICF research program. In order for the program to be flexible, it is divided into two phases. The goal of the first phase is to demonstrate the ignition temperature of 5-10 keV by a high-energy peta-watt (10 kJ/10 ps) laser [37]. This is followed by the second phase to demonstrate ignition and burning.

1.2 Blanket and the first wall

The blanket surrounds the plasma chamber. It consists of a lithium-containing tritium breeding material, a coolant to remove the neutron-deposited heat, a structural material, and possibly other materials, such as neutron multipliers to enhance the tritium production.

The blanket has two principal functions: (1) to convert the fusion energy into heat, and (2) to produce tritium [38]. Of the energy produced by D-T fusion 80% leaves the plasma immediately in the form of kinetic energy of the 14.1 MeV neutrons. These neutrons transfer their energy to the blanket materials, constituting as such a volumetric heat source in the blanket. The remaining 20% of the energy produced in fusion and all energy externally supplied to heat the plasma ultimately leave the plasma as energetic charged particles or atoms or as radiative energy, in any case constituting a surface heat source incident on the first wall facing the plasma. This first wall is also subjected to substantial

particle fluxes, leading to erosion. Special components are required to handle these concentrated heat and particle fluxes.

1.2.1 Blanket and tritium breeding

Deuterium exists at 0.0153 at.% in sea water and is readily extractable, thus constituting an essentially infinite fuel source [38]. However, tritium, one of the fuels for D-T reaction, is a quite limited resource due to its short half-life (12.5 yr) [39]. Thus, tritium must be produced artificially in reactors, for example, by neutron capture in lithium. The tritium production reactions are [38]:

$$ {}^{1}_{0}n + {}^{6}_{3}\mathrm{Li} \rightarrow {}^{3}_{1}\mathrm{T} + {}^{4}_{2}\mathrm{He} + 4.8\ \mathrm{MeV} \tag{1.6} $$

$$ {}^{1}_{0}n + {}^{7}_{3}\mathrm{Li} \rightarrow {}^{3}_{1}\mathrm{T} + {}^{4}_{2}\mathrm{He} + {}^{1}_{0}n' - 2.5\ \mathrm{MeV} \tag{1.7} $$

The first reaction has a large cross-section for thermal (slow) neutrons, while the second reaction is more probable with fast neutrons. Natural lithium consists of 7.5% ^{6}Li and 92.5% ^{7}Li and it is possible to enrich the lithium to increase the ^{6}Li content [38]. When the lithium is placed around the fusion chamber, the fusion neutrons can be used to produce tritium, thereby introducing the possibility of a fusion reactor "breeding" its own fuel.

The tritium breeding material can be solid or liquid. For example, there are Li_2O, Li_2SiO_3 and Li_4SiO_4 etc. for solid tritium breeders and Li, Li-Pb, Li-Sn and FLiBe (2LiF + BeF_2 mixed molten salt) etc. for liquid tritium breeders. The liquid breeders have the advantage that they can be circulated through the blanket, which allows the bred tritium to be extracted by processing the breeder external to the blanket. Tritium can be readily extracted from the liquid breeders. Shown in figure 1.6 is the 3D view of the FFHR-2 reactor concept [27]. It can be seen that all the internal surface areas are covered by blanket structures for the highest achievable tritium breeding ratio (TBR) (i.e., number of tritium

atoms produced per fusion neutron). From the viewpoint of commercial operation, the breeding materials for a fusion reactor have to achieve a TBR in excess of unity [39], which provides for the possibility of a self-sustained D-T fuel cycle.

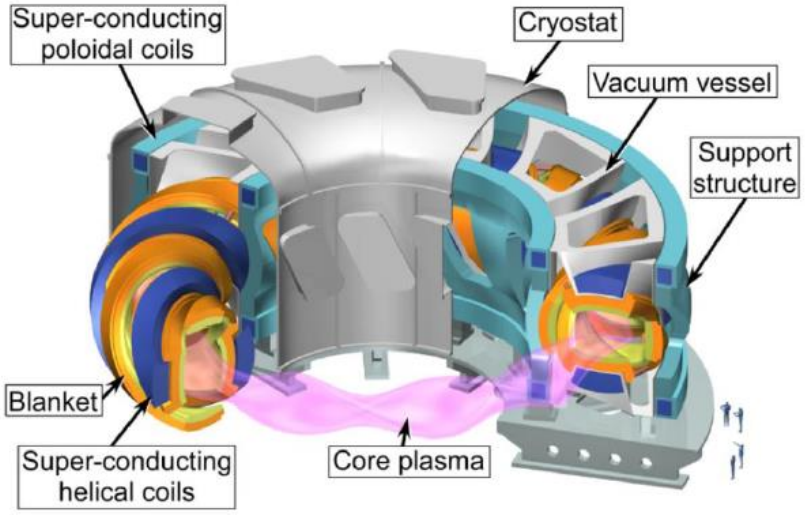

Figure 1.6 The FFHR-2 reactor concept [27].

1.2.2 The first wall of a magnetic fusion power reactor

The definition of the "first wall" will be different for magnetic fusion devices up to ITER and for those to be built thereafter for power generation. It is widely recognized that ITER will generate fusion power which, however, is not intended to be converted into electrical power. This is because no complete blanket concept will be implemented except for test blanket modules (TBM) to cover only a fraction of the surface area exposed to burning plasmas. In this case, the definition of the first wall is nothing but a vacuum chamber wall to separate D-T plasmas from the environment. As opposed to that, for fusion power reactors, essentially all the internal surface areas must be covered by blanket structures for the highest achievable tritium breeding ratio. The first wall is thus redefined

as the plasma-facing walls of breeding blanket units. Figure 1.7 shows a schematic diagram of FFHR-2 blanket [40].

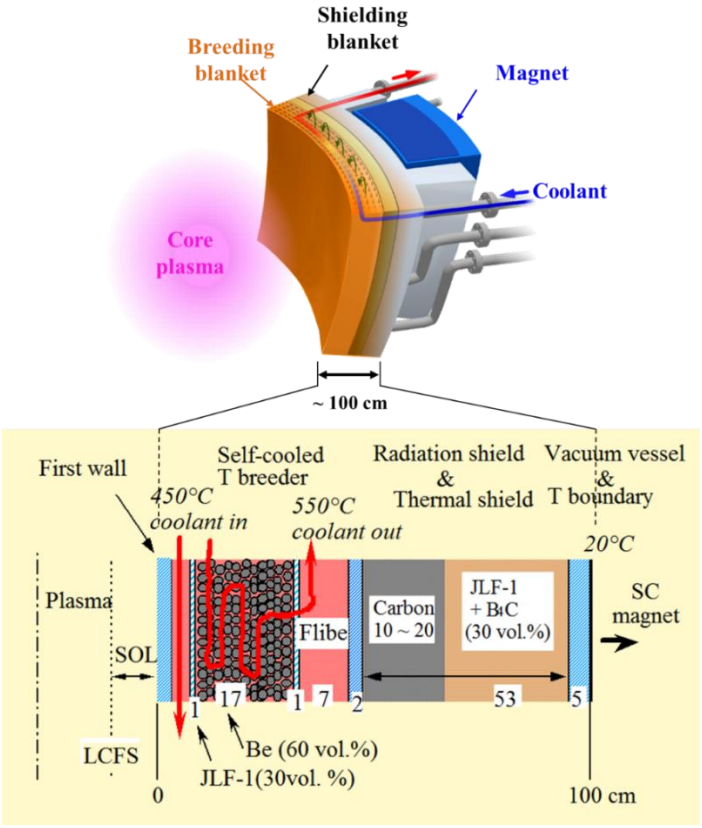

Figure 1.7 A schematic diagram of FFHR-2 blanket [40].

Reduced activation ferritic/martensitic (RAFM) steels such as F82H (Fe-8Cr-2W-0.2V-0.04Ta-0.1C) are the candidate materials for the first wall of DEMO reactors including FFHR-2 [41] due to the following advantages:

(1) Reduced activation. Figure 1.8 compares the radioactivity for four reference alloys after use in the first wall of a commercial fusion reactor [42]. The full-remote and full-hands-on recycle limits are shown to indicate the guideline for recycling and reuse [43]. SS316LN-IG (the reference ITER structural material) [44] will not reach the remote-recycling limit after cooling and thus the recycling is not feasible. F82H and NIFS-HEAT-

2 (V-4Cr-4Ti alloy) behave similarly. The activity of F82H and NIFS-HEAT-2 reached the level almost one order higher than the hands-on recycle limit by cooling for 100 and 50 years, respectively. SiC/SiC composite behaves very differently, with much lower activity at <1 year cooling but slightly higher activity at >100 year cooling relative to F82H and NIFS-HEAT-2.

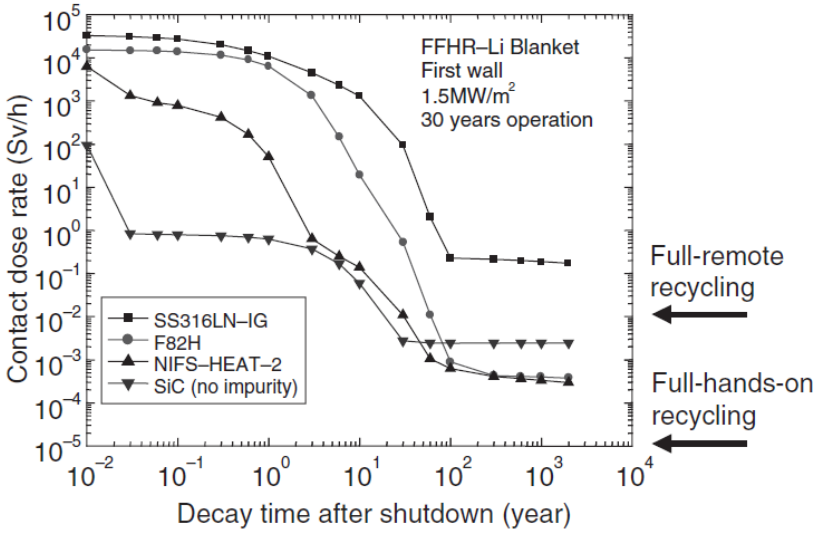

Figure 1.8 Radioactivity after shutdown in first wall of a commercial fusion reactor for four reference alloys [42]. SS316LN-IG: the reference ITER structural material, F82H: reference reduced activation ferritic/martensitic steel, NIFS-HEAT-2: reference V-4Cr-4Ti alloy, SiC/SiC: assumed to be impurity-free.

(2) Swelling resistance. RAFM steels are expected to exhibit a good resistance to swelling (1 vol.% per 100 dpa as compared with 1 vol.% per 10 dpa in stainless steels) [45]. Shown in figure 1.9 is the void swelling behavior of austenitic steels and ferritic/martensitic steels after neutron irradiation [46]. The RAFM steels have much smaller void swelling after neutron irradiation, since high density dislocations, large areas of packets and lath boundaries in the structure of RAFM steels provide sinks for neutron irradiation defects [47].

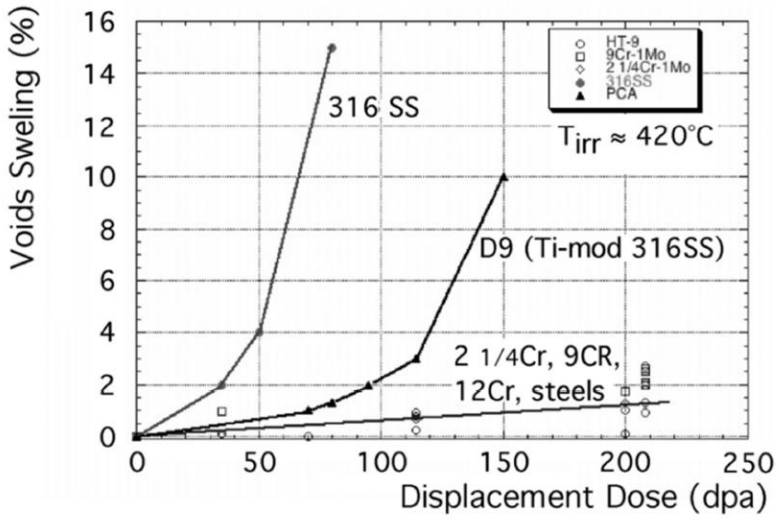

Figure 1.9 Void swelling behavior of austenitic steels and ferritic/martensitic steels after neutron irradiation [46].

(3) High thermal conductivity. Reduced activation ferritic steels have advantage in thermal conductivity, compared with those of the austenitic stainless steels. The thermal stress factor for reduced activation ferritic steels is approximately three times larger than that of austenitic stainless steels at temperatures less than 600 K [41], which allows a relatively thick first wall design for fusion reactor [48]. Thermal characters of some low activation materials are briefly summarized in table 1.1 [49].

Table 1.1 Thermal properties of low activation materials [49].

	RAF (F82H)	V-Alloy (V4Cr4Ti)	SiC_f/SiC	W-Alloy
Thermal conductivity κ (W/mK) (temperature)	32 (550 ℃)	34 (700 ℃)	12.5 (1000 ℃)	85 (1100 ℃)
Young's modulus *E* (GPa) (temperature)	184 (550 ℃)	121 (700 ℃)	~400 (1000 ℃)	
Linear thermal expansion α_i (10^{-6} K^{-1}) (temperature)	12.3 (550 ℃)	11.4 (700 ℃)	~2.5 (1000 ℃)	
Operating temperature (℃)	~550			
Upper limit	~700 (ODS)	~700	~1100	~1200
Lower limit	~300	~400	~600	~900

From the viewpoint of efficient heat exchange, the blanket operational temperature should be close to the maximum temperature at which the structural material can maintain its strength. For RAFM steels, the operational temperature would be around 500 °C [50]. Figure 1.10 shows the relation between the wall thickness and the resulting thermal stress [51]. The major engineering constraints determining first wall thickness are stress (primary and secondary (thermal)) and temperature limit of the materials. As the first wall thickness increases, thermal stress increases in proportion to thickness. The sum of thermal stress and stress arising from internal pressure has a minimum value at the wall thickness of ~5 mm, which is considered to be the optimum thickness in this design configuration.

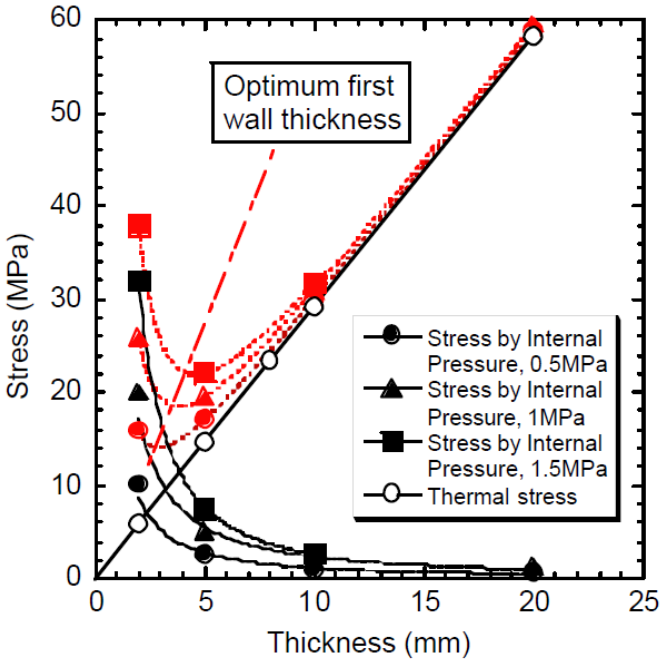

Figure 1.10 Stress vs. the first wall thickness [51].

Table 1.2 shows some of the parameters for the breeding blanket concepts [49]. It can be found that in most of the recent reactor studies, including FFHR, the first wall is designed to be 5 mm or even less, although these concepts employ various first wall materials such as vanadium alloy (V-alloy) and silicon-carbide-fiber-reinforced silicon carbide composites (SiC_f/SiC).

Table 1.2 Examples of the breeding blanket concepts [49].

	He cooled pebble bed	Water cooled pebble bed	Water cooled Pb-17Li	Self-cooled FLiBe	Self-cooled Li	He cooled Li	Self-cooled Pb-17Li (TAURO)	He cooled pebble bed (advanced)
Device	Tokamak DEMO	Tokamak DEMO	Tokamak DEMO	Helical FFHR-2	Tokamak	Tokamak LAR design	Tokamak SEAFP	Tokamak
Structure material	ODS steel RAF	F82H, ODS RAF	EURO-FER RAF	V-Alloy	V-Alloy	V-Alloy (W coating)	SiC_f/SiC	SiC_f/SiC
Fusion power (GW)	3.6	2.3	3.6	1.0		5.3	3.0	4.5
Neutron load (MW/m^2)	4.4 (max)	5.0 (max)	6.6 (max)	1.7 (ave)	10 (max)	11 (max)	2	3.5 (max)
Surface heat load (MW/m^2)	0.8 (max)	1.0 (max)	1.2 (max)	0.1 (ave)	2 (max)	2.73 (max)	0.5	0.6 (max)
FW thickness (mm)	5	3	4	5	4	1.5+1	3	3
FW temperature (℃)	630	~600	590	750	754	697	<1300	913
Coolant	He	H_2O	H_2O	FLiBe	Liq. Li	He	Pb-17Li	He
Pressure (MPa)	8	25	15.5	0.6	0.5	15	1.5	8
Tritium breeder	Li Ceramics	Li_2TiO_3	Pb-17Li	FLiBe	Li	Li	Pb-17Li	Li_4SiO_4
Neutron multiplier	Be	Be ($Be_{12}Ti$)	None	Be	Be	None	None	Be
Ref.	[52]	[53]	[52]	[51]	[54]	[55]	[56]	[57]

1.2.3 Tungsten as plasma-facing material

During the last decades of fusion research, most of the fusion devices with moderate magnetic field and plasma density have implemented low-Z carbon-based materials as plasma-facing materials. This was done after early tokamak experiences with high-Z walls led to poor plasma performance characterized by high central radiation losses, e.g., in PLT [58], JT-60 [59] and TFR [60] which caused severe restrictions in plasma operation. In parallel fusion devices operating with high field (B_t = 6-10 T) at high plasma density such as Alcator C-Mod [61] and FT & FTU [62] operate from the seventies till now with high-Z Mo and partly with W walls. This clearly indicates the favorable conditions for high-Z walls in fusion devices.

The main concerns of graphite and other possible low-Z plasma-facing materials are related to their strong erosion even under low edge plasma temperatures which limits the lifetime and demands frequent exchange of plasma-facing material. Figure 1.11 shows the calculated sputtering yields for beryllium, graphite, iron and tungsten when bombarded with deuterium ions [63]. Beryllium has the lowest atomic number of any structural material, graphite is a low-Z material of much interest, iron is representative of stainless steel, and tungsten, a high-Z material, has one of the lowest sputtering yields of candidate first wall materials. Apart from the lifetime restrictions, strong erosion leads to the built-up of deposits which can contain large amount of tritium by co-deposition. Co-deposition of tritium with carbon is the main mechanism of tritium retention in graphite wall devices and consumed a major fraction of the total tritium fuel supplied to D-T experiments in TFTR and JET [64]. However, tritium retention by co-deposition with eroded tungsten is very small, reduced by factors $>10^4$ over that of carbon since the net tungsten erosion is small and the retention in co-deposited W layers is low as shown in figure 1.12 [65].

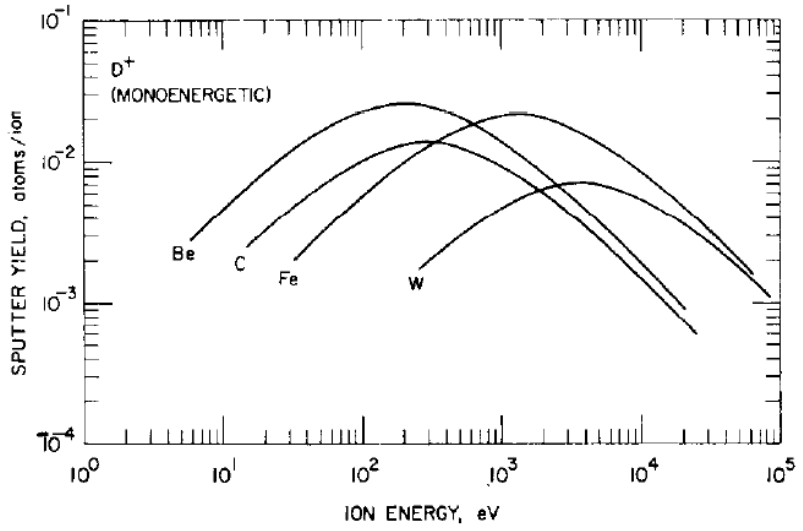

Figure 1.11 Calculated energy-dependent physical sputtering yields of candidate first wall materials bombarded with monoenergetic deuterium ions [63].

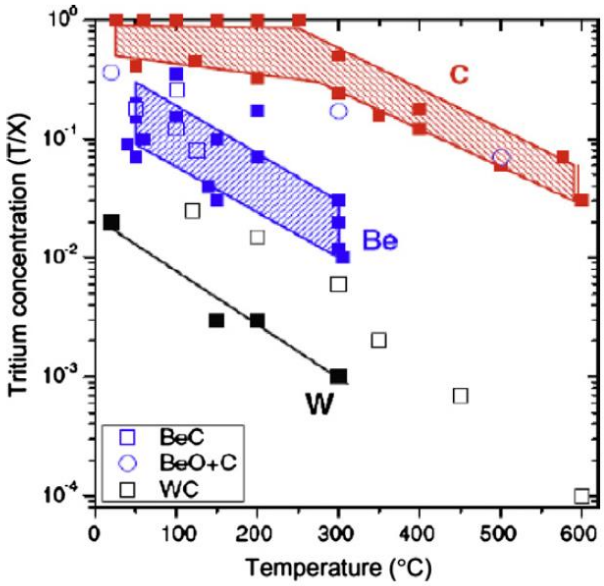

Figure 1.12 Retention fraction of tritium in co-deposited C, Be and W depending on temperature [65].

Tungsten is the most promising candidate for the plasma-facing material of fusion reactors and it has been chosen as divertor plasma-facing material in the activated phase of ITER. For a DEMO reactor, tungsten coatings on reduced activation ferritic/martensitic steels such as F82H are essential to protect the first wall from energetic ions sputtering [66]. Summarized in table 1.3 are the physical and mechanical properties of tungsten and tungsten alloys [67].

Table 1.3 Physical and mechanical properties of tungsten and tungsten alloys [67].

	W	W-1%La_2O_3	W-5%Re
Density (g/cm^3)	19.3	18.9	19.4
Thermal expans. coeff. ($10^{-6}/K$)	4.5	4.7	4.5
Thermal cond. at RT (W/mK)	145	120	70
Elastic modulus (GPa)	410	400	400
Ultimate strength (MPa)	1000	900	1100
Specific heat (J/gK)	0.14	0.14	0.14
DBTT (℃)	100 ~ 400	100 ~ 400	50 ~ 200
Recrystallization temp. (℃)	1150 ~ 1350	1250 ~ 1700	>1500
Melting point (℃)	3410	~3410	~3300
Atomic number	74	(74)	(74)
Atomic weight	183.8	(183.)	(184)
Cross section for thermal neutrons (*b*)	18.5	(18.)	(21.8)
Joining possible:			
Brazing	Yes	Yes	Yes
Welding	No (?)	No	No (?)

1.3 Hydrogen isotopes permeation issues

1.3.1 The plasma sheath

When plasma is in contact with a solid object, such as a limiter, divertor plate or diagnostic probe, a voltage difference spontaneously develops between the plasma and the object called the floating potential. Taken in aggregate, the solid surfaces will float negatively relative to the plasma, or alternatively, one may say that the plasma will adjust to assume a positive potential relative to the solid surfaces.

The potential drop occurs in a thin sheath which is established between the plasma and the solid. The sheath thickness is of order the Debye length λ_D [68]:

$$\lambda_D = (\frac{\varepsilon_0 k T_e}{n e^2})^{\frac{1}{2}}, \tag{1.8}$$

where k is the Boltzmann's constant, T_e is the electron temperature, n is the plasma density and e is the electronic charge.

In the plasma, $n_e = n_i$, i.e., the plasma is quasi-neutral. The plasma sheath, by contrast, has a net positive charge per unit volume since the electrons are repelled by the negative potential on the solid. The areal negative charge density on the solid surface approximately equals the areal positive charge density in the sheath. The sheath thus acts to shield the plasma from the potential on the solid surface. This shielding effect also occurs if the object is biased more negatively than the floating potential, the sheath thickness increases in this case, but is still usually very small compared with plasma dimensions. If the object is biased positively relative to the plasma, then the sheath disappears and the random, Maxwellian-distributed flux of electrons strikes the surface.

The shielding effect of the sheath is imperfect and a small residual field, the pre-sheath, penetrates deep into the plasma. In the simplest case this pre-sheath field extends to the symmetry point between two opposite-facing solid surfaces. The potential drop in the pre-sheath is small and acts to draw ions from the plasma into the sheath. This accelerating

field is just such as to cause the ion drift velocity, at the sheath/plasma interface, to equal the ion acoustic speed C_s [68]:

$$C_s = \left(\frac{k(T_e+T_i)}{m_i}\right)^{\frac{1}{2}}, \tag{1.9}$$

where k is the Boltzmann's constant, T_e and T_i are the electron and ion temperatures, respectively. This is the so-called Bohm criterion [69].

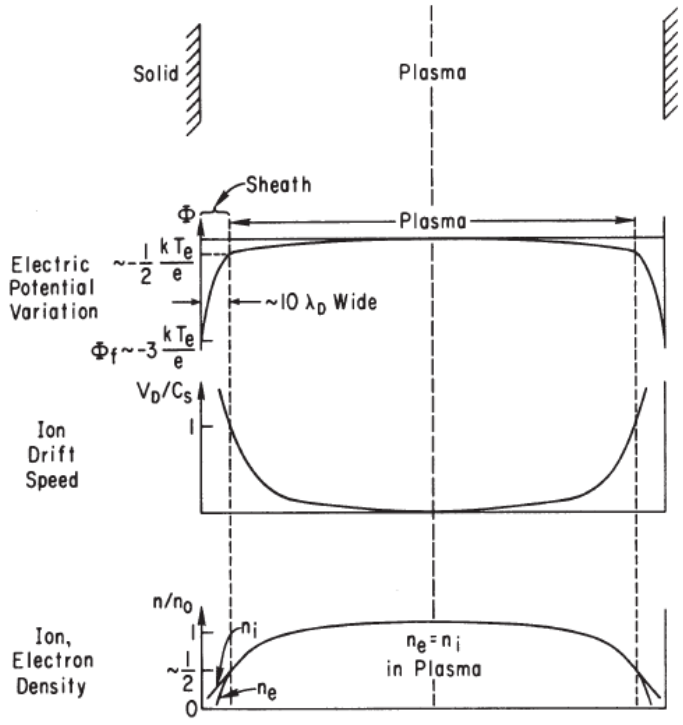

Figure 1.13 Interactions of plasma with a solid surface: a schematic diagram of the variation of electric potential, ion drift speed and ion/electron densities in the plasma between two semi-infinite planes [68].

The potential variations in sheath and pre-sheath, ion drift speed and ion/electron densities variations are shown in figure 1.13 [68]. The Poisson's equation [70] is employed which relates potential variation to space charge density:

$$\frac{\mathrm{d}^2\Phi}{\mathrm{dx}^2} = \frac{e}{\varepsilon_0}(n_e - n_i)\ , \tag{1.10}$$

where n_e and n_i are the electron and ion density, respectively. The existence of the floating potential has a number of consequences: (1) Ions are accelerated through the sheath and thus impact the solid surface with an energy which is greater than that associated with T_i. This generally increases sputtering. It also influences backscattering/retention/release and thus the ability of the solid and plasma to come into equilibrium with regard to the recycle of particles (hydrogen in the case of fusion devices). (2) The sheath controls the rates at which particles and energy are removed from the plasma by the solid surface. One wishes then to know the sheath transmission factors as a boundary conditions for modeling of the edge plasma. (3) For probe analysis one also requires knowledge of these transmission factors for all potentials, in addition to the floating potential.

1.3.2 The scrape-off layer and particle flux to the first wall

In magnetic confinement devices the plasma is confined within closed magnetic flux surfaces, normally generated by a combination of fields due to external conductors and by currents flowing in the plasma. Such fields can only be generated within a restricted volume, and there is therefore a boundary determined by the last closed flux surface (LCFS). The shape of the LCFS is determined by the magnetic fields. However, closed magnetic surfaces may be interrupted by a solid surface which then determines the position of the LCFS. Such a solid surface is called a limiter. Alternatively the closed surface may be determined entirely by the magnetic fields so that outside the LCFS, the plasma flows towards and eventually interacts with a solid surface. This is the basic geometry of a divertor. The essential difference between these two is that with a limiter the LCFS is in contact with a solid surface which is close to the plasma, while with a divertor the solid surface is removed some distance from the LCFS. The region radially outboard of the LCFS (separatrix) is called the scrape-off layer (SOL). Shown in figure 1.14 is a schematic diagram of the SOL in a magnetic fusion device [71].

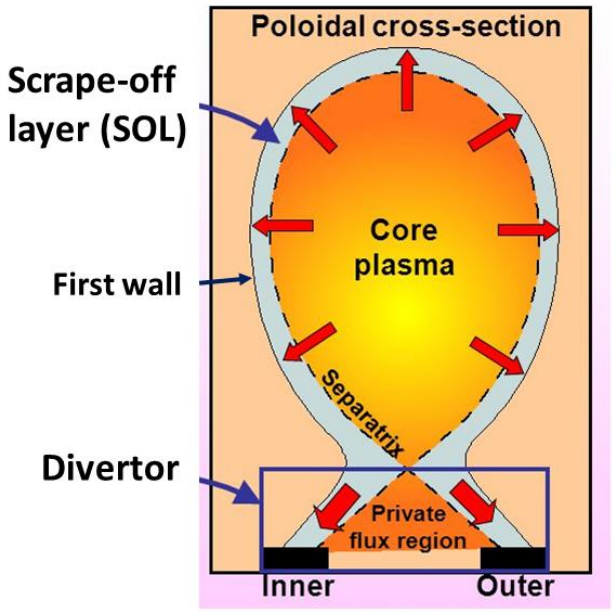

Figure 1.14 A Schematic diagram of the scrape-off layer (SOL) in a magnetic fusion device (replotted from [71]).

The particle flux density Γ to the surface of first wall is given by [71]:

$$\Gamma = \frac{1}{2} n C_s = \frac{1}{2} n \left(\frac{k(T_e+T_i)}{m_i}\right)^{\frac{1}{2}}, \tag{1.11}$$

where k is the Boltzmann's constant, n is the plasma density, T_e and T_i are the electron and ion temperatures, respectively. Generally, the edge plasma density in the SOL is of the order of 10^{13} cm^{-3}, the electron temperature is ~10-20 eV and the cross-field diffusion coefficient is typically of the order of 10^3 cm^2 s^{-1}. Assuming that the thickness of SOL is a few cm, the cross-field particle flux to the first wall may be estimated to be of the order of 10^{16} atoms cm^{-2} s^{-1}. Behrisch et al. [72] calculated the profiles of various incident ions fluxes to the first wall (figure 1.15). It can be seen that the incident deuterium flux to the first wall has been calculated to be ~10^{16} D cm^{-2} s^{-1}. A similar order estimate can be obtained from the cross-field transport scaling law observed in Alcator C-Mod [73]. The calculated particle bombarding energy to the first wall is shown in figure 1.16. One finds that the average particle bombarding energy is ~100-300 eV.

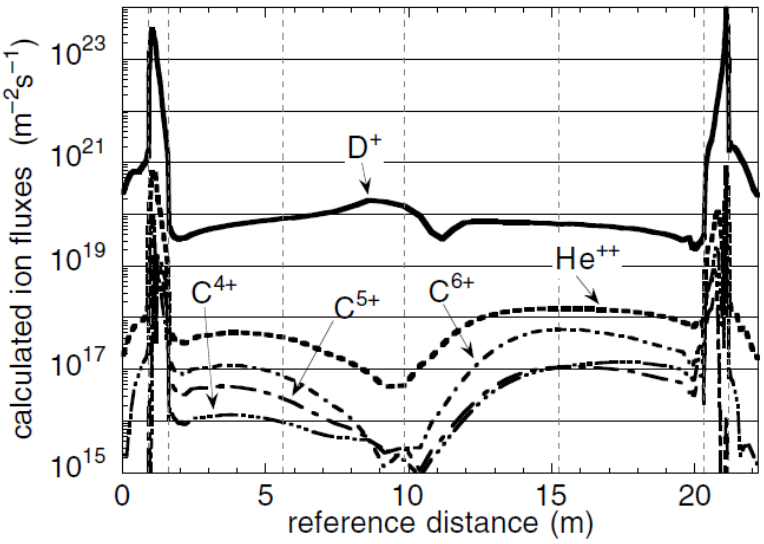

Figure 1.15 Calculated profiles of various ions fluxes to the first wall of a fusion reactor [72].

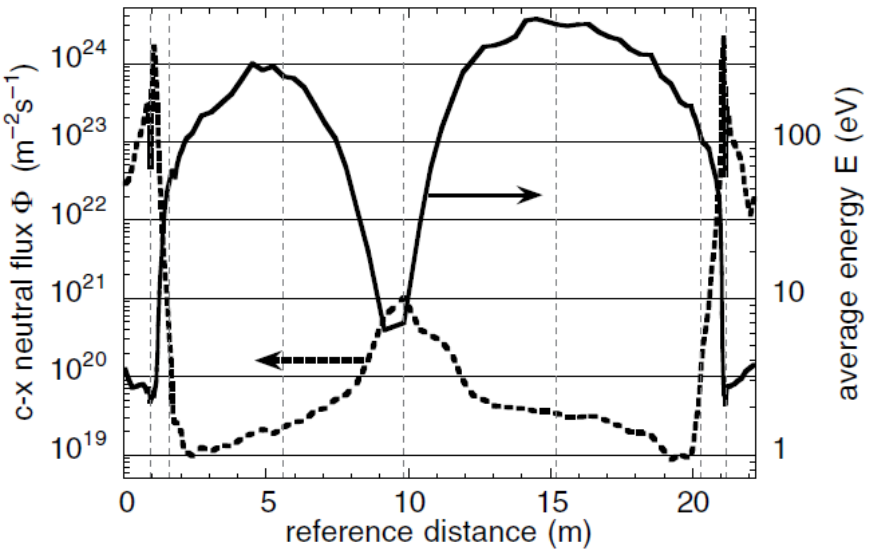

Figure 1.16 Calculated bombarding energy profile of incident particles to the first wall of a fusion reactor [72].

1.3.3 Bi-directional permeation

As shown in figure 1.17, the first wall will be exposed to edge plasma at elevated temperatures on the one side, and also it will be in contact with a liquid breeder or coolant, either one of which contains bred tritium on the other side. One then predicts that the first wall will be subjected to hydrogen isotopes penetration in the two opposite directions. From the edge plasma side, deuterium and tritium flow into the blanket by the mechanism referred to as plasma-driven permeation (PDP), and from the blanket bred tritium flows into the plasma side by gas-driven permeation (GDP).

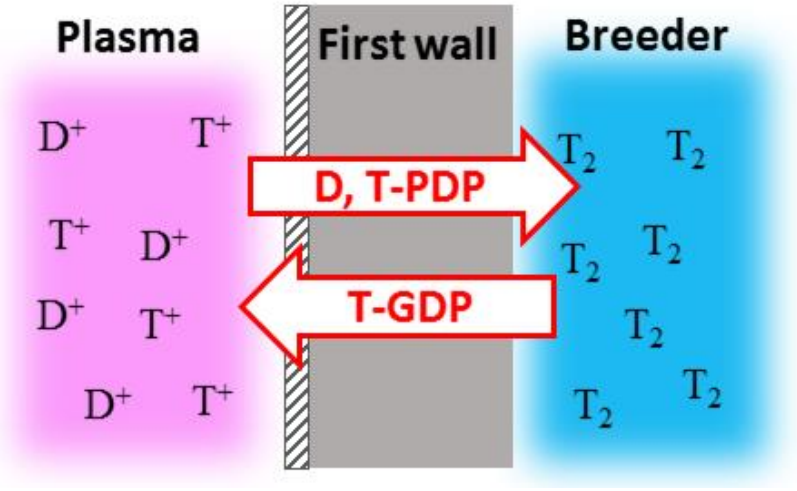

Figure 1.17 Hydrogen isotopes PDP and GDP through the first wall.

It is important to note that PDP necessitates an isotope separation capability in the tritium recovery loop of a reactor, which then complicates the entire fuel recycle system, and GDP, essentially the same effect as gas-puff for fueling except that it is uncontrollable, will lead to an unwanted increase in edge plasma density, which could even affect core confinement performance as well as isotope mixture imbalance [74].

Figure 1.18 shows a schematic diagram of the tritium flow in a FLiBe loop, taking into account the tritium leakage from the first wall. The overall tritium balance can be expressed as:

$$\frac{\partial M_T}{\partial t} = J_1 + J_2 - \sum J_3 - J_4 - J_5 \,, \tag{1.12}$$

in which M_T is the tritium inventory in the loop, J_1 is the tritium production rate, J_2 is the tritium PDP flow into blanket, J_3 is the tritium GDP flow from blanket and GDP leak from pipes, J_4 is the recovered tritium, and J_5 is the tritium GDP leak from heat exchanger. It is indicated in Eq. (1.12) that the bi-directional hydrogen isotopes PDP and GDP would effect on the overall fuel balance of a fusion reactor, which warrants detailed investigations on this subject.

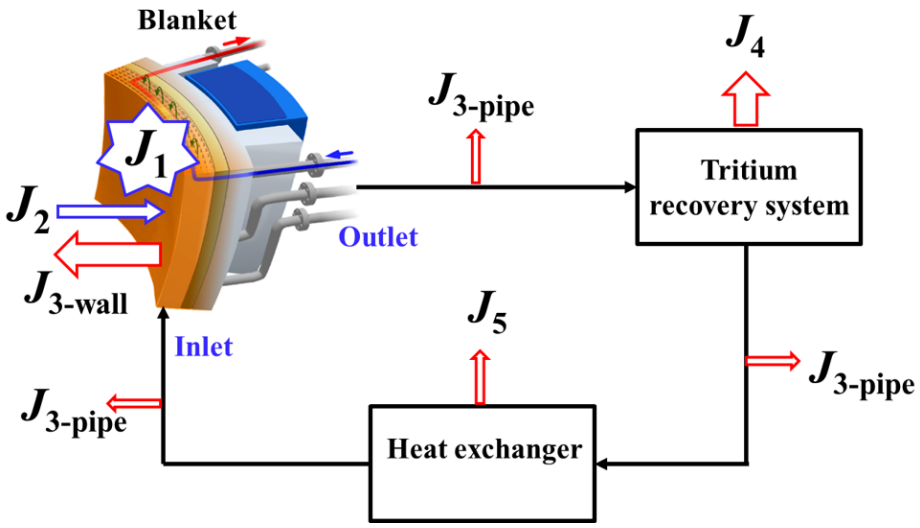

Figure 1.18 Schematic of the tritium flow in a FLiBe loop.

From 1980s, researchers started to investigate plasma-driven permeation issues using low energy, high flux plasmas, which are relevant to the reactor plasma-wall interaction conditions. Those data are summarized in table 1.4.

Table 1.4 A summary of the PDP experimental data in literature.

Material	Temp. (K)	Incident flux (cm^{-2} s^{-1})	E_{ion} (eV)	Thickness (mm)	Permeation flux (cm^{-2} s^{-1})	Ref.
F82H	773	1.0×10^{16}	<10	1.0	9.0×10^{13}	[75]
SUS304	683	8.8×10^{16}	20		1.5×10^{15}	[76]
SUS304	673	6.8×10^{16}	20-40 150	0.25	3.2×10^{14} $\sim 2 \times 10^{13}$	[77]
SUS304	400-673	Ne<~5×10^{10} cm^{-3}	<10	0.01	6.3×10^{14} (at 480 K)	[78]
Ni	523	Ne<~5×10^{10} cm^{-3}	<10	0.02 0.05 0.2	$\sim 9 \times 10^{14}$ $\sim 6 \times 10^{14}$ $\sim 2 \times 10^{13}$	[79]
Ni	473-773	3×10^{16}	100	0.3	$< 5 \times 10^{13}$	[80]
Nb	983	$5 \sim 10 \times 10^{16}$	few-200	0.3	$< 3.5 \times 10^{15}$	[81]
Kovar	773	$\sim 5.7 \times 10^{16}$	20	0.25	6.1×10^{13}	[82]
TiB_2 coated Kovar	773	$\sim 5.7 \times 10^{16}$	20	0.015/0.25	1.5×10^{13}	[82]
Nb & Nb/Pd	775-975	2.5×10^{16}	10-100	0.1	$< 6.3 \times 10^{15}$	[83]

As described at the beginning of this section, for those blankets employing liquid breeder to serve as a coolant as well (self-cooled breeder), the first wall is to be exposed to tritium bred in blankets, depending on its dissociation pressure, which may result in GDP. Shown in figure 1.19 are the equilibrium tritium partial pressures in lithium and lithium compounds at temperature of 800 K [84]. For FLiBe, which is the candidate breeder for the FFHR reactor [51], the tritium dissociation pressure is ~10^4 Pa at a T/M atomic concentration of ~0.1 ppm.

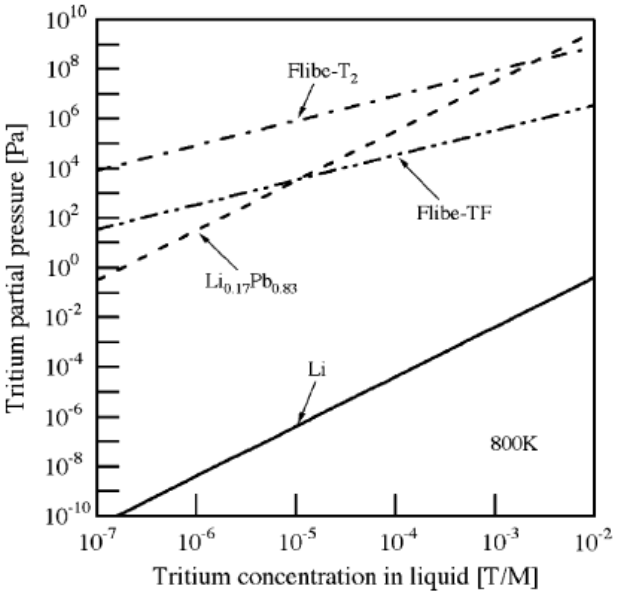

Figure 1.19 Equilibrium tritium partial pressures dissolved in lithium and lithium compounds [84].

Shown in table 1.5 are some experimental data on gas-driven permeation for various metals. Compared with the database of PDP, the data on hydrogen isotopes GDP through metals are much more comprehensive and updated. Hydrogen isotopes transport parameters in tungsten and several kinds of RAFSs are available. Those GDP experiments were performed with a driving pressure <10^5 Pa at a temperature range of 322-2073 K. Some specific aspects such as trapping [59] and ceramic coatings [63] were also investigated. However, due to the limitations of GDP setups, the surface recombination process is difficult to be addressed in these studies.

Table 1.5 A summary of the GDP experimental data in literature.

Material	Thickness (mm)	Gas	Pressure (Pa)	Temp. (K)	E_P (eV)	E_D (eV)	E_S (eV)	Ref.
F82H	1	H_2	1.33×10^4-10^5	423-793	0.39	0.14	0.25	[85]
F82H	0.5-0.8	D_2	5×10^2-10^5	373-743	0.42	0.14	0.28	[86]
F82H	0.4	H_2	10^3-10^5	373-723	0.41	0.15	0.27	[87]
F82H					0.50*	0.12	0.38	
F82H (oxidized)	1	D_2	10^2-10^3	573-873	0.42*	0.08	0.34	[88]
F82H	0.85	T_2	8×10^2-5.3×10^3	490-	0.42	0.08	0.34	[89]
		D_2		1000	0.43	0.083	0.35	
F82H	1	D_2	10^2-10^3	573-873	0.46	0.081	0.37	[90]
		H_2			0.43	0.083	0.34	
Batman	0.5-0.8	D_2	5×10^2-10^5	373-743	0.43	0.16	0.26	[86]
MANET Ⅱ	0.5	D_2	10^3-10^5	633-743	0.44	0.14	0.28	[91]
SUS304	0.1-0.3	H_2	10^3-10^5	500-	0.68	0.52	0.16	[92]
SUS316				1200	0.64	0.50	0.14	
Fe	0.5	H_2	2.8×10^3-10^5	342-619	0.35	0.07	0.28*	[93]
Fe	1.33	H_2	4.3×10^2-5.3×10^3	322-779	0.37	0.07	0.30*	[94]
		D_2			0.38	0.08	0.30*	
W	0.175	H_2	$0 \sim 2.7 \times 10^4$	1173-2073	1.43	0.39	1.04	[95]
W	0.5-2.5	H_2	$\sim 10^2$-10^4	673-1473	1.10	1.07	0.03	[96]
W	0.114	D_2	10^4-10^5	850–950	1.21	0.96	0.25	[97]

* Estimated value from diffusion and solution coefficients.

During the last decade, experimental studies on the joint optimization of vacuum plasma-sprayed tungsten (VPS-W) coatings and F82H substrate were investigated by Tokunaga et al. [98], Kim et al. [99] and Tanigawa et al. [100]. The microstructure and thermophysical properties of VPS-W coatings were reported by Yahiro et al. [101] and Nagasaki et al. [102] to evaluate the possibility of VPS-W coatings as plasma-facing armor. Besides, surface damage of VPS-W coatings on F82H due to repetitive ELM-like pulsed deuterium plasma irradiation was investigated by Kikuchi et al. [103] using a magnetized coaxial plasma gun. There was no indication of exfoliation of the tungsten coatings from F82H substrate after pulsed plasma exposures. Otsuka et al. [66, 104] reported studies on the retention and release mechanisms of tritium loaded in VPS-W coated F82H by plasma exposure. Tritium depth profile were examined using the tritium imaging plate technique [105] and the changes of tritium depth profile during storage and after annealing were monitored. The results supported that retention of tritium is mainly caused by pore diffusion of gaseous tritium followed by dissolution and trapping in tungsten grains, and dissolution of tritium into the F82H substrate.

In summary, although tungsten is a candidate coating material for the first wall (made of RAFSs such as F82H) of a DEMO reactor, no hydrogen isotopes permeation experiments, especially PDP experiments, for tungsten coated RAFSs have been reported in the existing database. Literature data on hydrogen transport parameters for tungsten and RAFSs are limited because all these data are taken only from GDP experiments and the surface recombination process under plasma exposure is not sufficiently investigated. From the viewpoint of fusion engineering study, more efforts are needed to establish the database of hydrogen isotopes GDP and PDP through tungsten coated RAFSs.

1.4 Objectives of this work

Evaluation of hydrogen isotopes permeation through the first wall and coatings effects on hydrogen permeation are of crucial importance to the fusion reactors design work. This PhD thesis research aims (1) to demonstrate experimentally hydrogen isotopes (H/D) simultaneous bi-directional permeation predicted for the first wall of a fusion power reactor, (2) to investigate tungsten coatings effects on hydrogen isotopes GDP and PDP behavior, (3) to investigate the isotopic effects on hydrogen transport, and (4) to establish a fundamental database on hydrogen and deuterium transport parameters for designing the first wall of fusion power reactors.

1.5 Outline of the thesis

This PhD thesis is structured as follows: after this introduction chapter, some theories and models on hydrogen isotopes transport in solids will be briefly reviewed in Chapter 2. The laboratory-scale steady-state plasma device: VEHICLE-1 and the permeation setup will be introduced in Chapter 3. In Chapter 4, studies on hydrogen isotopes gas- and plasma-driven permeation through a reduced activation steel alloy F82H will be presented, experimental demonstration of simultaneous bi-directional permeation through F82H will be shown as well. Hydrogen isotopes GDP and PDP through F82H coated with two different types of tungsten coatings, i.e., vacuum plasma-sprayed tungsten and sputter-deposited tungsten will be presented in Chapter 5 and Chapter 6, respectively. Chapter 7 includes the experimental results of hydrogen PDP through a sputter-deposited tungsten coated F82H permeation probe in the medium size spherical tokamak QUEST, followed by a summary and implications to reactors design in Chapter 8.

Chapter 2

Theories on hydrogen isotopes transport in solids

In Chapter 1 the phenomena of hydrogen isotopes gas- and plasma-driven permeation through the first wall of a magnetic fusion reactor have been introduced. The databases of gas- and plasma-driven permeation experiments have been briefly reviewed as well. This chapter reviews some of the physical mechanisms involved in the interaction of hydrogen particles with solids, their diffusion and trapping in the solids, and the surface recombination allowing them to be released. In the latter part of this chapter, the steady-state permeation models and hydrogen isotopic effects are shown.

2.1 Entering and release of hydrogen isotopes in solids

2.1.1 Reflection and implantation

When energetic hydrogen atoms or ions impinge on the first wall, a fraction of them are reflected in a time of $\leq 10^{-12}$ s [68]. The particle reflection coefficient R_N is defined as the number of all backscattered particles N divided by the number of incident particles N_0. As shown in figure 2.1, the particles backscattered have distributions in energy E, exit polar angle β, exit azimuthal angle φ and charge state q_i, depending on the incident energy E_0 and angle α, which may be described by [68, 106]:

$$f(E_0, \alpha; \mathrm{E}, \beta, \varphi, q_i). \tag{2.1}$$

Then R_N can be obtained by integrating the distributions:

$$R_N(E_0, \alpha) = \sum_i \int_0^{E_0} dE \int_0^{\pi/2} d\beta \int_0^{2\pi} d\varphi f(E_0, \alpha; E, \beta, \varphi, q_i) \sin\beta. \tag{2.2}$$

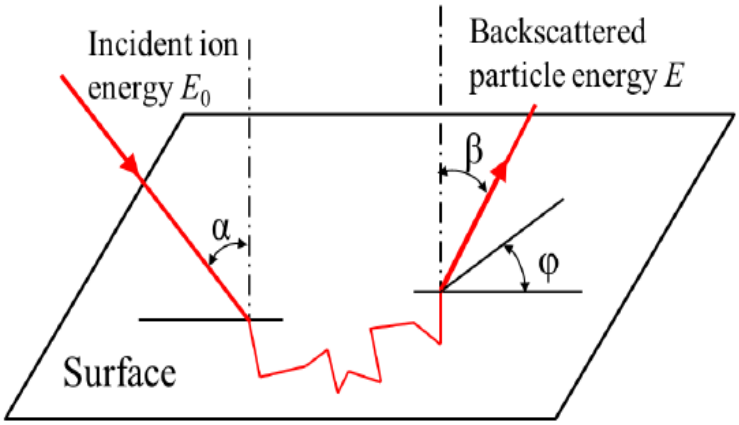

Figure 2.1 Backscattering of an ion with incident energy E_0 from the surface of a solid [68].

The particles which are not backscattered are implanted into the wall. These particles will be slowed down by transferring energy to the target electrons (electronic stopping), or by interaction with the target atom core (nuclear stopping). The mean range of implantation ions may be calculated by [107]:

$$\bar{d} = \frac{1}{n}\int_0^{E_0} \frac{dE}{s(E)}, \tag{2.3}$$

where E_0 is the incident energy, n is the particle number and $S(E)$ is the total stopping cross-section from electronic and nuclear stopping.

Based on the binary collision approximation (BCA) [108], several Monte Carlo simulation codes have been developed for plasma-wall interaction applications, for example, TRIM [109], ACAT [110] and EDDY [111]. Shown in figure 2.2 are the calculation results for reflection coefficient of hydrogen on pure iron surface by these codes [74]. The calculated reflection coefficient decreases as an increase of implantation energy when E_0 is larger than 10 eV. Figure 2.3 shows a calculation on hydrogen implantation profile in iron by the EDDY code. In general, the implantation range increases with increasing incident energy.

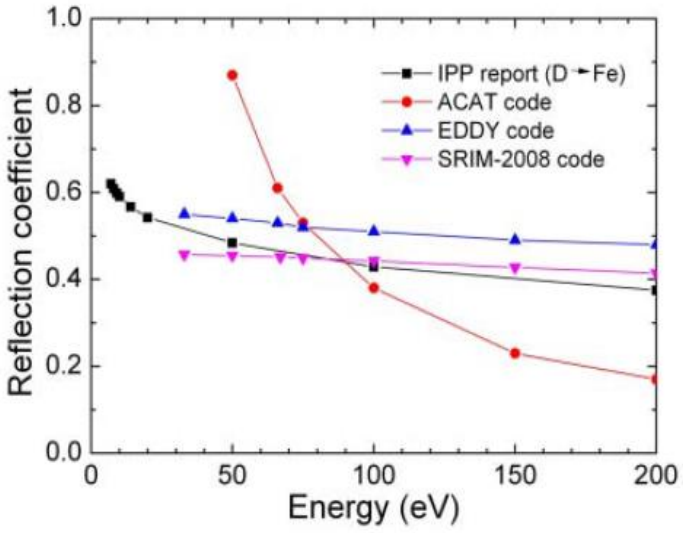

Figure 2.2 Particle reflection coefficient of hydrogen on iron estimated by the Monte Carlo codes [74].

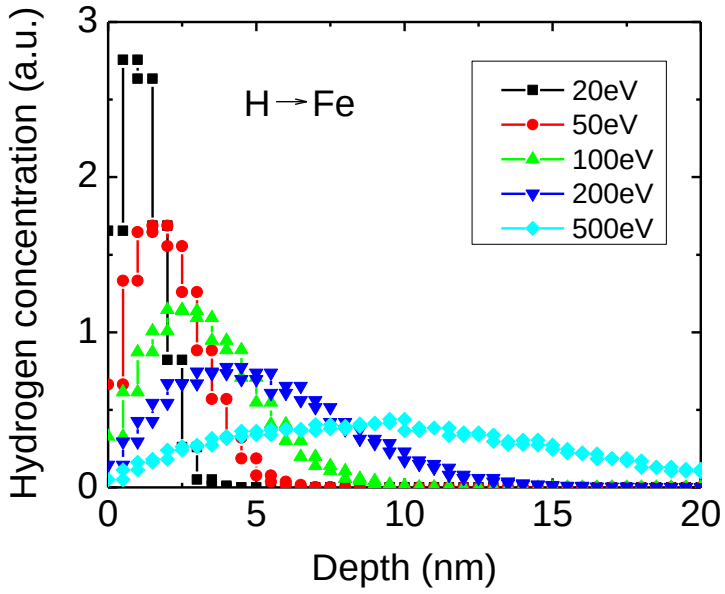

Figure 2.3 Calculated hydrogen implantation profiles in iron at different incident energies by the EDDY code.

2.1.2 Solution

In this section, we review the relationship for solubility assuming thermodynamic equilibrium between the diatomic hydrogen molecule and hydrogen atoms in a metal:

$$\frac{1}{2}\mathrm{H}_2 \leftrightarrow \mathrm{H}. \tag{2.4}$$

The hydrogen solubility in metal is proportional to the square root of the partial pressure of the gas (Sieverts' law [112]) and the bulk concentration *C* which can be given by:

$$C = S\sqrt{P}\,, \tag{2.5}$$

where *S* is the hydrogen solubility of the membrane material or the Sieverts' constant which can be expressed as [107]:

$$S = S_0 \exp(-\frac{U_S}{kT}), \tag{2.6}$$

where U_S is the enthalpy of solution, which is positive for endothermal hydrogen-solid system and negative for exothermal case. *k* is the Boltzmann's constant and *T* is the temperature (K).

2.1.3 Diffusion and trapping

The dissolved hydrogen atoms may transport in the lattice by random-jumping migration between interstitial lattice positions, or be trapped by defects and impurities in the lattice. Figure 2.4 shows a schematic energy diagram for hydrogen in metals [107]. It can be seen that the trapping sites expose a higher binding energy than regular solution sites. The behavior of one-dimensional hydrogen transport in a solid with trapping sites can be described by the following equations [113]:

$$\frac{\partial C(x,t)}{\partial t} = D(T)\frac{\partial^2 C(x,t)}{\partial^2 x} - \frac{\partial C_t(x,t)}{\partial t} + G(x,t) \tag{2.7}$$

$$\frac{\partial C_t(x,t)}{\partial t} = D(T)\frac{C(x,t)C_t^e(x,t)}{\lambda^2} - C_t(x,t)\nu_0 \exp(-\frac{U_t}{kT}) \tag{2.8}$$

$$C_t^e(x,t) = C_t^0(x) - C_t(x,t), \tag{2.9}$$

where $C(x,t)$ and $C_t(x,t)$ are the concentrations of mobile and trapped atoms as a function of position x and time t; D is the diffusion coefficient; T is the temperature; $G(x,t)$ is the hydrogen implantation profile; $C_t^0(x)$ and $C_t^e(x)$ are the concentrations of intrinsic and empty trapping sites, respectively; λ is the mean distance between trapping sites; ν_0 is the jumping frequency; k is the Boltzman's constant and U_t is the de-trapping energy. Equation (2.7) indicates that trapping sites introduced by neutron or energetic particle bombardment will only affect the initial transient permeation behavior.

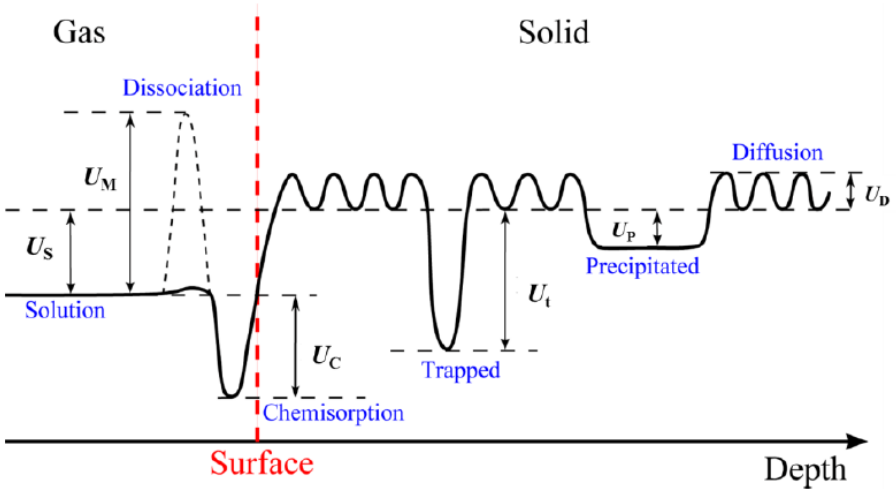

Figure 2.4 Schematic energy diagram for hydrogen in metals (replotted from [107]). U_S, U_C, U_t and U_P are the enthalpies of solution, chemisorption, trapping and precipitation. U_M is dissociation energy and U_D is the activation energy for diffusion.

Hydrogen diffusion through metals is thermally activated process, thus it features an Arrhenius-type dependence on temperature and can be expressed as [114]:

$$D = D_0 \exp(-\frac{U_D}{kT}), \tag{2.10}$$

where D_0 is the pre-exponential containing the jumping frequency and lattice structure information, and U_D is the activation energy for diffusion.

2.1.4 Surface recombination

With the exception of extremely high temperatures, hydrogen is released from the surface of a solid via the recombination of dissolved atoms to hydrogen molecules [115]. The recombination flux (i.e., re-emission flux) J- is proportional to the square of the hydrogen concentration at the surface C [107]:

$$J_- = K_r C^2, \tag{2.11}$$

where K_r is the recombination coefficient.

Based on the idealized energy diagram shown in figure 2.4, several models for estimating K_r have been proposed (see Ref. [116-118]). Baskes [116] gave a simplified method to calculate the recombination coefficient and the K_r is given as:

$$K_r = \frac{K_0}{\sqrt{T}} \exp(-\frac{U_K}{kT}), \tag{2.12}$$

where U_K is the activation energy of recombination and $U_K = U_D + U_S$ when $U_D + U_S \geq 0$; and $U_K = 2U_S$ when $U_D + U_S < 0$. K_0 is a pre-factor which is related to the solubility, diffusivity and surface sticking coefficient.

2.2 Steady-state GDP models

2.2.1 Diffusion limited GDP

According to the Fick's first law, the one-dimensional steady-state hydrogen permeation flux J_+ controlled by diffusion is generally given by [119]:

$$J_+ = -D\frac{\partial C}{\partial x}, \tag{2.13}$$

where D is the hydrogen diffusivity, $\partial C/\partial x$ is the hydrogen concentration gradient.

The upstream and downstream pressures are denoted by P_1 and P_2. The downstream side is normally kept in high vacuum ($P_2 \approx 0$), hence the hydrogen concentration at the downstream surface is almost zero. The solution of Fick's first law is [120]:

$$J_+(t) = \frac{DS\sqrt{P_1}}{L}\left[1 + 2\sum_{n=1}^{\infty}(-1)^n \exp(\frac{-Dn^2\pi^2 t}{L^2})\right], \tag{2.14}$$

where L is the membrane thickness.

The total amount of hydrogen which has permeated through the membrane per unit area can be written as:

$$Q(t) = \int J dt = \frac{DS\sqrt{P_1}}{L}\left[t - \frac{L^2}{6D} - \frac{2L^2}{\pi^2 D} \times \sum_{n=1}^{\infty}\frac{(-1)^n}{n^2}\exp\left(\frac{-Dn^2\pi^2 t}{L^2}\right)\right]. \tag{2.15}$$

The diffusivity D can be measured from the transient permeation behavior by fitting the transient permeation flux data as shown in figure 2.5(a) [85]. Diffusivity can also be estimated either by the so-called time-lag method $t_l = L^2/6D$ [120], at which a line fitted to the asymptotic region of the time-integrated flux $Q(t)$ curve intersects the time axis (figure 2.5(b)), or by measuring the breakthrough time $t_b \approx L^2/15.3D$ [121]. All of the above-mentioned three methods can be used to obtain D, depending on the experimental data conditions. For example, if the transient curve is not available, D can be measured from the steady-state data by time-lag method. On the other hand, breakthrough time measurement would be useful when the permeation flux cannot reach steady-state.

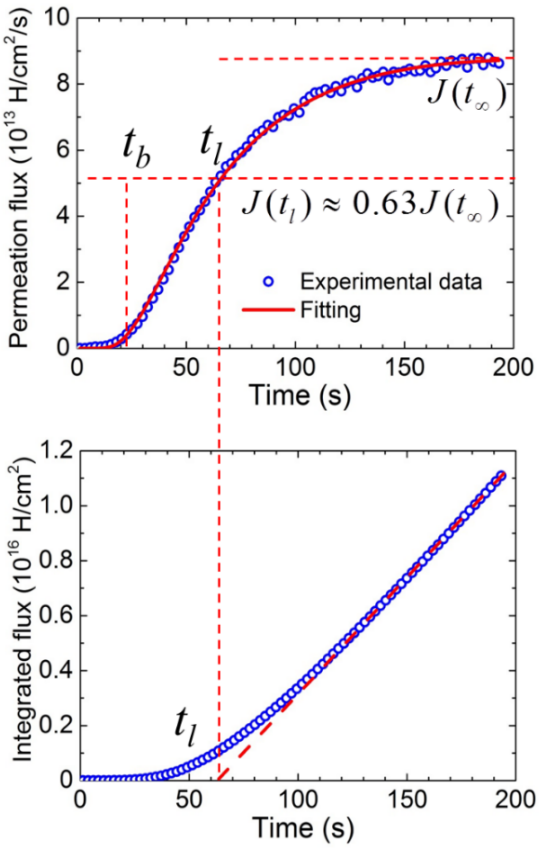

Figure 2.5 An example of diffusivity measurement: (a) fitting the transient GDP flux curve, and (b) time-lag from time-integrated GDP flux [85].

Steady-state permeation rate J_∞ is driven by the difference of the hydrogen concentration at the upstream and downstream surface. Hence, the Eq. (2.14) becomes:

$$J_\infty = \frac{\Phi\sqrt{P_1}}{L}, \tag{2.16}$$

where Φ is the permeability of hydrogen through a solid and $\Phi = DS$. D and S are assumed to be independent of hydrogen concentration and time, being only a material property. The right term in Eq. (2.16) is valid also for multi-layer membrane if Φ represents the effective permeability coefficient Φ_{eff}.

Experimental evidence of diffusion limited permeation is $J_\infty \propto \sqrt{P}$ in contrast to $J_\infty \propto P$ which is characteristic for surface limited permeation regime. In general, the diffusion limited permeation regime is valid at high driving pressures *P*. More detailed conditions on validity of each permeation regime can be found in Ref. [122-123] for single-layer membrane and in Ref. [124] for multi-layer membranes.

2.2.2 GDP through a two-layer membrane

Coating the membrane with an additional layer (barrier) always results in the reduced permeation if diffusion remains the rate limiting process. The experimental proof of the barrier efficiency is a relative reduction of the steady-state permeation flux measured at the identical conditions (*P*, *T*). Its definition is the ratio of the steady-state permeation rate through the uncoated membrane versus one through the coated membrane, termed as the permeation reduction factor (PRF):

$$PRF = \frac{J_{\text{uncoated}}}{J_{\text{coated}}} . \tag{2.17}$$

The larger the PRF, the greater the efficiency of the coating material. Such membrane can be modeled as a membrane composed of two homogeneous layers. Its effective permeability Φ_{eff} is based on the sum of permeation resistances for each layer. For a two-layer membrane, the Φ_{eff} can be expressed as [125]:

$$\frac{L}{\Phi_{\text{eff}}} = \frac{L_1}{\Phi_1} + \frac{L_2}{\Phi_2} , \tag{2.18}$$

where indices denote layer *1* and *2*, while the membrane thickness $L=L_1+L_2$.

Shown in figure 2.6 is a schematic illustration of hydrogen diffusion through a two-layer membrane showing concentration profile [126]. In contrast to the heat conduction where the temperature profile is continuous through the multi-layer membrane, the hydrogen concentration profile is not continuous through multi-layer membrane. Instead, the hydrogen chemical potential is continuous. Usually one suppose that the hydrogen

concentration ratio at the interface is equal to the ratio of hydrogen solubilities in these materials [127]:

$$\frac{C_{1,i}}{C_{2,i}} = \frac{S_1}{S_2}, \tag{2.19}$$

where index *i* denotes the position at the interface.

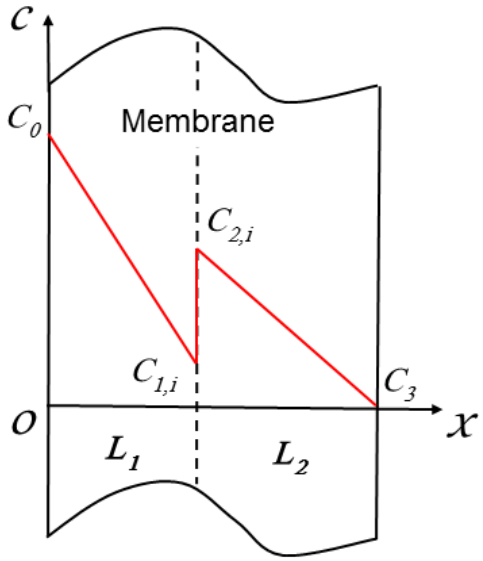

Figure 2.6 Hydrogen diffusion through a two-layer membrane showing concentration profile (replotted from [126]).

By measuring the steady-state permeation fluxes of coated and uncoated membranes one can obtain the permeability for the coating material using Eqs. (2.16) and (2.18). Further determination of solubility and diffusivity requires measurements of transient permeation fluxes. The time-lag method can be used to evaluate the diffusivity. For a two-layer membrane permeation, the time-lag t_l' can be described as [128]:

$$t_l' = [\frac{L_1^2}{D_1}\left(\frac{L_1}{6D_1} + \frac{\alpha L_2}{2D_2}\right) + \frac{L_2^2}{D_2}(\frac{L_1}{2D_1} + \frac{\alpha L_2}{6D_2})](\frac{L_1}{D_1} + \frac{\alpha L_2}{D_2})^{-1}, \tag{2.20}$$

where $\alpha = S_1/S_2$. The effective diffusivity D_{eff} can be obtained by measuring the time-lag t_2 of the two-layer membrane as $D_{\text{eff}} = (L_1+L_2)^2/6t_l'$. Then Eq. (2.20) can be reformed as [129]:

$$\frac{D_1}{D_2} = (1 + 3\beta\lambda)[(1 + \beta\lambda)(1 + \lambda)^2 \frac{D_2}{D_{\text{eff}}} - \lambda^2(3 + \beta\lambda)]^{-1}, \quad (2.21)$$

where $\beta = \Phi_1/\Phi_2$ and $\lambda = L_2/L_1$. Eqs. (2.20) and (2.21) are invariant to relative position of layers ($1 \leftrightarrows 2$), hence the transient permeation as well as the steady-state permeation are not influenced by the order of the layers.

The solubility is usually obtained from the measured Φ and D using $\Phi = DS$.

In summary, the measurements of steady-state permeation flux and time-lag of bare and coated membranes enable the evaluation of permeability, diffusivity and solubility of the coating material.

2.3 Steady-state PDP models

For plasma-driven permeation, three regimes are considered [130-131]: (1) diffusion-limited hydrogen release from both the upstream and downstream surfaces (to be referred to as the DD regime), (2) recombination-limited hydrogen release from the upstream surface and diffusion-limited hydrogen release from the downstream surface (to be referred to as RD regime), and (3) recombination-limited hydrogen release for both surfaces (to be referred to as RR regime).

The rate controlling process can be characterized by the dimensionless parameter W [130]:

$$W = \frac{d}{D}(J_0 K_r)^{1/2}, \quad (2.22)$$

where d is the implantation range, J_0 is the net implantation flux and K_r is the recombination coefficient on the upstream surface. Shown in figure 2.7 (a) is the normalized hydrogen concentrations as a function of W, assuming the ratio of the implantation range and the membrane thickness $\alpha = d/L = 10^{-6}$, and the surface conditions for the front surface and

back surface are the same ($\beta = K_r/K_l = 1$). C_0, C_p and C_1 are the hydrogen concentrations at the upstream surface, implantation range, and downstream surface, respectively.

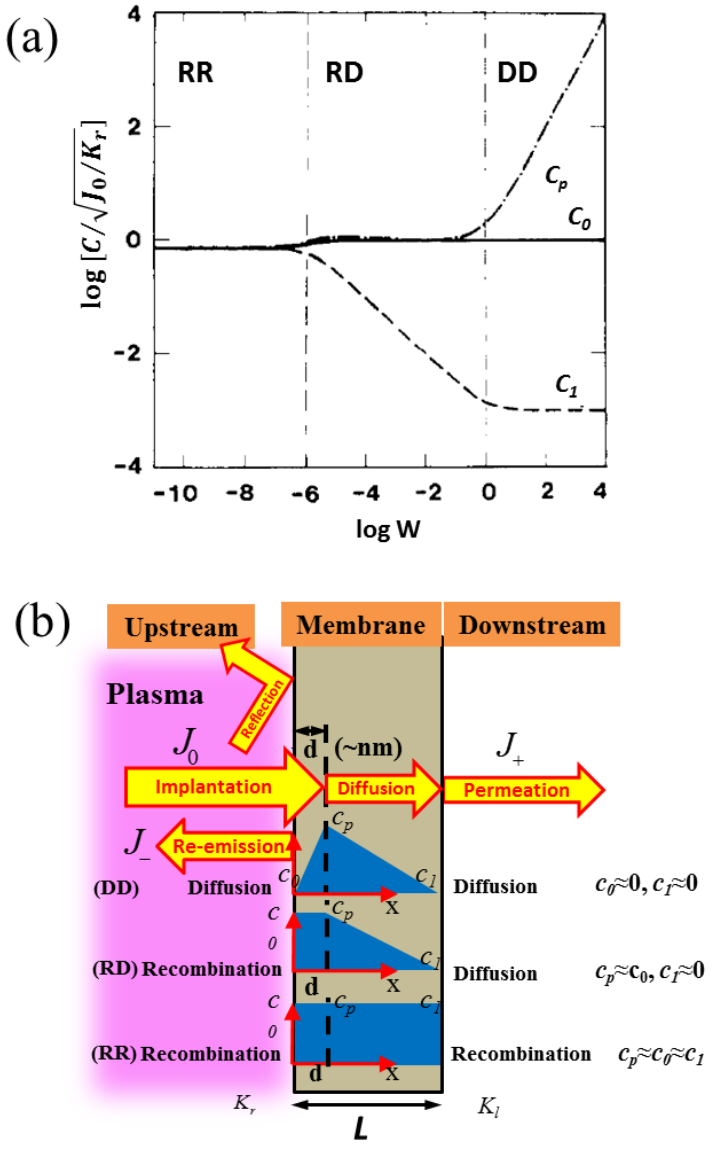

Figure 2.7 (a) Normalized hydrogen concentrations as a function of W (reedit from [130]) and (b) sketches of the steady-state hydrogen concentration profiles for the three regimes. C_0 is the hydrogen concentration at the plasma-side surface. C_1 is the hydrogen concentration at back-side surface while C_p is the hydrogen concentration at the implantation depth d.

The overall hydrogen transport is controlled by the slowest process and the parameter W may be regarded as a competition between the diffusion and recombination processes. For $W > 1$, which is possible when hydrogen is deeply implanted and diffusion is slow compared with surface recombination, the concentration is peaked at the implantation range d ($C_0 \approx 0$, $C_1 \approx 0$, as shown in figure 2.7(b)). This regime is the DD-regime. For $\alpha\beta < W < 1$, $C_p \approx C_0$ and $C_1 \approx 0$, indicating recombination-limited hydrogen release at the upstream surface and diffusion-limited hydrogen release at the downstream surface. If $W < \alpha\beta$, the hydrogen concentration is uniform throughout the membrane ($C_p \approx C_0 \approx C_1$) and PDP is in the RR regime.

The steady-state hydrogen plasma-driven permeation flux J_+ is given by the following formulae:

$$J_+ = \frac{d}{L} J_0 \qquad \text{(DD regime)} \qquad (2.23)$$

$$J_+ = \frac{D}{L}\sqrt{\frac{J_0}{K_r}} \qquad \text{(RD regime)} \qquad (2.24)$$

$$J_+ = \frac{K_l}{K_r + K_l} \qquad \text{(RR regime)} \qquad (2.25)$$

It should be pointed out that:

1) In the DD regime, $J+$ is not related to the surface recombination coefficients.

2) In the RD regime, J_+ is only affected by the upstream surface recombination coefficient, but not the downstream surface condition. Meanwhile, only in this regime J_+ is proportional to the square root of the net implantation flux J_0.

3) In both DD and RD regimes, J_+ is inversely proportional to the membrane thickness L. In contrast, J_+ is not affected by membrane thickness in RR regime.

2.4 Isotopic effects

Isotopic effects on hydrogen transport can be divided into two classes [132], i.e., intrinsic effects and synergistic effects. The former class is related to the differences in the transport properties of each of the individual isotopes, for example, the isotope dependence of the diffusivity, the heat of transport and trap strength. The latter class is due to the competition of the various isotopes for traps and the coupling of isotopes through the process of surface recombination.

It is commonly assumed that the ratio of diffusivity of hydrogen isotopes is equivalent to the inverse ratio of the square root of the masses of the isotopes:

$$\frac{D_{\mathrm{H}}}{D_{\mathrm{D}}} = \sqrt{\frac{m_{\mathrm{D}}}{m_{\mathrm{H}}}}, \tag{2.26}$$

where D and m are the diffusivity and mass of the respective isotope, and the subscripts H and D refer to hydrogen and deuterium, respectively. Similar expressions can be written for tritium and simplified as:

$$D_{\mathrm{H}} = \sqrt{2}D_{\mathrm{D}} = \sqrt{3}D_{\mathrm{T}}, \tag{2.27}$$

where the subscript T refers to tritium. These relationships between isotopes stem come from the classical rate theory, which relates diffusivity to atomic vibrational frequency and the frequency is inversely proportional to isotopic mass. The activation energy for diffusion is also assumed to be independent of the mass of the isotope. It is assumed that Eqs. (2.26) and (2.27) show a good approximation for both permeability and diffusivity. The solubility ($S = \Phi/D$), however, is governed by the heat of solution, which is independent of the mass of the isotope.

Taking into account the isotopic effects, the one-dimensional hydrogen transport process described in Eqs. (2.7)-(2.9) can be modified as [133]:

$$\frac{\partial C^j(x,t)}{\partial t} = D_j(T)\frac{\partial^2 C^j(x,t)}{\partial^2 x} - \sum_i \frac{\partial C_t^{ij}(x,t)}{\partial t} + G_j(x,t) \tag{2.28}$$

$$\frac{\partial C_t^{ij}(x,t)}{\partial t} = D_j(T)\frac{C(x,t)C_t^{ei}(x,t)}{\lambda^2} - C_t^{ij}(x,t)\nu_0 \exp(-\frac{U_t^i}{kT}) \tag{2.29}$$

$$C_t^{ei}(x,t) = C_t^{0i}(x) - \sum_j C_t^{ij}(x,t), \tag{2.30}$$

where $C^j(x,t)$ and $C_t^{ij}(x,t)$ are the concentrations of mobile j^{th} species and trapped j^{th} species in the i^{th} trapping site; D_j is the diffusion coefficient of the j^{th} species; T is the temperature; $G_j(x,t)$ is the hydrogen implantation profile of the j^{th} species; U_t^i is the de-trapping energy of the i^{th} trapping site; $C_t^{0i}(x)$ and $C_t^{ei}(x)$ are the concentrations of intrinsic and empty i^{th} trapping sites, respectively.

2.5 Summary

In this chapter, the physical mechanisms involved in the hydrogen permeation processes are introduced. When hydrogen particles impinge on solids, a fraction of them will be immediately reflected. For those hydrogen atoms implanted into the solid, they will either transport in the lattice of solids, or be trapped by defects and impurities. Finally, the mobile atoms will be released as molecules by surface recombination.

The theories on hydrogen isotopes transport in solids have been well developed and some hydrogen transport cases can be analytically or numerically solved. This PhD thesis work tries to utilize these theories to explain the observations in various permeation experiments. Using the equations describing the transient and steady-state hydrogen transport behavior, the permeation properties of various materials can be evaluated and the transport parameters such as diffusivity, permeability, solubility and surface recombination coefficient can be measured.

The steady-state PDP models show the relation between the net implantation flux J_0 and the permeation flux J_+ in different regimes, which indicate the potential methods to suppress J_+. Taking the RD regime as an example, one would consider either increasing the front surface recombination coefficient or increasing the membrane thickness to reduce J_+ for the first wall made by a certain material. However, as pointed out in Chapter 1, thermo-mechanical stresses would not allow us to consider thick first wall designs. This leads us to the use of coatings on the plasma-facing surfaces, which are presented in detail in Chapter 5 and Chapter 6.

Chapter 3

Experimental

3.1 Linear plasma facility: VEHICLE-1

3.1.1 The VEHICLE-1 facility

Hydrogen isotopes gas- and plasma-driven permeation experiments are carried out in a steady-state liner plasma facility: VEHICLE-1 [134]. Figure 3.1 shows (a) a picture and (b) a schematic diagram of VEHICLE-1 (the Vertical and Horizontal positions Interchangeable test stand for Components and Liquids for fusion Experiments). The VEHICLE-1 facility employs a 1 kW 2.45 GHz electrical cyclotron resonance (ECR) plasma source which can generate steady-state plasmas. These plasmas are guided by magnetic field, flowing linearly down to interact with the permeation membrane located in the middle of the test chamber. For well-diagnosed experiments, VEHICLE-1 is installed with two movable Langmuir probes, an optical spectrometer, a total and partial pressure gauge for plasma characterization, and equipped with an infrared pyrometer, thermocouples and a resistive heater for temperature measurements and control, respectively.

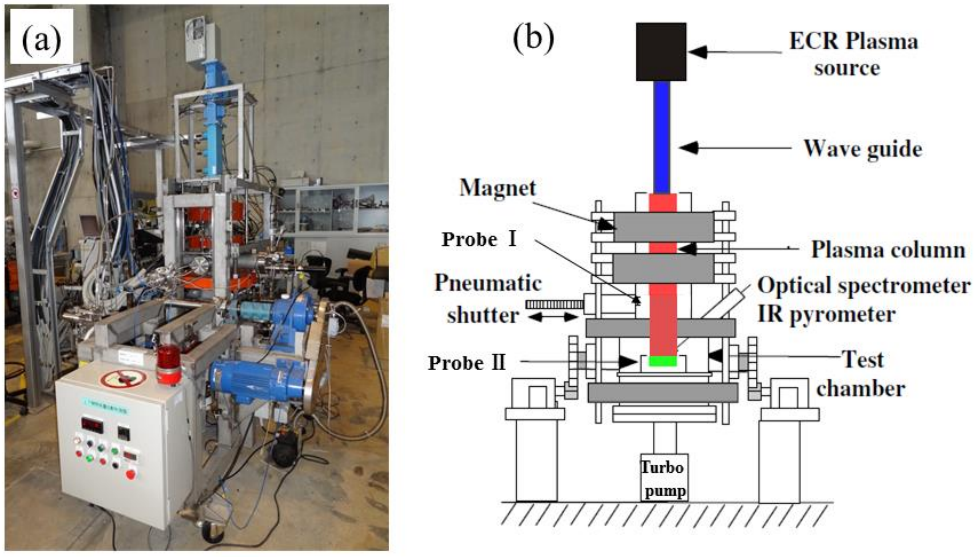

Figure 3.1 (a) The VEHICLE-1 facility and (b) a schematic diagram of the device.

3.1.2 ECR discharges

For ECR discharges, described in figure 3.2 [135], a circularly polarized microwave propagates along the DC magnetic field lines to a resonance zone, where the wave energy is absorbed by a collisionless heating mechanism. One or several magnetic field coils are used to generate a nonuniform, axial magnetic field within the chamber. When a low-pressure gas is introduced, the gas breaks down and a discharge forms inside the chamber. The plasma streams or diffuses along the magnetic field lines into a process chamber toward a wafer holder. Energetic ions and free radicals generated within the entire discharge region (source and process chambers) impinge on the wafer. ECR discharges are generally excited at microwave frequencies (e.g., 2.45 GHz), and the wave absorption requires application of a strong DC magnetic field (875 Gauss at resonance).

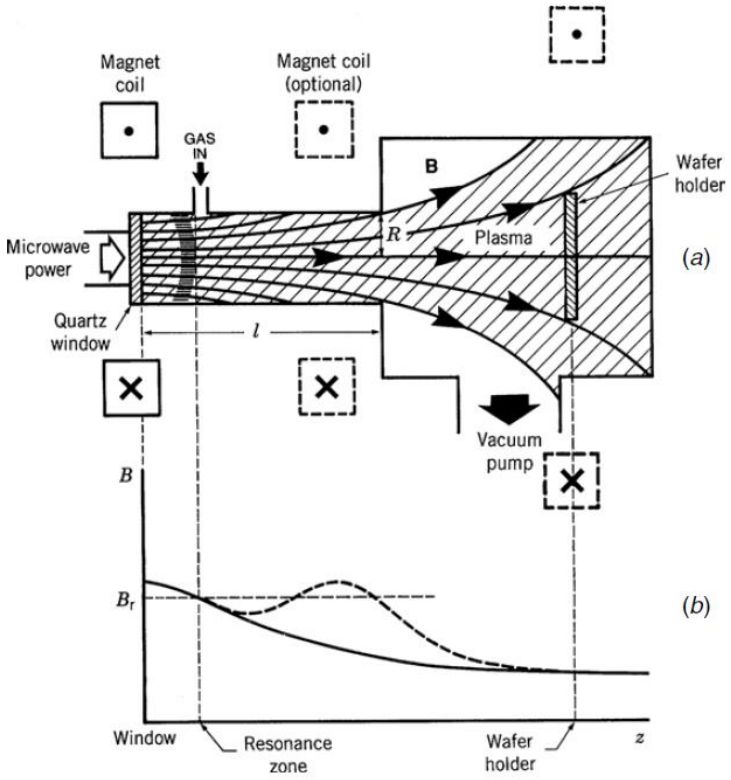

Figure 3.2 A typical ECR system: (a) geometric configuration and (b) axial magnetic field variation, showing resonance zone [135].

3.1.3 The permeation setup in VEHICLE-1

Shown in figure 3.3 is a schematic diagram of the GDP and PDP setup in VEHICLE-1. For GDP experiments, hydrogen (or deuterium) is introduced from a gas cylinder into the closed volume, the gas pressure is in the range of 10^3-10^5 Pa. An absolute pressure gauge has been used to measure the gas pressure at the high pressure side, while hydrogen permeation flux is detected by a quadrupole mass spectrometer (QMS) at the downstream side. A resistive heater is set beneath the membrane to control the temperature.

For PDP experiments, the plasma density is of the order of 10^{10} cm^{-3} and the electron temperature is ~5 eV measured by a Langmuir probe in front of the sample. The ion bombarding energy is set at -100 V by applying a negative DC bias on the sample. Plasma exposure is controlled by a pneumatically-operated shutter made of molybdenum, the opening time of which is ~20 ms.

For simultaneous bi-directional deuterium PDP and hydrogen GDP experiments, the gate valve is closed and an ultra-high vacuum variable leak valve is used to control the amount of hydrogen gas flow. It enables the gas flow of remarkably small amount with controllable leakage less than 6.7×10^{-9} Pa m^3/s. Therefore, the QMS Ⅱ can be operated with high pressure hydrogen gas filled in the closed volume. The PDP deuterium flux is detected by QMS Ⅱ, while the GDP hydrogen flux is detected by QMS Ⅰ through a 1 mm diameter orifice in the opposite direction.

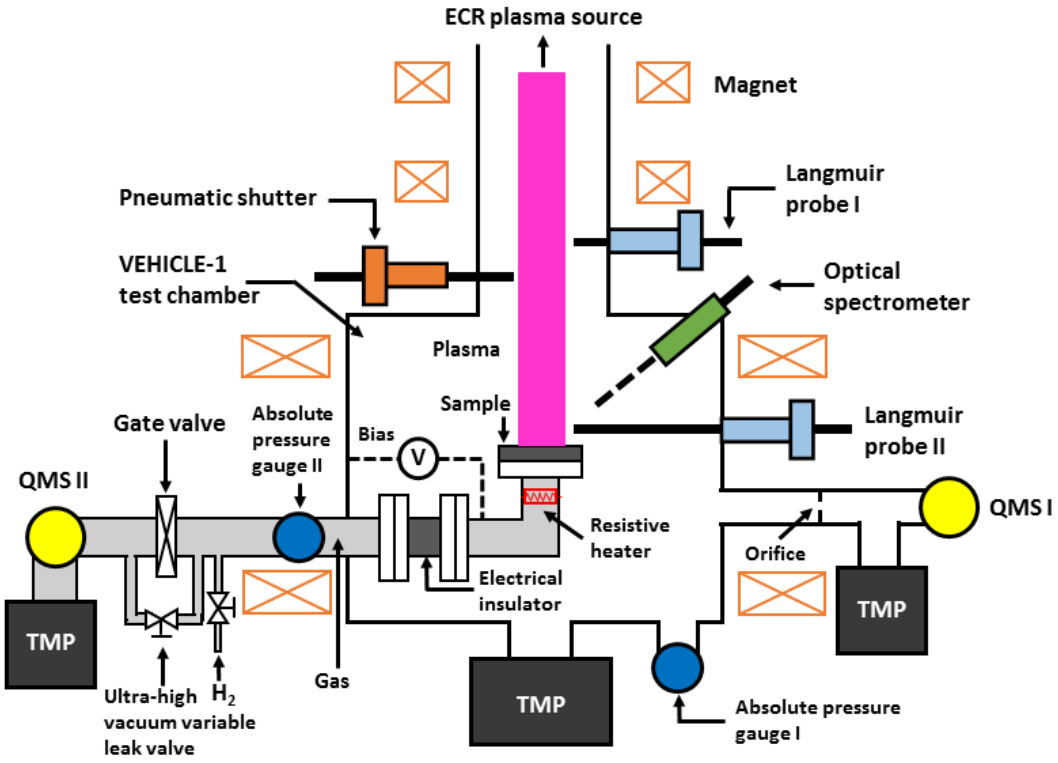

Figure 3.3 A schematic diagram of the gas-driven and plasma-driven permeation setup in VEHICLE-1. Two QMSs have been installed so that bi-directional permeation experiments can be performed.

3.1.4 Mass spectrometry

The mass spectrometer is essentially an instrument which can be used to measure the mass, or more correctly the mass/charge ratio, of ionized atoms or other electrically charged particles. The first mass spectrograph was invented by A. Dempster et al. [136], and have therefore been in continuous development over a long period. The principle of using electric and magnetic fields to accelerate and establish the trajectories of ions inside the spectrometer according to their mass/charge ratio is common to all the different designs.

The following description of Dempster's original mass spectrograph, as shown in figure 3.4 [137], is a simple illustration of these physical principles.

i) Magnetic sector spectrograph

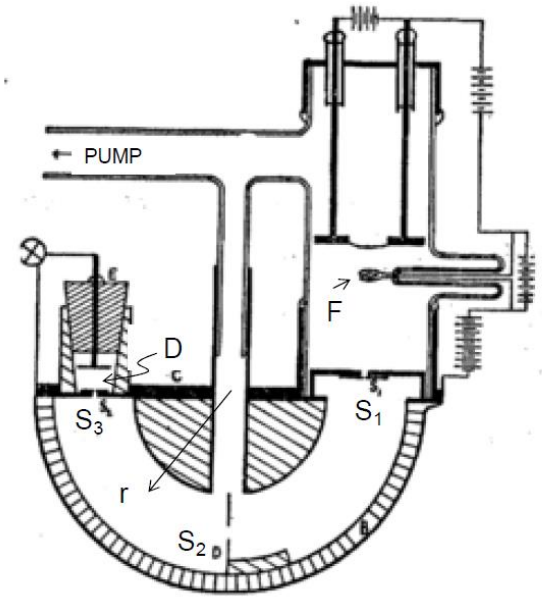

Figure 3.4 Dempster's mass spectrograph [137]. Atoms/molecules are first ionized by electrons emitted from the hot filament (F) and then accelerated towards the entrance slit (S_1). The ions then follow a semicircular trajectory established by the Lorentz force in a uniform magnetic field. The radius of the trajectory, *r*, is defined by three slits (S_1, S_2, and S_3). Ions with this selected trajectory are then detected by the detector (D).

Equating the Lorentz force with the centripetal force gives:

$$qvB = \frac{mv^2}{r}, \tag{3.1}$$

where q is the charge on the ion, B is the magnetic field, m is the mass of the ion and r is the radius of the ion trajectory.

Classically, the speed of the ion, *v*, is related to its accelerating voltage *V*, by

$$\frac{1}{2}mv^2 = qV. \tag{3.2}$$

Eliminating *v* from Eqs. (3.1) and (3.2) gives:

$$\frac{m}{q} = \frac{B^2r^2}{2V}. \tag{3.3}$$

Therefore, for fixed radius of curvature, an ion with a particular mass/charge ratio (*m/q*) can be isolated and measured by an appropriate combination of magnetic field *B* and accelerating voltage *V*. In these early designs, it was convenient to fix *B* (using a permanent magnet) and scan *V* in order to measure the mass spectrum of the different species present in the vacuum chamber of the spectrometer.

ii) Quadrupole mass spectrometer

In practice, it is difficult to achieve very stable and spatially uniform magnetic fields, especially with permanent magnets. These difficulties can lead to degradation of the mass resolution and drifts in the calibration of the instrument. In addition, the presence of stray magnetic fields can affect other instruments that may be used in conjunction with a mass spectrometer. In the early 1950's it was found that the use of magnetic fields could be eliminated by a design which uses alternating quadrupole electric fields rather than magnetic fields, hence the name quadrupole mass spectrometer. This is the design that is currently in widespread use for residual gas analysis. It is highly stable and has excellent mass resolution. With high sensitivity electron multipliers, it can measure partial pressures down to 10^{-12} Pa.

A quadrupole mass spectrometer (QMS) consists of an ionizer (bombardment by electrons from a hot filament), an ion accelerator, and a mass filter consisting of four parallel metal rods arranged as shown in the figure 3.5 [137]. Two opposite rods have an applied potential of (U + Vcos(ωt)) and the other two rods have a potential of -(U + Vcos(ωt)), where U is a DC voltage and Vcos(ωt) is an AC voltage. The applied voltages

affect the trajectory of ions traveling down the flight path centered between the four rods. For given DC and AC voltages, only ions of a certain mass/charge ratio pass through the quadrupole filter and all other ions are thrown out of their original path. A mass spectrum is obtained by monitoring the ions passing through the quadrupole filter as the voltages on the rods are varied. There are two methods: varying ω and holding U and V constant, or varying U and V with (U/V) fixed for a constant angular frequency, ω.

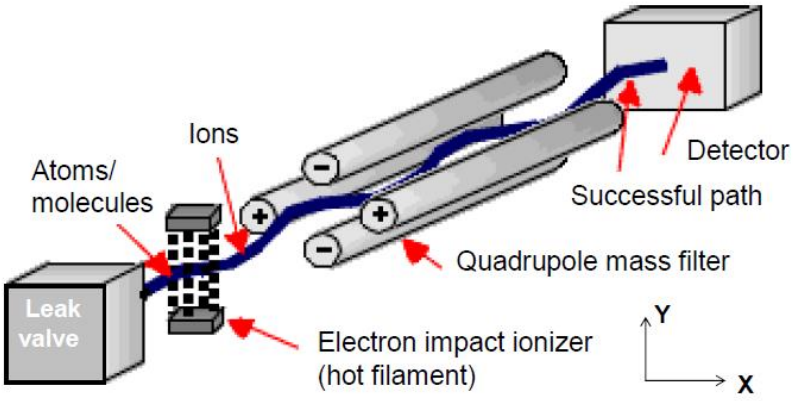

Figure 3.5 Schematic of a quadrupole mass filter [137].

The general principle of operation of the mass filter can be visualized qualitatively as follows: light ions (low mass/charge ratio) are able to follow the alternating component of the field. For the X-direction, those ions will stay in phase with the RF drive, gain energy from the field and oscillate with increasingly large amplitude until they encounter one of the rods and are discharged. Therefore the X-direction is a high-pass mass filter: only high masses will be transmitted to the other end of the quadrupole without striking the X-electrodes. On the other hand, in the Y-direction, heavy ions will be unstable because of the defocusing effect of the DC component, but some lighter ions will be stabilized by the AC component if its magnitude is such as to correct the trajectory whenever its amplitude tends to increase. Thus the Y-direction is a low-pass mass filter: only low masses will be transmitted to the other end of the quadrupole without striking the Y electrodes. By a suitable choice of RF/DC ratio, the two directions together provide a mass filter which is capable of resolving individual atomic masses.

The attractive features of the quadrupole as a mass analyzer are evident from the above discussion: the quadrupole provides a convenient filter which can be tuned to the desired mass by varying the amplitude of the RF voltage, V; the mass selectivity (resolution) can also be varied electronically by simply adjusting the DC/RF ratio. Simultaneously varying the amplitude of the DC and RF voltages (at fixed ω) allows the entire mass spectrum to be scanned.

3.1.5 Emission spectroscopy and line radiation

Emission spectroscopy can provide information about the particle densities and temperatures by a measurement of the atomic line intensities or the line profiles [68, 138]. The emission is determined by electron impact excitation and radiative decay.

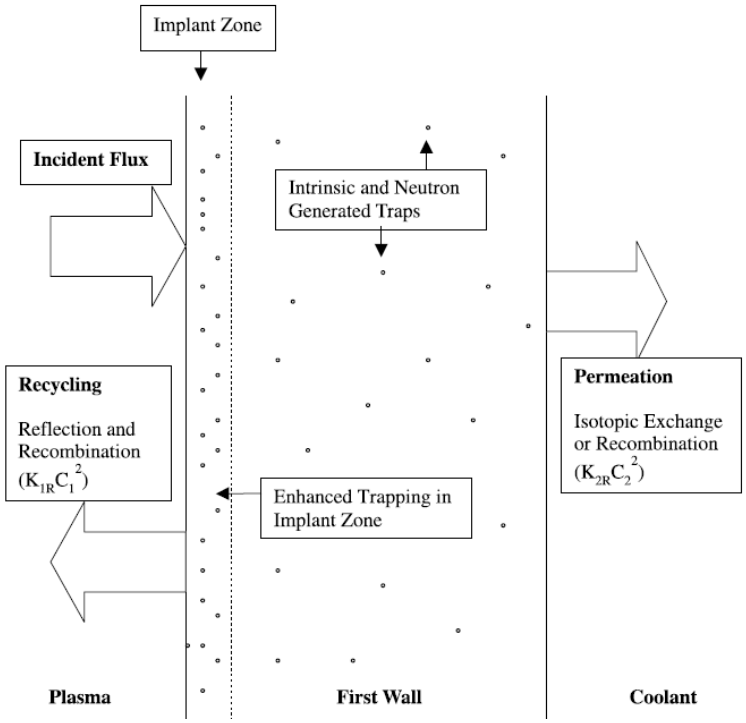

Figure 3.6 Hydrogen recycling process at the surface of fusion reactor plasma-facing materials [115].

Figure 3.6 shows the hydrogen recycling process at the surface of plasma-facing materials [115]. Recycling is defined as the rate of return of the cold hydrogen to the plasma, controlling the fueling rate and lowering the plasma temperature. Recycling includes the reflection and re-emission hydrogen fluxes.

In the case of ion beam experiments, assuming that the background level is low, the partial pressure of hydrogen recycled due to re-emission and reflection from the target material is generally used as the measure of recycling. In the case of plasma experiments, however, because hydrogen is the feed gas for plasma generation and its partial pressure is rather high, partial pressure measurements would not serve for the same purpose. Therefore, spectroscopic measurements focused on the H_α light have been conducted in the present work. To briefly mention the atomic physics processes related to the H_α spectroscopy, electron impact excitation of hydrogen up to n=3 followed by relaxation down to n=2, where n is the principal quantum number, induces photon emission with the particular wave length of 656.3 nm, referred to as H_α light. There are two origins of H_α photons: one from reflected hydrogen atoms; the other from those generated by the dissociation of reemitted molecules. Therefore, one expects that the intensity of H_α light may be used as the measure of hydrogen recycling and is expressed as [139]:

$$I_{H_\alpha} = n_e n_H < \sigma v > \tag{3.4}$$

where $I_{H\alpha}$ is the H_α light intensity, n_e is the electron density, n_H is the atomic hydrogen density and $< \sigma v >$ is the excitation rate coefficient.

In addition to H_α spectroscopy, visible light measurements have been conducted in the VEHICLE-1 device. One finds in figure 3.7 that the visible light is essentially composed of H_α and H_β lights under the typical experimental conditions (ECR power: ~400 W, hydrogen gas pressure: ~0.1 Pa, DC bias: -100 V). Therefore, the visible light intensity profile to be shown in Chapter 4 may be treated as an indicator of hydrogen recycling.

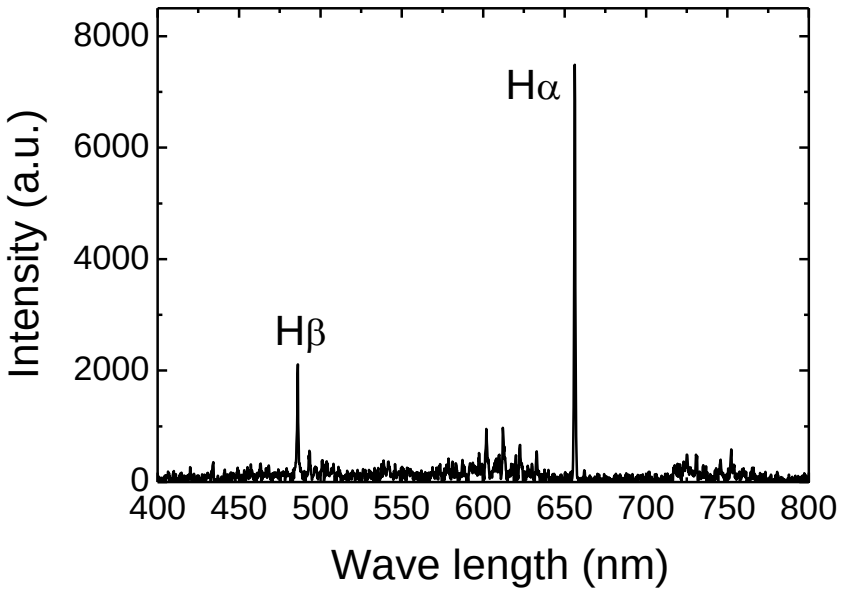

Figure 3.7 Major components in the visible light wave length range (data taken in the VEHICLE-1 device).

3.2 Plasma characterization

3.2.1 Langmuir probe

The electron density (n_e) and electron temperature (T_e) can be measured by Langmuir probes. A Langmuir probe consists of a bare wire or metal disk (figure 3.8), which is inserted into a plasma and electrically biased with respect to a reference electrode (shown in figure 3.9) to collect current-voltage I-V characteristic curve as the applied bias voltage sweep from a negative to a positive potential [140-141].

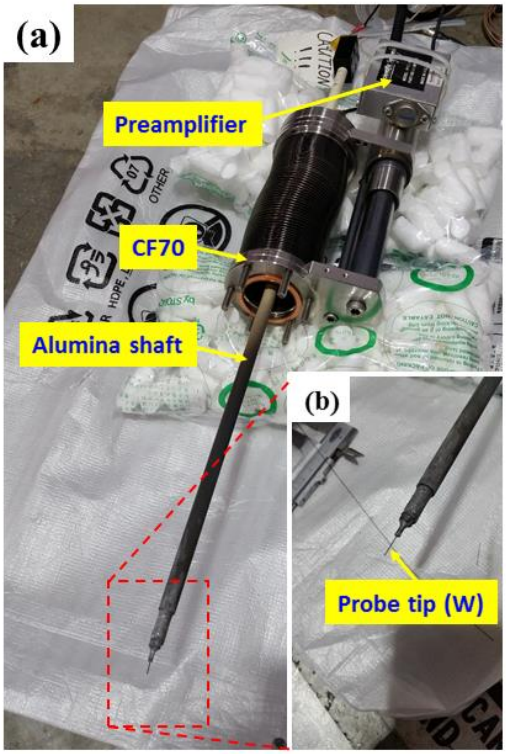

Figure 3.8 The Langmuir probe used in VEHICLE-1.

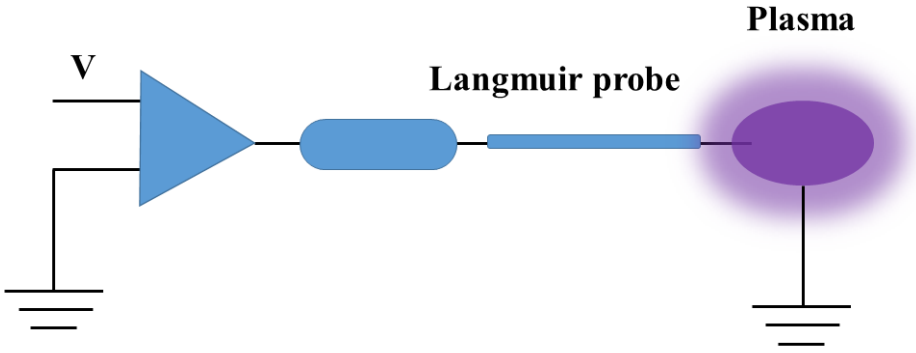

Figure 3.9 A simple Langmuir probe schematic.

The plasma parameters including n_e and T_e can be obtained by analyzing the I-V characteristic curve. The I-V characteristic curve, as described in figure 3.10, can be divided into three regions [141-142]: (a) the electron saturation region, (b) the electron retardation region, and (c) the ion saturation region.

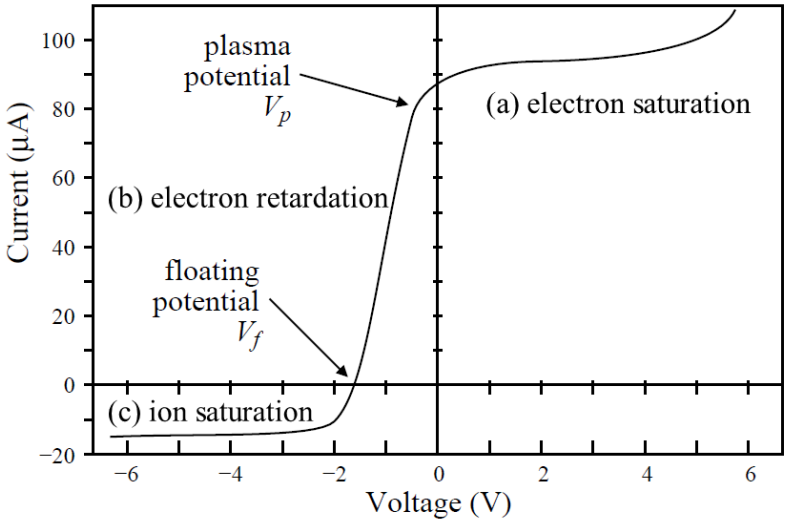

Figure 3.10 A characteristic I-V curve of Langmuir probe [141].

(a) In the electron saturation region the probe is biased positively with respect to the plasma potential. Negative ions and electrons are attracted to the probe and electron saturation occurs.

(b) When the probe is biased negatively with respect to the plasma potential the probe attracts electrons which are energetic enough to overcome the potential barrier. If the electron distribution is in thermal equilibrium the electron current is exponential with respect to the applied voltage and the slope of the exponential region yields the electron temperature.

(c) For increasingly negative potentials with respect to the plasma potential the point is reached where no electrons reach the probe and only positive ions are collected. This region yields the ion number density in the plasma.

The way in which the I-V characteristic is analyzed is vital to the accuracy of the measured plasma parameters. The zero second derivative method is a simple and efficient analysis routine to calculate the plasma parameters including plasma potential (V_p), floating potential (V_f), electron temperature (T_e) and electron density (n_e).

Plasma potential, V_p: The I-V characteristic goes through an inflection at the plasma potential. At the plasma potential there is no potential between the probe and the plasma and the current measured is due to thermal electrons and ions in the plasma. The inflection point on the I-V characteristic can be accentuated by taking the first and second derivative of the current with respect to the applied voltage. The first derivative goes through a maximum at the plasma potential and the second derivative is equal to zero at the plasma potential.

Floating potential, V_f: The negative potential which develops on a floating probe is known as the floating potential. There is no net current flow through the probe and V_f will repel sufficient electrons to equate the ion and electron fluxes. The voltage point on the I-V curve is the point at which the net current (I) is equal to zero.

Electron temperature, T_e: The electron temperature is calculated by taking the current measured at the plasma potential, $I(V_p)$ and dividing it by the integral of the I-V curve from V_f to V_p, [143]:

$$\frac{I(V_p)}{\int_{V_f}^{V_p} I(V)dv} = \frac{1}{kT_e}\,. \tag{3.5}$$

This method of calculating T_e is less sensitive to noise than the more common technique of calculating T_e by dividing $I(V_p)$ by the derivative of the I-V characteristic.

Electron density, n_e: The electron density is calculated from the current measured at the plasma potential using the following equation [143]:

$$n_e = \frac{I(V_p)}{A_p}\left(\frac{2\pi m_e}{e^2 kT_e}\right)^{\frac{1}{2}}, \tag{3.6}$$

where A_p is the area of the probe, m_e is the mass of electron and e is the electronic charge.

3.2.2 Plasma parameters in VEHICLE-1

The data of n_e and T_e in VEHICLE-1 measured by the Langmuir probe are shown in figure 3.11 as a function of ECR power and in figure 3.12 as a function of hydrogen pressure, respectively. For the ECR power dependence measurements, the hydrogen pressure is maintained at ~0.2 Pa and DC bias is set at -100 V. The electron density increases with increasing ECR power, which, however, is not the case with the electron temperature. In figure 3.11, the ECR power and DC bias are set at 200 W and -100 V, respectively. The plasma density increases with increasing hydrogen gas pressure while the electron temperature shows an opposite trend.

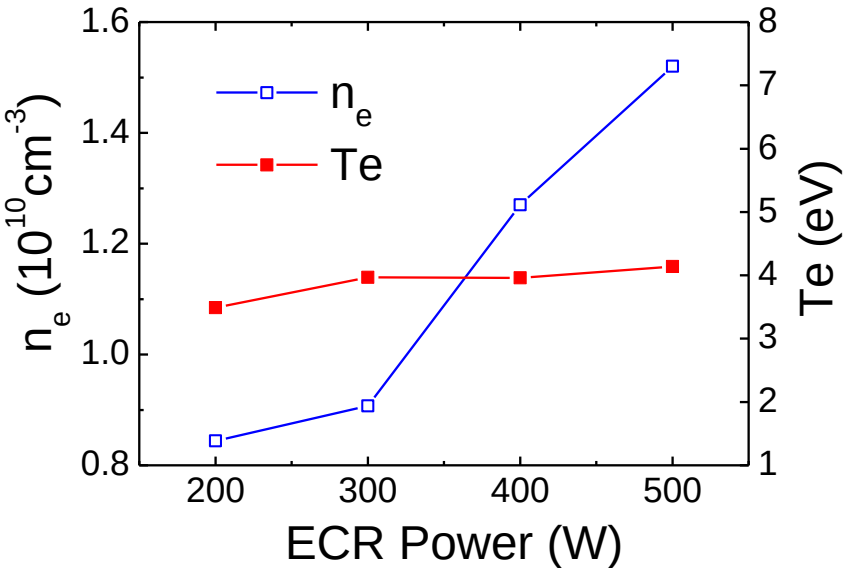

Figure 3.11 Plasma density and electron temperature as a function of ECR power.

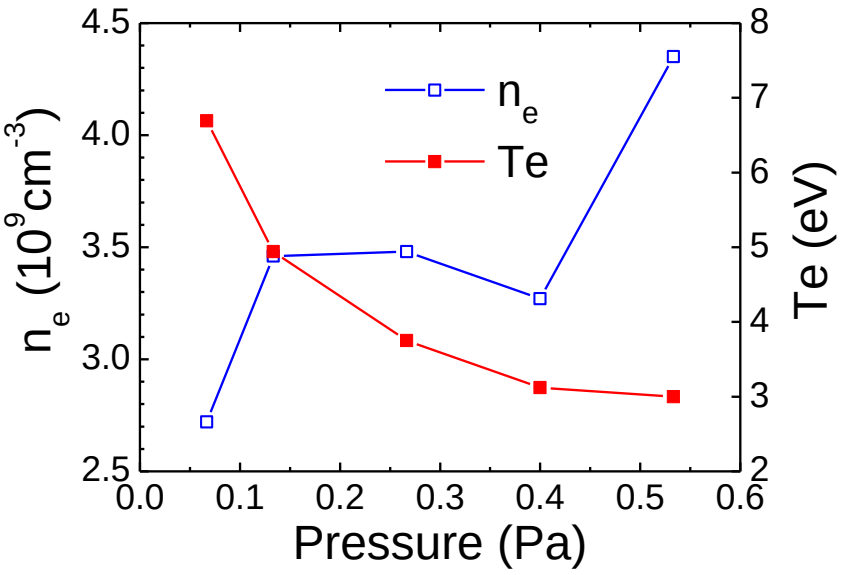

Figure 3.12 Plasma density and electron temperature as a function of hydrogen pressure.

The ion species mix of the hydrogen plasmas has been estimated in our previous work using a zero-dimensional model (as shown in figure 3.13) [144]. The modeling results indicate that H_3^+ is the dominant ion species at the electron temperature and neutral hydrogen gas pressure (~0.1 Pa) in our experiments. The concentration of H^+ increases as the increase of electron temperature and becomes the dominant species when the electron temperature is higher than 4 eV.

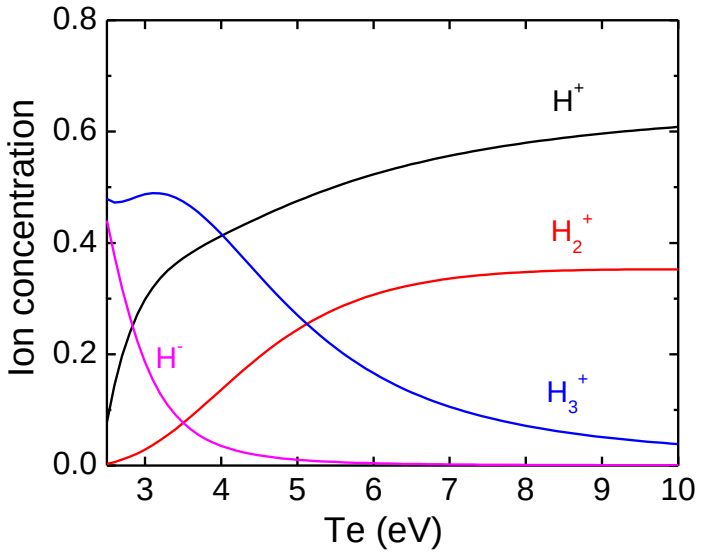

Figure 3.13 Estimation of the ion species mix using the zero-dimensional model [144].

Then the net implantation flux J_0 into a membrane at a certain bias voltage can be expressed in the following manner [145]:

$$J_0 = \sum_{j=1}^{3} \frac{(1-R_{Nk})jN_k}{2} \sqrt{\frac{k(T_e+T_i)}{m_{H_j^+}}}, \tag{3.7}$$

where k is the Boltzmann's constant, T_e and T_i ($T_i \approx 0$) are the electron and ion temperatures, respectively, and R_{Nk} is the particle reflection coefficient calculated from the Monte Carlo program, SRIM (see figure 2.2 of Chapter 2). The net implantation flux is estimated to be of the order of $10^{15} \sim 10^{16}$ H cm^{-2} s^{-1} for VEHICLE-1 hydrogen plasmas.

As presented in Section 1.3 of Chapter 1, the cross-field particle flux to the first wall of a fusion power reactor has been estimated to be of the order of 10^{16} atoms cm^{-2} s^{-1}. It is thus believed that the plasma bombardment conditions in VEHICLE-1 are relevant to those to be seen in the first wall environment of fusion reactors.

3.3 Thermal desorption spectroscopy

Thermal desorption spectroscopy (TDS), also known as temperature programmed desorption (TPD), is the method of observing desorbed gases from a sample. The gas is desorbed by heating the sample while the pressure in the system is recorded, the resulting pressure-time curve will be referred to as a "desorption spectrum". If the temperature-time relation for sample heating is suitably controlled, the desorption spectra can be analyzed to provide information on various adsorption parameters. This information includes [146]: (1) the number of the various desorbing phases and the population of the individual phases, (2) the activation energy of desorption of the various phases, and (3) the order of the desorption reaction.

In this PhD work, the deuterium retention data are taken by the TDS method. Shown in figure 3.14 is the TDS facility which employ an infrared heater with a maximum output power of ~1500 W. The samples can be heated to a temperature of ~650 ℃ at a ramp rate of 0.3-3 ℃/s. The temperature is measured by a thermocouple attached to the sample surface. The amount of retained deuterium is determined by integrating the partial pressures of D_2 and HD during thermal desorption.

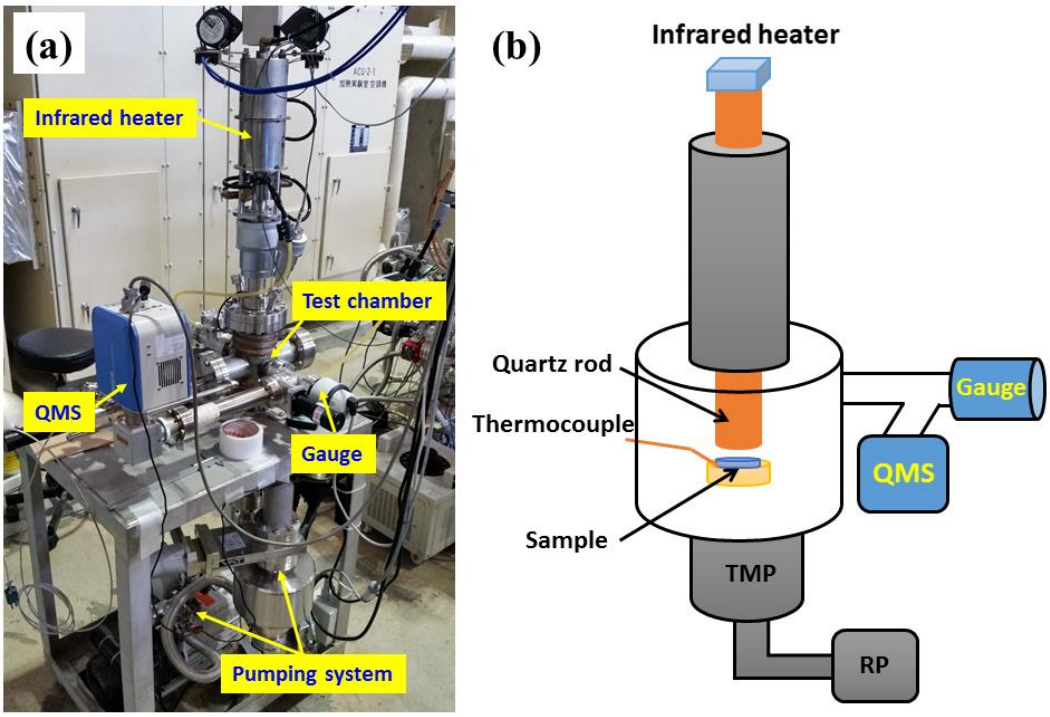

Figure 3.14 (a) The TDS facility and (b) a schematic diagram of the device.

3.4 Secondary ion mass spectrometry

Secondary ion mass spectrometry (SIMS), as shown in figure 3.15, is a technique used to analyze the composition of solid surfaces and thin films by sputtering the surface of the specimen with a focused primary ion beam and collecting and analyzing ejected secondary ions [147]. The mass/charge ratios of these secondary ions are measured with a mass spectrometer to determine the elemental, isotopic, or molecular composition of the surface. Due to the large variation in ionization probabilities among different materials, SIMS is generally considered to be a qualitative technique, although quantitation is possible with the use of standards. SIMS is the most sensitive surface analysis technique, with elemental detection limits ranging from parts per million to parts per billion. In this work, the

deuterium depth concentration profile in tungsten coated F82H steel after PDP has been measured by SIMS. A brief overview of the SIMS technique are introduced as follows.

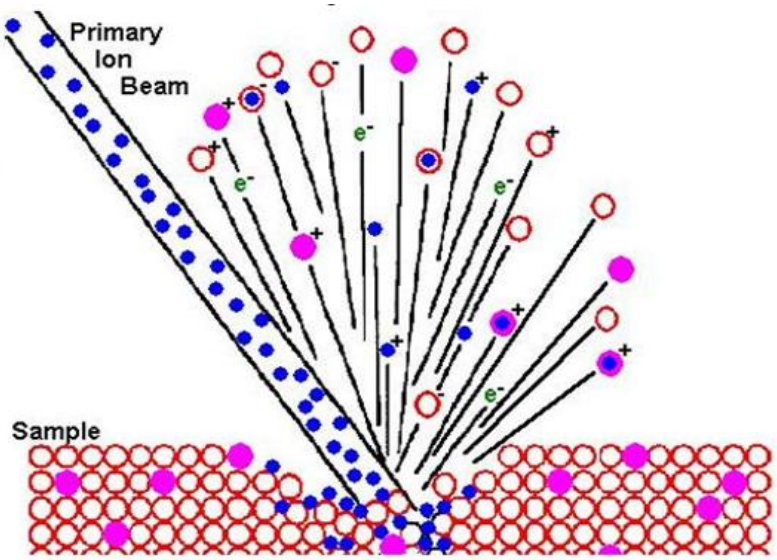

Figure 3.15 The principle of the secondary ion mass spectrometry.

Generally, a secondary ion mass spectrometer consists of (1) a primary ion gun generating the primary ion beam, (2) a primary ion column, accelerating and focusing the beam onto the sample, (3) high vacuum sample chamber holding the sample and the secondary ion extraction lens, (4) a mass analyzer separating the ions according to their mass to charge ratio, and (5) a detector. Static SIMS concentrates on the first top monolayer, providing mostly molecular characterization, while in dynamic SIMS mode, bulk composition and depth distribution of trace elements are investigated with a depth resolution ranging from sub-nm to tens of nm. Shown in figure 3.16 is a schematic diagram of a typical dynamic SIMS instrument [148].

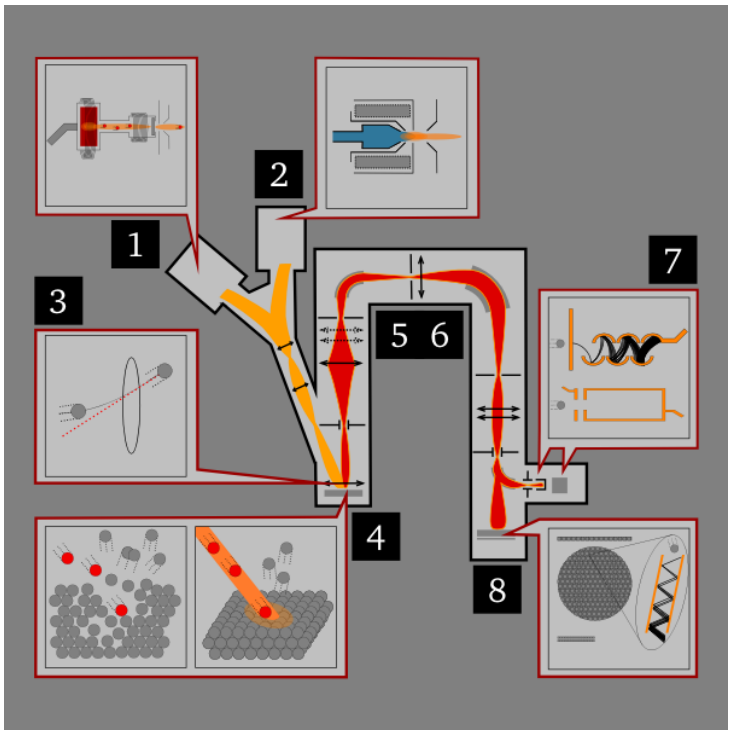

Figure 3.16 Schematic of a typical dynamic SIMS instrument [148]. High energy (usually several keV) ions are supplied by an ion gun (1 or 2) and focused on to the target sample (3), which ionizes and sputters some atoms off the surface (4). These secondary ions are then collected by ion lenses (5) and filtered according to atomic mass (6), then projected onto an electron multiplier (7, top), Faraday cup (7, bottom), or CCD screen (8).

Three types of ion guns are employed [148]. In one, ions of gaseous elements are usually generated with duoplasmatrons or by electron ionization, for instance noble gases (Ar^+, Xe^+) or oxygen (O^-, O_2^+, O_2^-). This type of ion gun is easy to operate and generates roughly focused but high current ion beams. A second source type, the surface ionization source, generates Cs^+ primary ions [149]. Cesium atoms vaporize through a porous tungsten plug and are ionized during evaporation. Depending on the gun design, fine focus or high current can be obtained. A third source type, the liquid metal ion gun,

e.g. gallium, operates with metals or metallic alloys, which are liquid at room temperature or slightly above. The liquid metal covers a tungsten tip and emits ions under influence of an intense electric field. The choice of the ion guns depends on the required current, the beam dimension and the injected secondary ions to be analyzed. Oxygen primary ions are often used to investigate electropositive elements due to an increase of the generation probability of positive secondary ions, while cesium primary ions often are used when electronegative elements are being investigated. For short pulsed ion beams in static SIMS, liquid metal ion guns are most often deployed for analysis.

Depending on the SIMS type, there are three basic analyzers available [150]: sector, quadrupole, and time-of-flight. A sector field mass spectrometer uses a combination of an electrostatic analyzer and a magnetic analyzer to separate the secondary ions by their mass to charge ratio. A quadrupole mass analyzer separates the masses by resonant electric fields, which allow only the selected masses to pass through. The time of flight mass analyzer separates the ions in a field-free drift path according to their velocity.

3.5 Sample preparation

The F82H permeation samples are cut from the F82H plates used in the JFT-2M tokamak at JAEA [151]. The samples are prepared in the same dimensions as those commercially available conflat (CF) flanges with an outer diameter of 70 mm, except that a circular area of ~35 mm in diameter inside the knife-edge is machined down to thicknesses of 0.5 mm to 2 mm to use as permeation membranes, as shown in figure 3.17 (a) and (b). Plasma-facing surfaces of the membranes are mechanically polished and then cleaned in an ultrasonic bath. α-Fe samples are also prepared in the same way used in some of the experiments as a reference material.

For the PDP experiments, the plasma-facing side of the membrane is covered by a stainless steel mask which has a 35 mm diameter opening in the middle. Although the

diameter of the cylindrical plasma column is ~70 mm, only the central membrane area of the sample is exposed to the plasma, as shown in figure 3.17 (c) and (d).

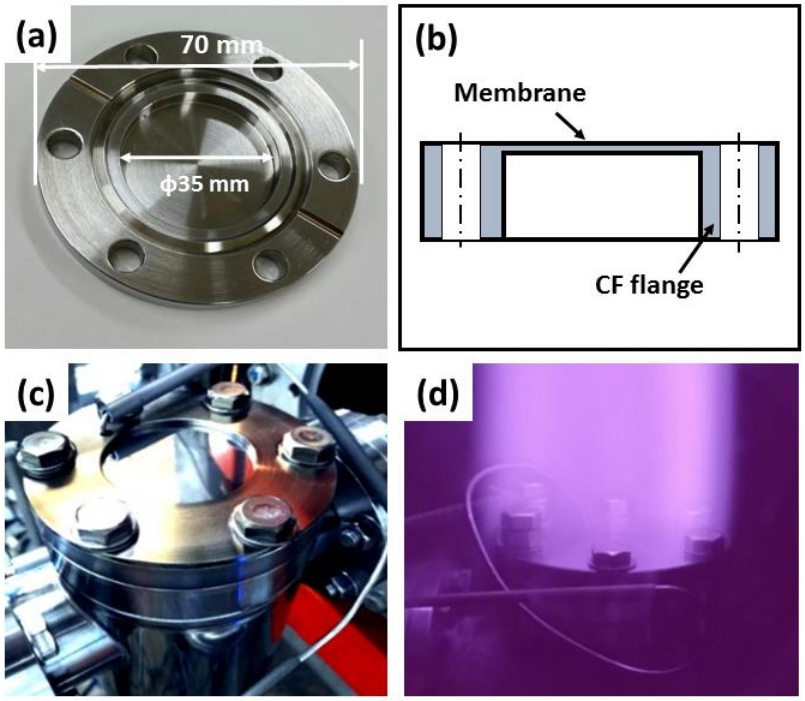

Figure 3.17 (a) A picture of the permeation membrane sample with dimensions, (b) a schematic diagram of the permeation membrane, (c) a sample installed with a mask and (d) a sample exposed to hydrogen plasma in the VEHICLE test chamber.

The concept of the vacuum plasma spraying process is illustrated in figure 3.18 [98]. The vacuum plasma-sprayed tungsten (VPS-W) coatings used in this work are prepared on the surface of F82H flanges. Blast treatment has been carried out for the F82H substrate surface before vacuum plasma spraying process. The thickness of VPS-W coatings varies from 40 μm to 200 μm. The deposition temperature is ~600 ℃, which is below the F82H phase transformation temperature (~750 ℃) so as to keep its good performance. The

average size of W powder particles is ~25 µm. The average density of VPS-W coatings has been evaluated to be ~90% of bulk W.

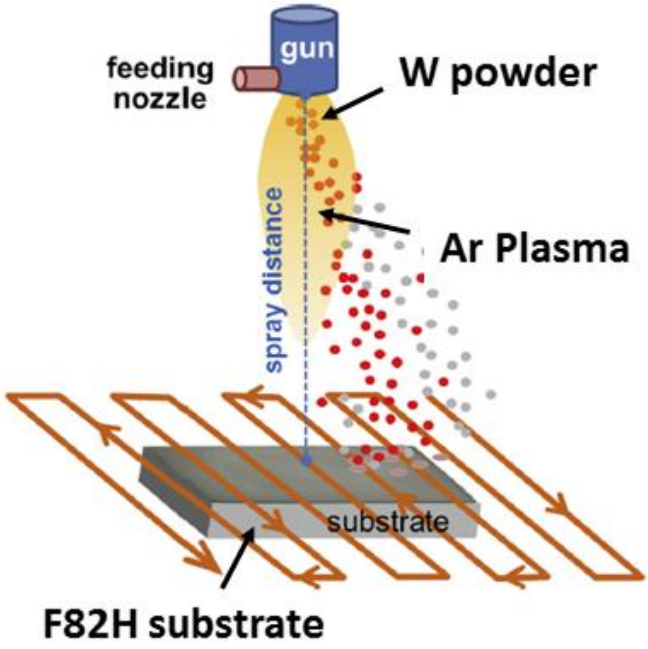

Figure 3.18 A schematic diagram of the vacuum plasma spraying process [98].

Figure 3.19 shows the schematic diagram of the physical sputter-deposition process [152]. The sputter-deposited tungsten (SP-W) coatings are deposited on the F82H flanges surface as well. The F82H substrate surface is mechanically polished before sputtering. The thickness of SP-W coatings varies from ~0.5 µm to ~5 µm. The temperature of F82H substrate is kept at ~300 ℃ during argon ions sputter-deposition process. The argon gas pressure is ~0.19 Pa. Dense and pore-free W coatings can be produced by this technique. The density of SP-W coatings is evaluated from the weight increase and film volume after W deposition, which is 19.2 g/cm^3, ~99.5% of bulk W.

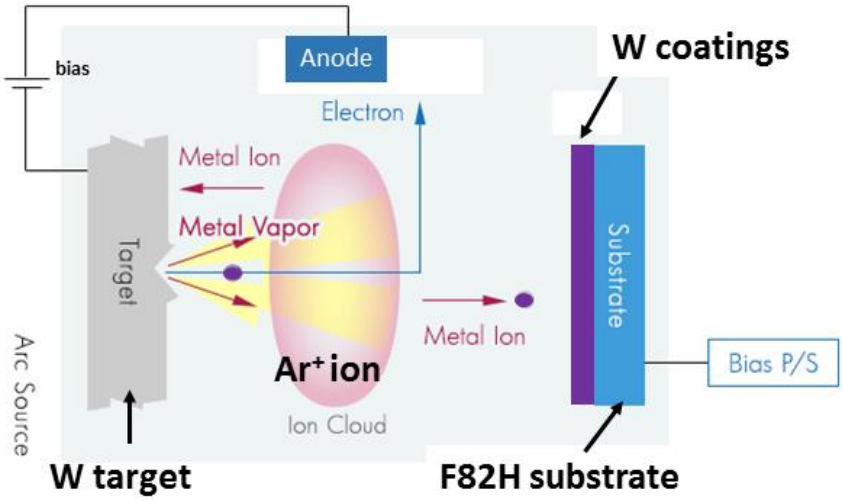

Figure 3.19 A schematic diagram of the physical sputter-deposition process [152].

3.6 Summary

In this chapter, a laboratory-scale steady-state plasma facility VEHICLE-1 has been introduced. The plasma parameters in VEHICLE-1 have been characterized. Taking into account the ion species mix and surface particle reflection, the plasma bombardment conditions in VEHICLE-1 are believed to be relevant to the first wall environment of fusion reactors. The thermal desorption spectroscopy and secondary ion mass spectrometry are briefly reviewed. Samples including bare F82H membranes, VPS-W coated F82H and SP-W coated F82H membranes are prepared. Hydrogen isotopes gas- and plasma-driven permeation data obtained in the VEHICLE-1 facility will be presented in Chapter 4, Chapter 5 and Chapter 6.

Chapter 4

Bi-directional hydrogen isotopes gas- and plasma-driven permeation through a reduced activation steel alloy F82H

In this chapter, hydrogen and deuterium gas- and plasma-driven permeation through a reduced activation steel alloy F82H have been systematically investigated using the VEHICLE-1 facility. Hydrogen and deuterium transport parameters for F82H have been measured from both GDP and PDP experiments. Isotopic effects have been discussed. Simultaneous bi-directional hydrogen isotopes (H/D) permeation through F82H has been demonstrated experimentally for the first time under controlled experimental conditions.

4.1 Microstructure characterization of F82H

Figure 4.1 shows the SEM (scanning electron microscope) image of the polished F82H surface. Some lines with width of a few tens of nanometers are shown on the membrane surface, which is the result of imperfect polishing. EDS (dispersive X-ray spectroscopy) analysis yields the surface elemental composition of: C (0.1 wt%), O (0.1 wt%), Cr (8.5 wt%), W (2.6 wt%) and Fe (88.7 wt%).

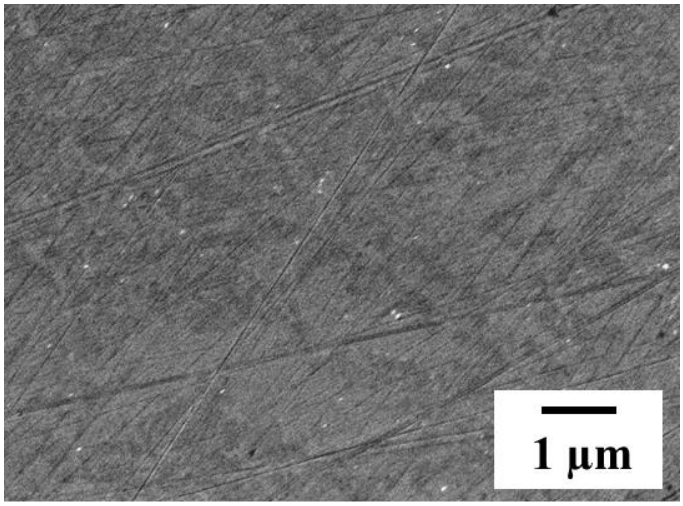

Figure 4.1 A SEM image of the polished F82H surface.

4.2 Gas-driven permeation

4.2.1 Characteristics of GDP through F82H

The GDP data have been taken for F82H membranes at temperatures between 150 ℃ and 500 ℃. Shown in figure 4.2 are the steady-state deuterium GDP fluxes as a function of upstream gas pressure, from which one can find a linear relation between the GDP flux and the square-root of upstream pressure at all the temperatures examined in this study.

Shown in figure 4.3 are the steady-state deuterium GDP fluxes through 0.5 mm, 1 mm and 2 mm thick F82H membranes under upstream gas pressure of ~10^4 Pa, which is relevant to the tritium dissociation pressure from FLiBe at ~530 ℃ and at a (T/M) concentration of ~0.1 ppm [84]. The membrane temperature is 490 ℃. It indicates that the permeation flux is inversely proportional to the membrane thickness.

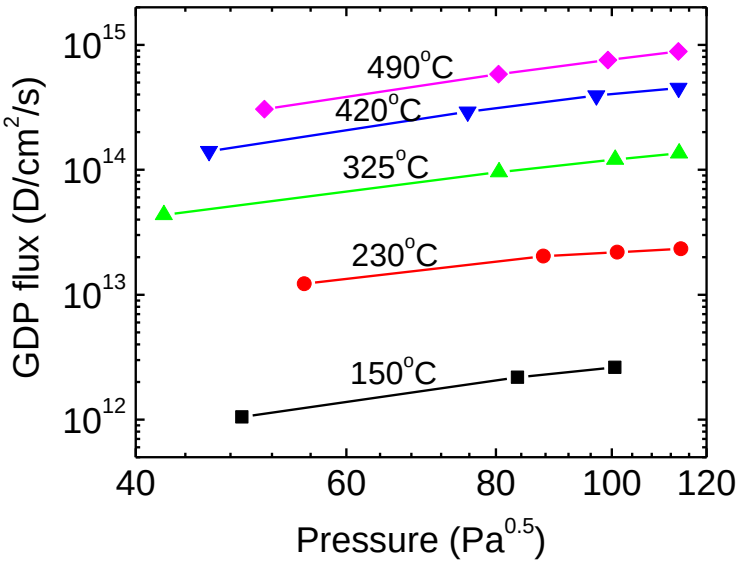

Figure 4.2 Pressure dependence of deuterium GDP flux through a 0.5 mm thick F82H membrane in the temperature range of 150-500 ℃.

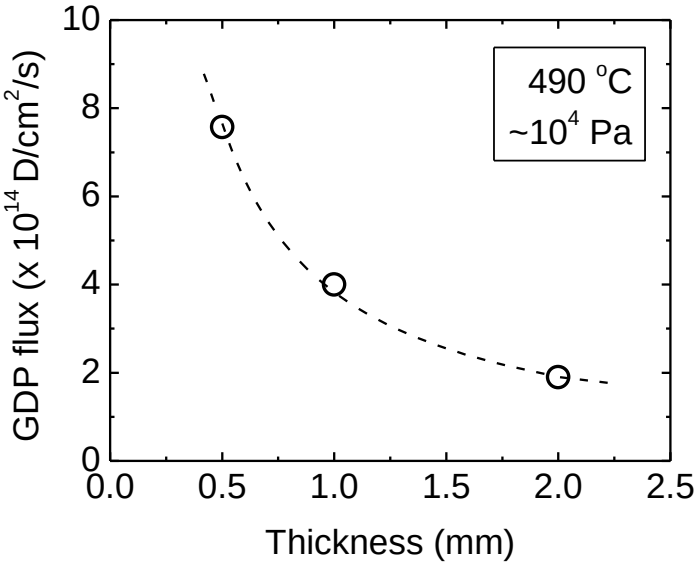

Figure 4.3 Thickness dependence of deuterium GDP flux through F82H membranes at 490 ℃ with upstream gas pressure of ~10^4 Pa.

According to Fick's law, the steady-state hydrogen diffusion-limited GDP flux J_∞ (atoms cm^{-2} s^{-1}) is given by Eq. (2.16), assuming downstream pressure $P_{\text{down}} = 0$:

$$J_\infty = \frac{\Phi\sqrt{P_{\text{up}}}}{L} = \frac{DS\sqrt{P_{\text{up}}}}{L}, \tag{4.1}$$

where D (cm^2 s^{-1}) is the diffusivity, S (mol cm^{-3} Pa$^{-0.5}$) is the Sieverts' constant or solubility, Φ (mol cm^{-1} s^{-1} Pa$^{-0.5}$) is the permeability and $\Phi = DS$. P_{up} (Pa) is the upstream gas pressure and L (cm) is the membrane thickness. All the experimental data agree with the theoretical prediction of Eq. (4.1), indicating that hydrogen isotopes GDP through F82H under the experimental conditions is diffusion-limited.

4.2.2 Isotopic effects

The measurements of steady-state GDP fluxes enable the evaluation of permeability. Shown in figure 4.4 is the evaluated hydrogen permeability for α-Fe from 200 ℃ to 500 ℃. In this temperature range, the hydrogen permeability Φ (mol cm^{-1} s^{-1} $Pa^{-0.5}$) can be expressed as:

$$\Phi_{(\mathrm{H})} = 5.3 \times 10^{-9} \exp\left(\frac{-0.47\ \mathrm{eV}}{k\mathrm{T}}\right), \tag{4.2}$$

where k is the Boltzmann's constant and T is the temperature (K). The experimental data are close to the literature data for α-Fe given by Forcey et al. [153] and Yamanishi et al. [154].

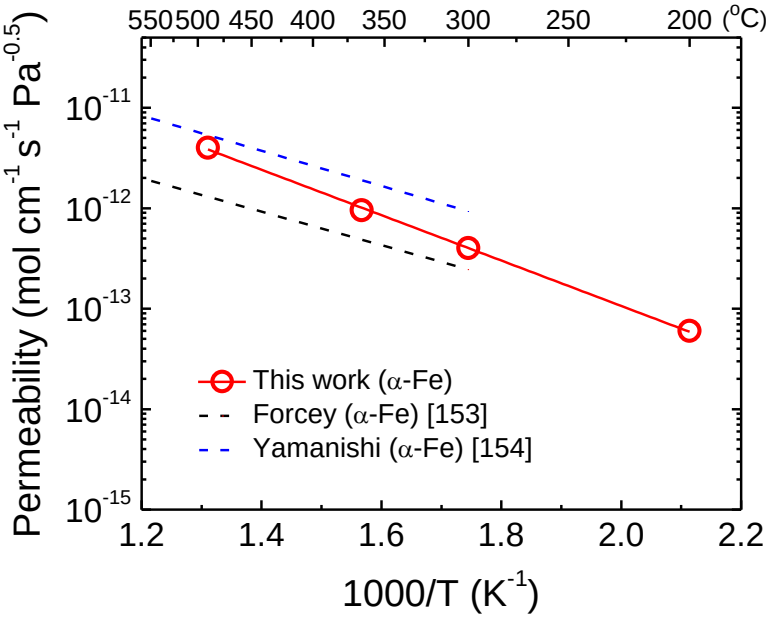

Figure 4.4 Measured hydrogen permeability for α-Fe. Forcey's [153] and Yamanishi's [154] data are shown for comparison.

Shown in figure 4.5 are the results of hydrogen and deuterium permeability for F82H from 150 ℃ to 500 ℃. Literature data [85-86, 88, 90] are also shown for comparison. The permeability Φ (mol cm^{-1} s^{-1} Pa$^{-0.5}$) from present experiments can be expressed as:

$$\Phi_{(\mathrm{H})} = 1.0 \times 10^{-9} \exp\left(\frac{-0.46\ \mathrm{eV}}{k\mathrm{T}}\right) \tag{4.3}$$

$$\Phi_{(\mathrm{D})} = 6.8 \times 10^{-10} \exp\left(\frac{-0.46\ \mathrm{eV}}{k\mathrm{T}}\right). \tag{4.4}$$

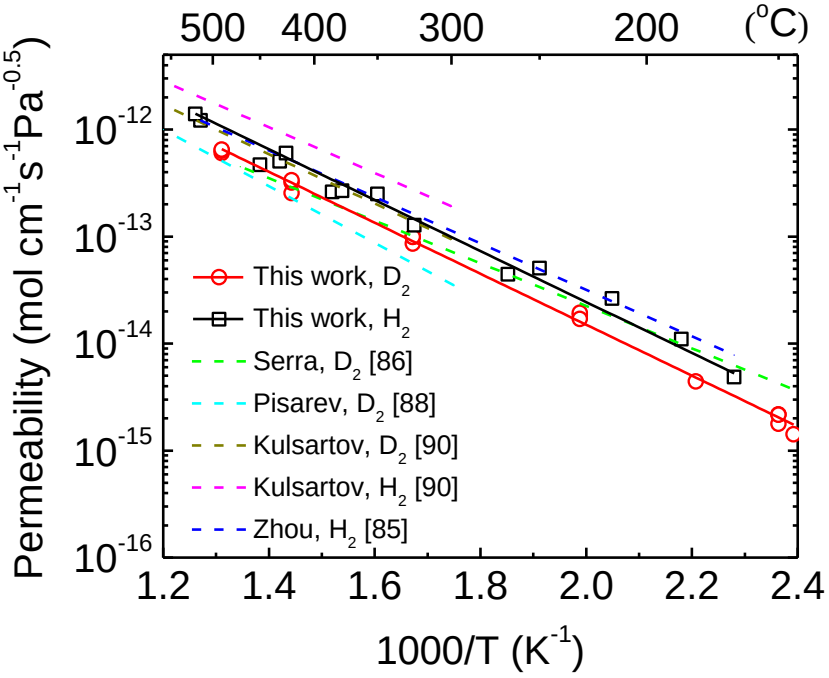

Figure 4.5 Measured permeability of hydrogen isotopes for F82H. Serra's [86], Pisarev's [88], Kulsartov's [90] and Zhou's [85] data are shown for comparison.

The hydrogen and deuterium "apparent" activation energies for permeation are virtually identical within experimental error, showing independence from isotopic mass, and agree well with those obtained by Kulsartov et al. [90] in the temperature range of 300-

600 ℃ at upstream hydrogen and deuterium pressures between 100 Pa and 1000 Pa. The ratio of the pre-exponential factor is calculated to be 1.47, consistent with the theoretical value of 1.41 predicted by the classical rate theory which relates diffusivity to atomic vibrational frequency and the frequency is inversely proportional to isotopic mass [155].

The isotopic mass effect has also been reported for stainless steel [156], iron [94] and Pd-Ag alloy [157]. For example, figure 4.6 shows the hydrogen isotopic mass effect on the permeability for type 310 austenitic stainless steel [156]. These permeability coefficients were measured at an upstream gas pressure of 4.4×10^4 Pa. One can find that the activation energies of hydrogen and deuterium for permeation in type 310 austenitic stainless steel are statistically independent of isotopic mass over the temperature range of 200 ℃ to 500 ℃. The average ratio of the pre-exponential factor is calculated to be ~1.44, which is consistent with classical behavior.

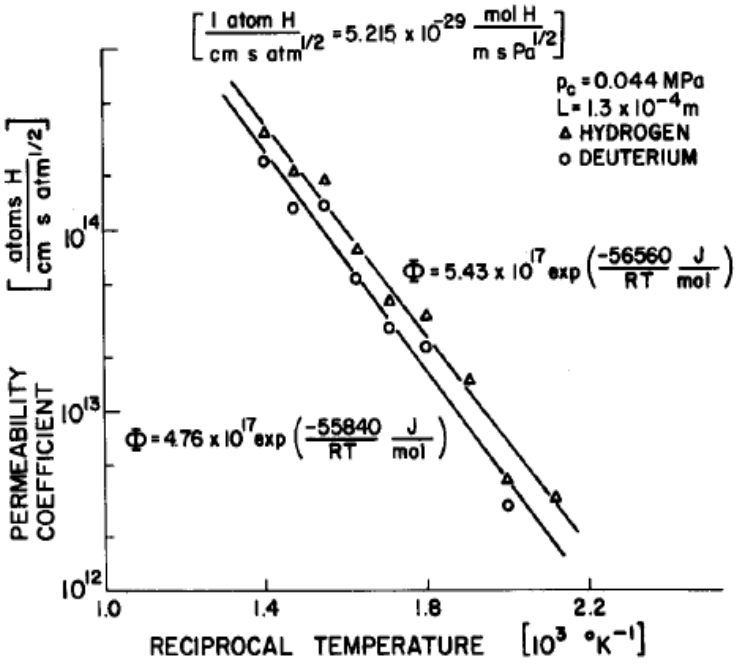

Figure 4.6 Hydrogen isotopic mass effect on the permeability for type 310 austenitic stainless steel [156].

As has been introduced in Section 2.2 of Chapter 2. There are three methods to evaluate the diffusivity D: 1) from the transient permeation behavior by fitting the transient permeation flux data, 2) by the so-called time-lag method $t_l = L^2/6D$ [120], or 3) by measuring the breakthrough time $t_b \approx L^2/15.3D$ [121]. Shown in figure 4.7 is the evaluated hydrogen permeability for α-Fe from 200 ℃ to 500 ℃. Literature data [154, 158] are shown for comparison. The diffusivity D ($cm^2\ s^{-1}$) has been measured to be:

$$D_{(\mathrm{H})} = 5.7 \times 10^{-4} \exp\left(\frac{-0.10\ \mathrm{eV}}{k\mathrm{T}}\right), \tag{4.5}$$

which is close to published data given by Yamanishi et al. [154].

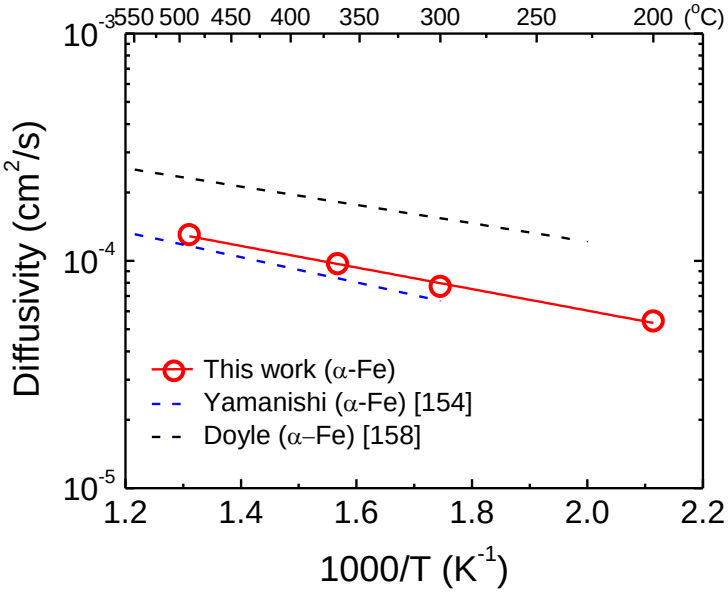

Figure 4.7 Measured hydrogen diffusivity for α-Fe. Yamanishi's [154] and Doyle's [158] data are shown for comparison.

The hydrogen solubility (or Sieverts' constant) S (mol cm^{-3} Pa$^{-0.5}$) for α-Fe can be obtained from $S = \Phi/D$ as:

$$S_{(\mathrm{H})} = 9.3 \times 10^{-6} \exp\left(\frac{-0.37\ \mathrm{eV}}{k\mathrm{T}}\right). \tag{4.6}$$

Shown in figure 4.8 is the measured hydrogen solubility for α-Fe from the present work. The experimental data are in a good agreement with literature data by Penalva et al. [159].

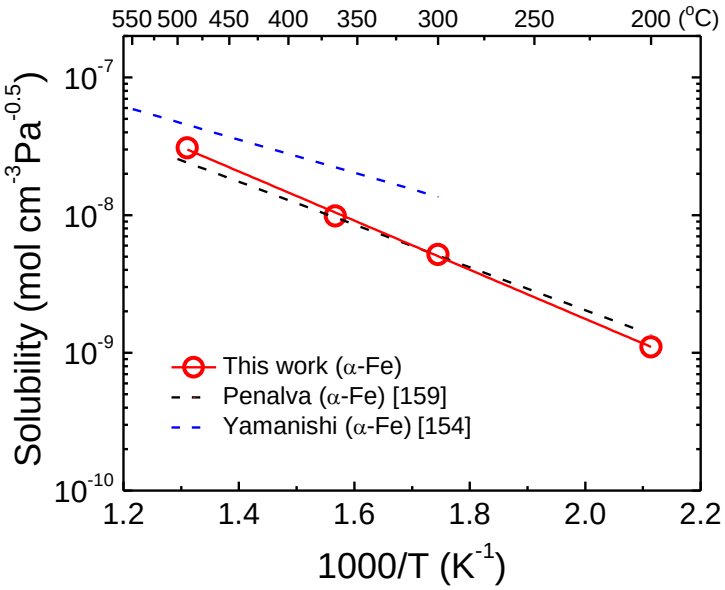

Figure 4.8 Measured hydrogen solubility for α-Fe. Penalva's [159] and Yamanishi's [154] data are shown for comparison.

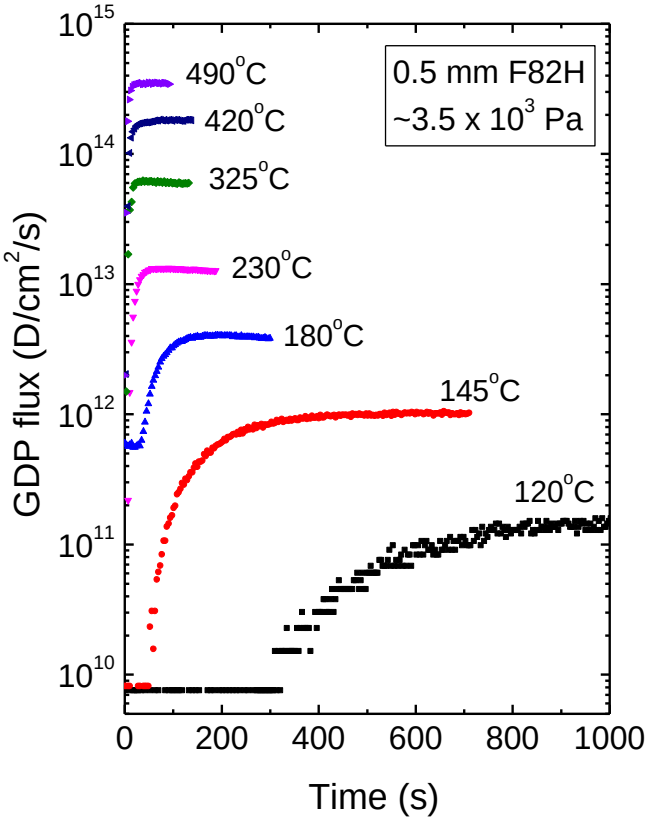

Figure 4.9 Deuterium GDP breakthrough curves through a 0.5 mm thick F82H membrane at various temperatures.

Shown in figure 4.9 are the deuterium GDP breakthrough curves through a 0.5 mm thick F82H membrane at various temperatures. The upstream deuterium pressure is set as ~3.5 × 10^3 Pa. The steady-state GDP flux increases with increasing temperature. Hydrogen and deuterium diffusivity for F82H has been evaluated from the GDP data, as shown in figure 4.10.

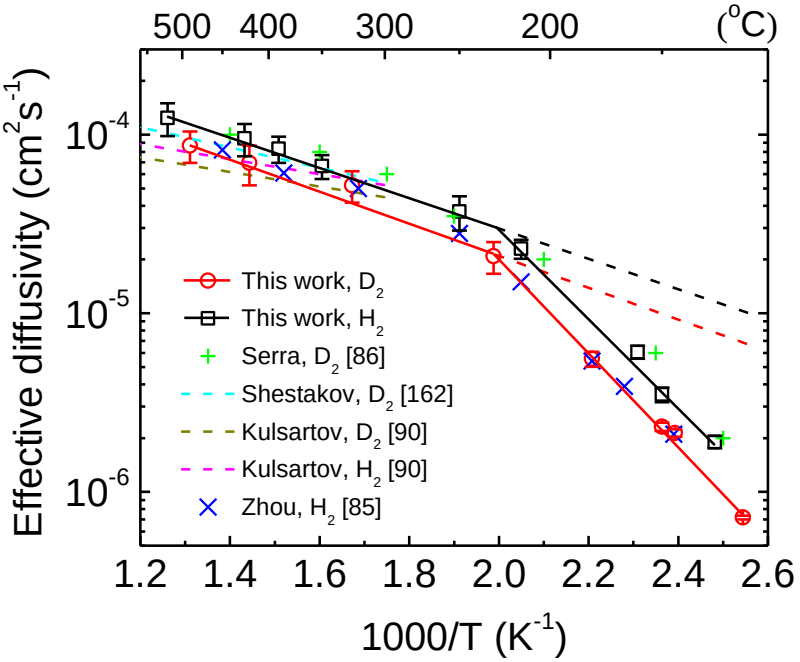

Figure 4.10 Measured diffusivity of hydrogen isotopes for F82H. Serra's [86], Shestakov's [162], Kulsartov's [90] and Zhou's [85] data are shown for comparison.

It is evident that the measured *D* for F82H, in the lower part of the present temperature range (120-250 ℃), drop sharply below the broken lines representing the data at higher temperatures (250-500 ℃). A breaking point around ~250 ℃ has also been reported in other works when measuring diffusivity for 7-10% Cr martensitic/ferritic steels [86, 160]. A possible explanation for the breaking point is the trapping effect [85]. At high temperatures, the trapping effect becomes negligible and the effective diffusivity is almost equal to the lattice diffusivity, but when the temperature decreases, the effective diffusivity starts to fall below the value of lattice diffusivity.

On the other hand, the values of permeability are described by Arrhenius straight lines in the present temperature range (figure 4.5). It arises from the fact that the values of permeability are evaluated from the steady-state permeation fluxes through the sample, i.e., when the trapped hydrogen population has reached equilibrium and, thus, does not affect

any further the flux through the sample. The contrasting behavior of the independently measured values of permeability and diffusivity provides remarkably convincing proof of the trapping effect to the present work.

The Arrhenius plots for the effective diffusivity of hydrogen and deuterium as calculated from time-lag data parallel each other, consistent with the permeability measurements. In fusion reactors, blankets are required to operate at elevated temperatures for efficient heat exchange [161]. The diffusivity D (cm^2 s^{-1}) at temperatures >250 ℃ is given by:

$$D_{(\mathrm{H})} = 9.9 \times 10^{-4} \exp\left(\frac{-0.14\ \mathrm{eV}}{k\mathrm{T}}\right) \tag{4.7}$$

$$D_{(\mathrm{D})} = 7.2 \times 10^{-4} \exp\left(\frac{-0.14\ \mathrm{eV}}{k\mathrm{T}}\right). \tag{4.8}$$

As shown in Eq. (2.26) of Chapter 2 that the ratio of diffusivity of hydrogen isotopes is equal to the inverse ratio of the square root of the mass [114]:

$$\frac{D_{(\mathrm{H})}}{D_{(\mathrm{D})}} = \sqrt{\frac{m_{(\mathrm{D})}}{m_{(\mathrm{H})}}}\ . \tag{4.9}$$

The activation energy for diffusion is assumed to be independent of the mass of the isotope, which is supported by our present experimental results, and the activation energy agrees well with some of the published values [85-86, 162]. The pre-exponential factor ratio of 1.38 is essentially identical to that obtained for permeability. This result indicates that the isotopic mass effect for diffusivity is consistent with classical behavior.

To allow a reference, the isotopic mass effect on hydrogen diffusivity for type 310 austenitic stainless steel is shown in figure 4.11 [156].

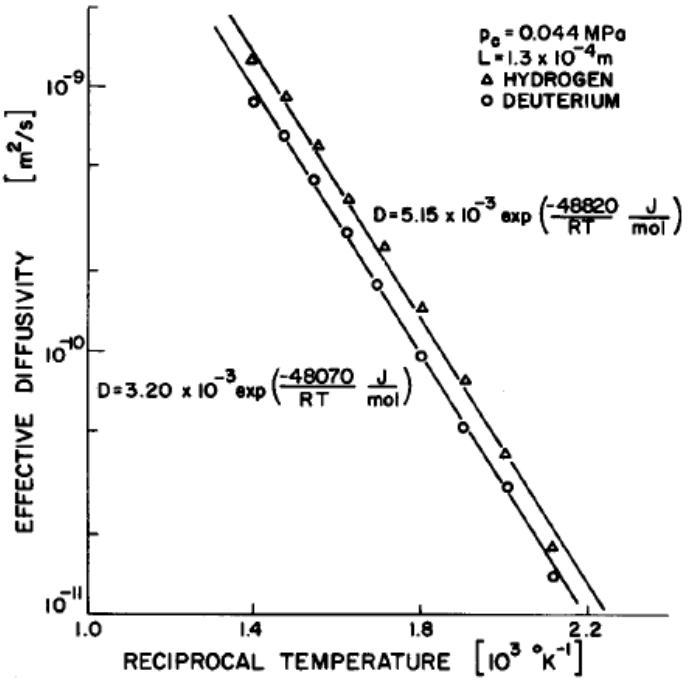

Figure 4.11 Hydrogen isotopic mass effect on the diffusivity for type 310 austenitic stainless steel [156].

As anticipated, the solubility for hydrogen and deuterium in F82H as calculated from the expression $\Phi = DS$ are identical within experimental error, exhibiting no isotopic effect. Shown in figure 4.12 are the solubility S (mol cm^{-3} Pa$^{-0.5}$) data from this work:

$$S_{(\mathrm{H})} = 1.0 \times 10^{-6} \exp\left(\frac{-0.32\ \mathrm{eV}}{k\mathrm{T}}\right) \tag{4.10}$$

$$S_{(\mathrm{D})} = 9.4 \times 10^{-7} \exp\left(\frac{-0.32\ \mathrm{eV}}{k\mathrm{T}}\right). \tag{4.11}$$

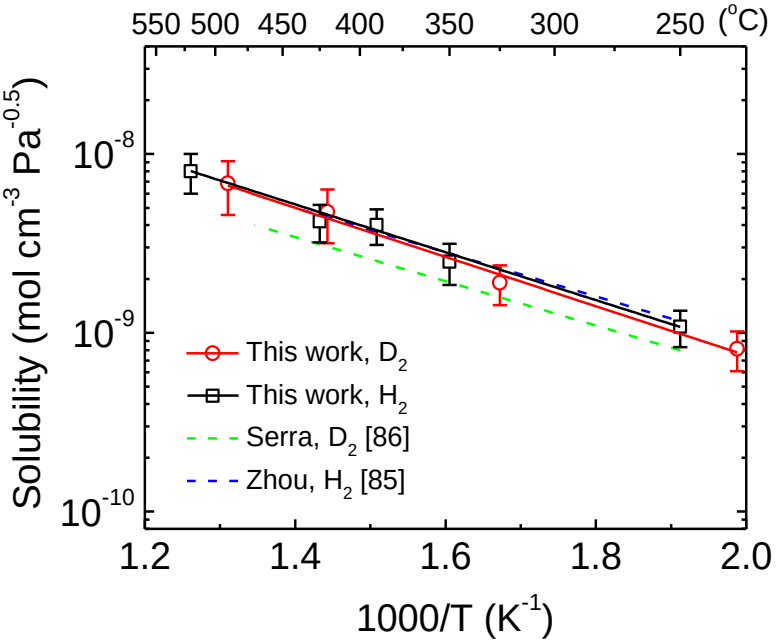

Figure 4.12 Measured solubility of hydrogen isotopes for F82H. Serra's [86] and Zhou's [85] data are shown for comparison.

4.3 Plasma-driven permeation

4.3.1 PDP in the RD-regime

Figure 4.13 shows the deuterium PDP flux through a 0.5 mm thick F82H membrane with a polished surface at the temperature of ~500 ℃. The plasma is produced with a deuterium gas pressure of ~0.1 Pa. The ECR power and DC bias are set at 350 W and -100 V, respectively. Under such discharge conditions, the electron temperature and density are measured by the Langmuir probe to be ~5 eV and 1×10^{10} cm^{-3}, respectively. Using Eq. (3.7), the net implantation flux J_0 has been estimated to be ~1.1×10^{16} $D/cm^2/s$. At ~500 ℃, the steady-state permeation flux has been found to be ~4.7×10^{12} $D/cm^2/s$.

A permeation spike has been observed for F82H in this experiment appeared in the time sequence of the plasma-driven permeation flux such that firstly the permeation flux increases to show a peak and then followed by a significant decrease to reach the steady-state permeation. The cause is attributed to the reduction of deuterium concentration in the plasma implanted surface by re-emission enhancement [77, 163].

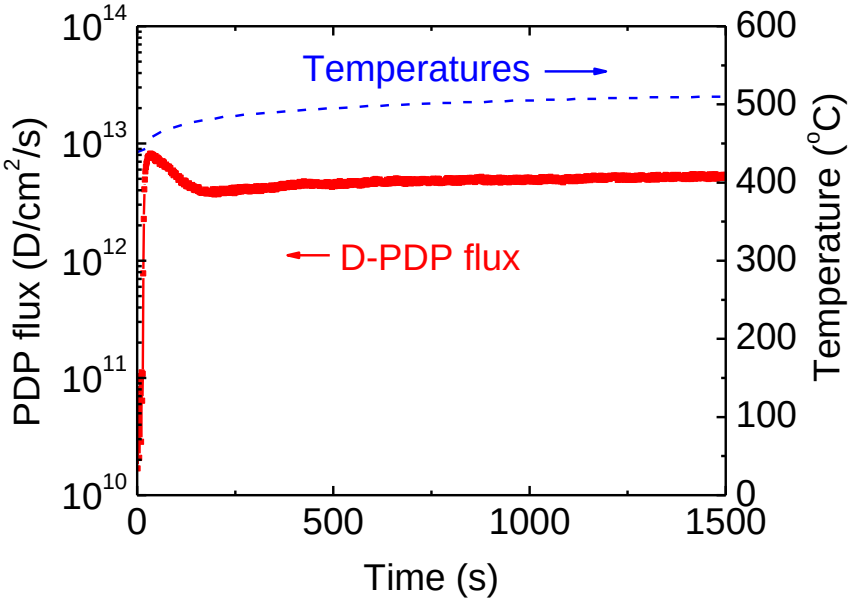

Figure 4.13 Deuterium PDP breakthrough curve through a 0.5 mm thick F82H membrane at ~500 ℃.

Shown in figure 4.14 are the steady-state deuterium PDP fluxes through 0.5 mm, 1 mm and 2 mm thick F82H membranes at temperatures of 445 ℃ and 510 ℃. The steady-state PDP fluxes through F82H are inversely proportional to the membrane thickness at all the examined temperatures. Recombination-limited release may be assumed for the upstream surface in this study because the implantation depth is only several nm at a bias of -100 V (see figure 2.3 of Chapter 2) and the possibility of DD-limited regime can be excluded as well by the measured permeation flux ratios. That means that hydrogen plasma-driven permeation through F82H in the present study is in the recombination-diffusion limited regime (RD-regime).

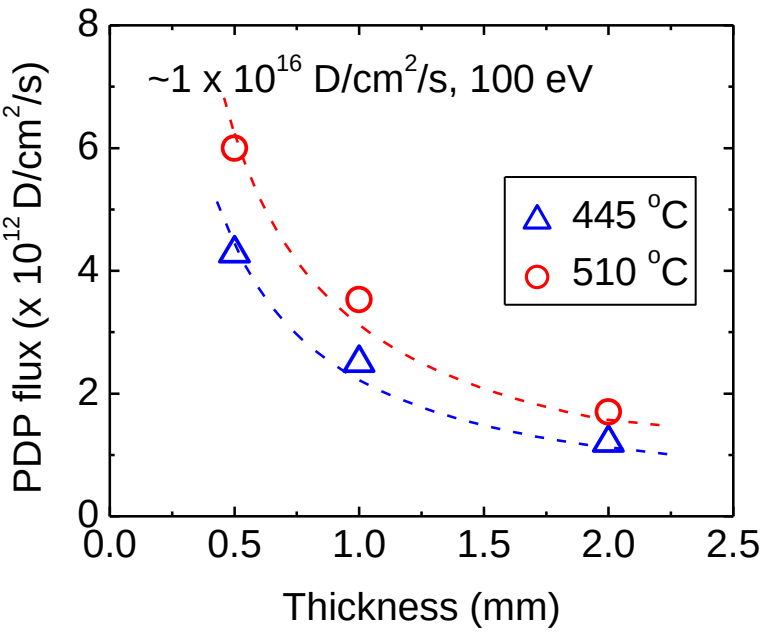

Figure 4.14 Thickness dependence of steady-state deuterium PDP fluxes through F82H membranes at temperatures of 445 ℃ and 510 ℃.

4.3.2 Surface recombination coefficient

Deuterium PDP fluxes through F82H membranes have also been measured as a function of temperature. Shown in figure 4.15 is the temperature dependence of PDP flux through 0.5 mm and 1 mm thick F82H membranes. It indicates that the PDP flux increases with increasing the membrane temperature and the PDP fluxes through the 0.5 mm thick F82H is about a factor of 2~3 higher than that through the 1 mm thick F82H in the temperature range of 250-550 ℃.

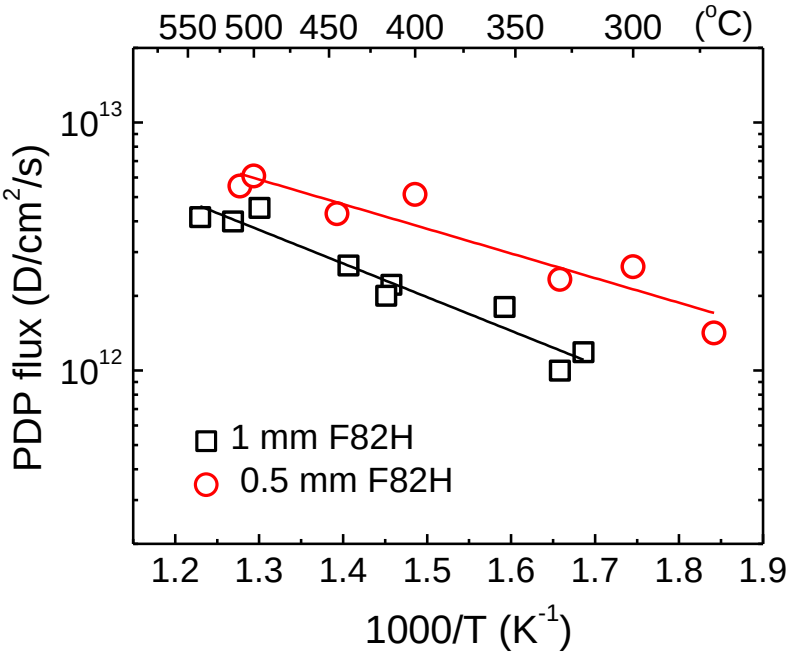

Figure 4.15 Temperature effect on steady-state deuterium PDP fluxes through F82H membranes.

As introduced in Section 2.3 of Chapter 2, for hydrogen PDP taking place in the RD-regime, the steady-state permeation flux J_+ (atoms cm^{-2} s^{-1}) is inversely proportional to the square root of the upstream surface recombination coefficient K_r (cm^4 s^{-1}):

$$J_+ = \frac{D}{L}\sqrt{\frac{J_0}{K_r}}\ , \tag{4.12}$$

where D (cm^2 s^{-1}) is the hydrogen diffusivity, L (cm) is the membrane thickness and J_0 (atoms cm^{-2} s^{-1}) is the net implantation flux. Using the evaluated data on D, K_r can be obtained from the measured data on J_0 and J_+.

To validate the experimental method, evaluation of K_r for α-Fe has been performed and compared with some of the literature data. Shown in figure 4.16 are the K_r ($cm^4\ s^{-1}$) data taken for α-Fe, which can be expressed as follows:

$$K_r = 1.2 \times 10^{-17} \exp\left(\frac{0.41\ \text{eV}}{k\text{T}}\right). \tag{4.13}$$

The experimental error mainly comes from the measurement of the net implantation flux J_0. The experimental results are in good agreement with the literature data measured by Nagasaki et al. [164], which means the method used in this work is valid for the evaluation of other first wall candidate materials.

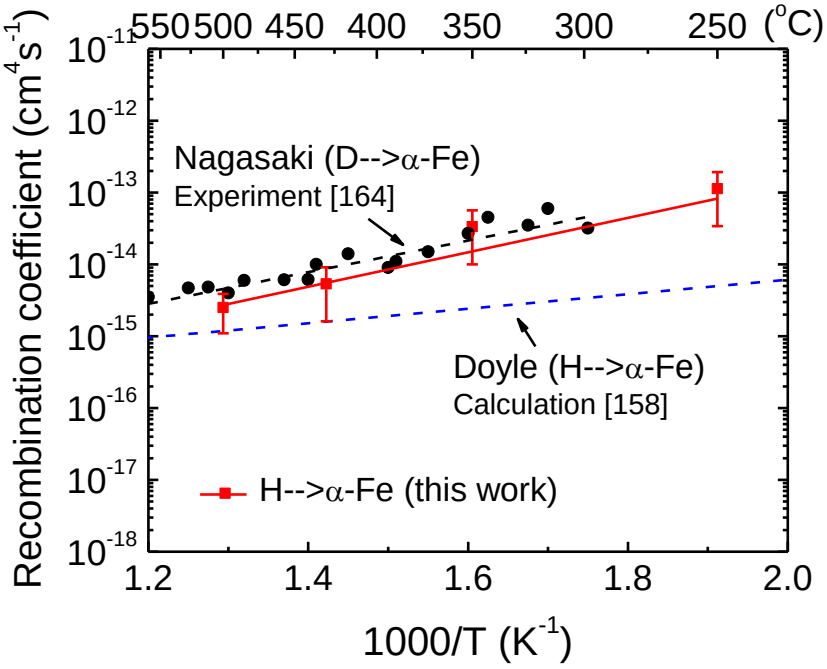

Figure 4.16 Measured hydrogen recombination coefficient for α-Fe. Nagasaki's [164] and Doyle's [158] data are shown for comparison.

Then the same evaluation method has been applied to F82H. Shown in figure 4.17 is the evaluated K_r (cm^4 s^{-1}) of deuterium for F82H from the present work which is given by:

$$K_r = 3.8 \times 10^{-17} \exp\left(\frac{0.20\ \text{eV}}{k\text{T}}\right). \tag{4.14}$$

To allow a comparison, literature data [85, 158, 164] are also shown in figure 4.17. The evaluated K_r of hydrogen for F82H is consistent with our previous study [85]. The evaluated K_r of deuterium for F82H is in good agreement with the reported data in Ref. [158] in both magnitude and temperature dependence.

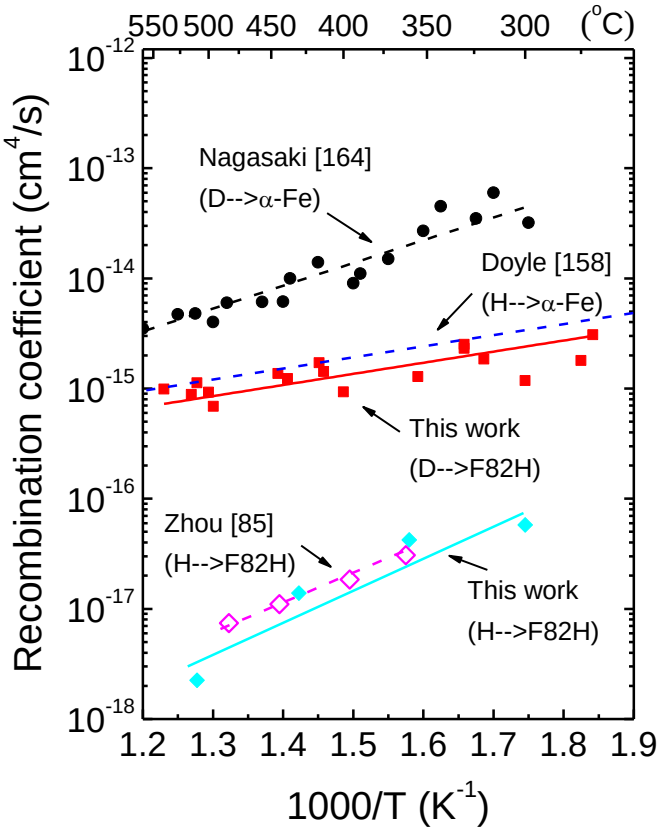

Figure 4.17 Measured hydrogen and deuterium recombination coefficients for F82H. Zhou's [85], Nagasaki's [164] and Doyle's [158] data are shown for comparison.

4.3.3 Discussion

The recombination coefficient is extremely sensitive to the surface conditions, such as surface morphology and contamination [165] etc. It has been indicated by some of the experimental results for stainless steel and nickel [68]. Myers et al. [166] measured the deuterium recombination coefficient for 304 stainless steel with and without in-situ sputtering of the surface oxide (as shown in figure 4.18). In this experiment, the rate of deuterium release at the surface was determined in the temperature range of 425-575 K for two kinds of surface, one oxidized by electro-polishing and air exposure, the other sputtered with Fe ions. It was found that the deuterium recombination coefficient for the ion-sputtered surface was a factor of 100 greater than the oxidized surface. These results are consistent with the theory that a decrease in permeation rate due to energetic ion bombardment is caused by the removal from the upstream surface of contamination which, when present, has an inhibiting effect on molecular recombination [77].

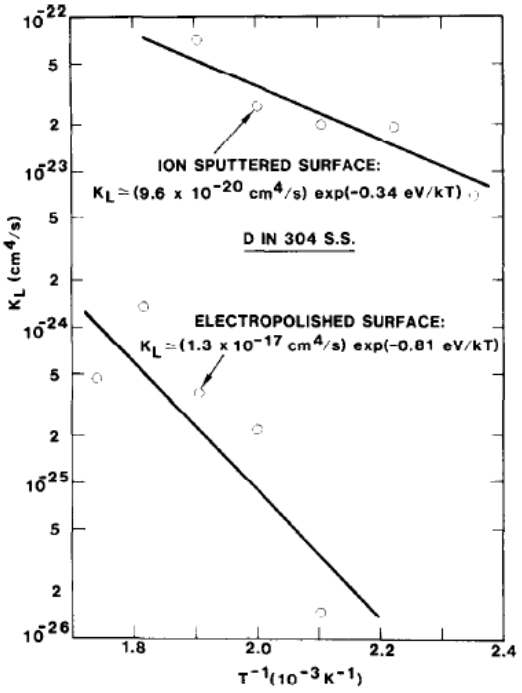

Figure 4.18 Recombination coefficient of deuterium on 304 stainless steel with and without prior sputtering of surface oxide [166].

Ogorodnikova [167] investigated the effects of surface impurities on plasma-driven tritium permeation through metals. Figure 4.19 shows the tritium permeation probability as a function of the sticking coefficient on the plasma-facing surface. It has been found the removal of impurities on the plasma-facing surface, namely the increasing of the sticking coefficient, significantly decreases tritium permeation through most of endothermic metals. The increase of impurities on the plasma-facing surface, namely the reduction of the front sticking coefficient, drastically increases hydrogen isotopes permeation.

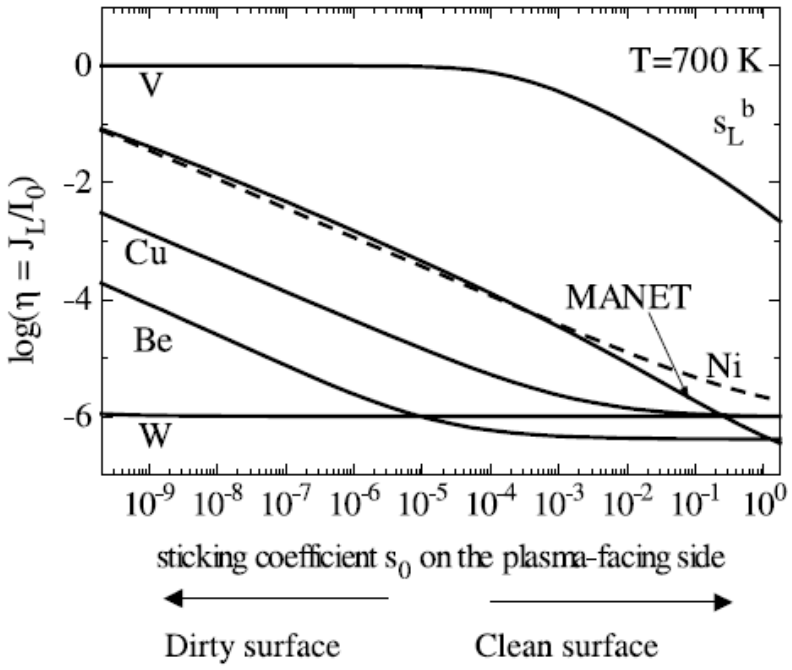

Figure 4.19 Calculated tritium permeation probability as a function of the sticking coefficient on the plasma-facing surface [167].

Physically, the explanation of the increase of the steady-state permeation with the reduction of the sticking coefficient on the front surface, is quite clear. Impurities on the plasma-facing surface act as a barrier against the hydrogen isotopes re-emission. The

reduction of sticking coefficient results in the reduction of the re-emission flux. In the steady-state the sum of the re-emission (J_-) and the permeation (J_+) fluxes is constant:

$$J_0 = J_- + J_+. \tag{4.15}$$

If the re-emission flux decreases, the permeation flux increases.

If the energy of the incident particles is below 50 eV, the much sputtering of impurities from the plasma-facing surface is not expected. If the energy of the incident particles striking the first wall is high enough to remove surface impurities, it is expected that the surface will be sputter-cleaned during the plasma operation [168]. Removal of the impurities on the front surface of the metal increases the front sticking coefficient. The creation of surface roughness and damages have additional effects on the increase of the sticking factor [165]. Consequently, the plasma-facing surface will depend upon the whole set of physical and physicochemical conditions existing in each particular fusion device.

In this study, the membrane is polished and analyzed by energy dispersive X-ray spectroscopy to make sure no major impurities are left on the surface. Prior to hydrogen isotopes PDP experiments, argon plasma bombardment is conducted for 10 minutes at -50 V to remove surface contamination from air exposure. Having surface conditioning done, K_r is assumed to be evaluated from a relatively "clean" surface. Probably resulted from the different sputtering yield effects of hydrogen isotopes, K_r of hydrogen and deuterium for F82H span a range of about two orders of magnitude [77]. Nevertheless, further investigations are still needed to address this issue.

4.4 Bi-directional H/D permeation

Hydrogen isotopes gas-driven permeation and plasma-driven permeation experiments have been presented separately in Section 4.2 and Section 4.3. For the hydrogen isotopes permeation through the first wall, a fundamental materials science question that needs to be addressed is: can gas- and plasma-driven permeation of hydrogen isotopes in the two counter directions actually take place simultaneously under fusion reactor relevant conditions? Experiments studies have been done to answer the question. In this section, the data taken from the first-of-a-kind bi-directional deuterium PDP and hydrogen GDP experiments are presented.

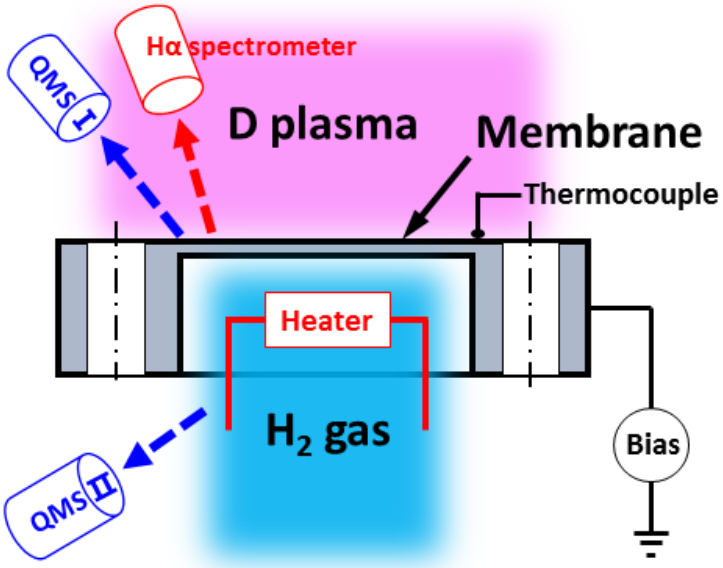

Figure 4.20 A schematic diagram of the bi-directional H/D permeation setup in VEHICLE-1.

Shown in figure 4.20 is a schematic diagram of the bi-directional permeation setup in VEHICLE-1. The F82H membrane is fixed in such a way that the upstream surface is exposed to deuterium plasma, while the other side is exposed to hydrogen gas. The sample

membrane is heated up to ~500 ℃ by a resistive heater. At the plasma-facing side, the hydrogen GDP flux can be detected by a quadrupole mass spectrometer (QMS) through a 1 mm diameter orifice. The H_α signal is monitored by an optical spectrometer. The electron temperature is raised up to ~10 eV for the improved sensitivity of H_α spectroscopy. Under such experimental conditions, if the recycling condition of the membrane surface changes, variation in H_α intensity and hydrogen partial pressure are expected to be detected. At the gas side, since it is difficult to measure the real-time deuterium PDP flux due to the high background pressure that the variable leak valve is closed for ~2 h to accumulate the permeated deuterium in the closed volume. The evidence of deuterium PDP into hydrogen gas can be determined by the increase of D_2 and HD partial pressures.

4.4.1 Hydrogen GDP into deuterium plasma

Shown in figure 4.21 is the evidence of GDP hydrogen flows into the deuterium plasma. In this case, the thickness of F82H membrane is 0.5 mm and the membrane temperature is ~500 ℃. The deuterium plasma bombarding energy is set at -100 V. Taking into account the ion species mix in the low temperature deuterium plasma and the particle reflection at the plasma-facing surface, the net implantation flux is estimated to be ~8.3×10^{15} D/cm^2/s.

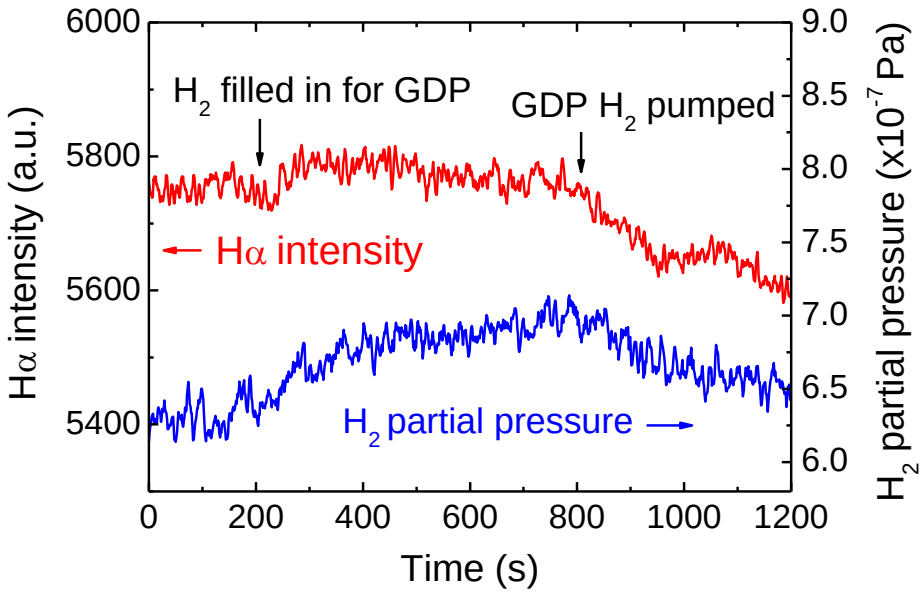

Figure 4.21 Measured H_α signal and hydrogen partial pressure at the plasma-facing side. The thickness of F82H membrane is 0.5 mm. The membrane temperature is ~500 ℃.

Recognize that the hydrogen partial pressure and H_α spectroscopy nicely keep track of each other in the duration period from the initial hydrogen gas fill-in to the gas pump-out at the downstream side. The membrane is first exposed to deuterium plasma, in which case only deuterium PDP takes place. Then hydrogen gas is introduced from a gas cylinder into the closed volume to a pressure of ~10^4 Pa. After the H_α signal reaches steady-state, the hydrogen gas is then pumped out. Langmuir probe measurements are performed before and after introducing hydrogen gas into the GDP volume. The plasma density is found to increase from ~4×10^9 cm^{-3} to ~6×10^9 cm^{-3}, while the electron temperature decreases from 10.7 eV to 8.5 eV. These data indicate that GDP hydrogen flows into deuterium plasma and results in an increase in the first wall recycling. The GDP hydrogen flow rate has been evaluated to be about ~6.4×10^{14} $H/cm^2/s$.

4.4.2 Deuterium PDP into hydrogen gas

Notice that, while GDP hydrogen flows into deuterium plasma, PDP deuterium flows into hydrogen gas as well. The experimental conditions are essentially the same with that described in the previous section except that the hydrogen gas pressure is reduced to ~1.4 × 10^3 Pa in this experiment to obtain relatively high D_2 and HD signals. As shown in figure 4.22, both the D_2 and HD partial pressures increase after deuterium PDP pressure build-up of ~2 h, indicating that PDP deuterium flows into hydrogen gas in the counter direction of GDP hydrogen. The PDP deuterium flow rate in this case has been evaluated to be ~5.6 × 10^{12} D/cm^2/s.

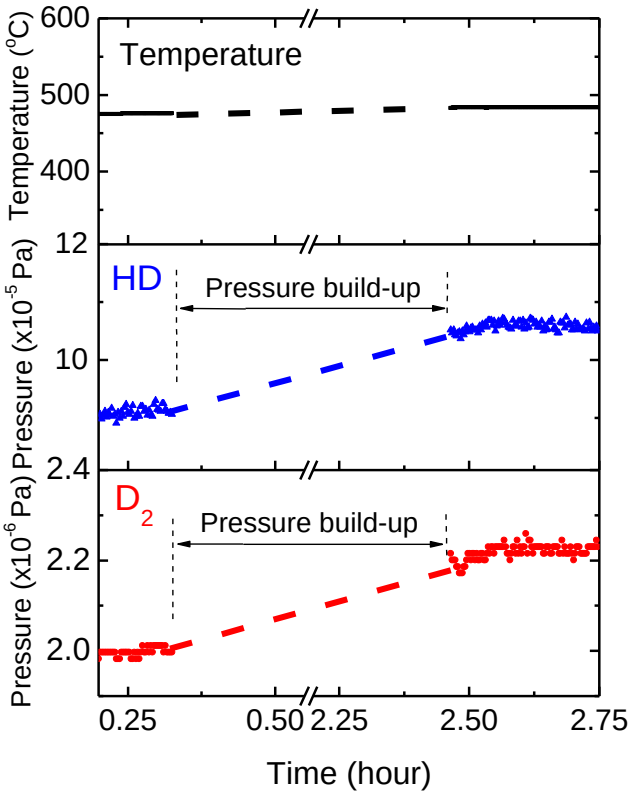

Figure 4.22 D_2 and HD partial pressures detected at the gas side. The F82H membrane thickness is 0.5 mm.

4.5 Summary

Gas- and plasma-driven permeation through a reduced activation steel alloy F82H has been investigated using a steady-state laboratory-scale plasma device: VEHICLE-1. The hydrogen transport parameters data taken for α-Fe have been found to be in good agreement with the literature data, which means that the experimental setup in VEHICLE-1 is valid for the evaluation of other first wall candidate materials.

Both GDP and PDP data taken for F82H show thickness dependence, suggesting that hydrogen isotopes permeation through F82H is diffusion-limited. The hydrogen and deuterium transport parameters such as permeability, diffusivity, solubility and surface recombination coefficient have been successfully measured for F82H. In particular, the surface recombination coefficient of deuterium on F82H, which is essential to correctly predict the hydrogen isotopes permeation flux through the first wall, has been experimentally measured for the first time. Isotopic effects on hydrogen transport have been discussed. The permeability and diffusivity data show isotopic mass effect which is predicted by the classical rate theory relating hydrogen diffusion to the atomic jumping frequency, the solubility, however, exhibits no isotopic mass effect.

Simultaneous bi-directional H/D permeation has been demonstrated experimentally for the first time under controlled experimental conditions. Hydrogen GDP has been found to take place in the opposite direction of deuterium PDP. The hydrogen GDP flux into deuterium plasma has been found to be about two orders of magnitude higher than that of deuterium PDP when the gas driving pressure is high (~10^4 Pa). It suggests that for blankets employing those breeders with high tritium equilibrium pressures, GDP may dominate the overall hydrogen transport process and increase in first wall recycling. In this case, one would expect to apply surface coatings to reduce both the GDP and PDP fluxes through the first wall. Further investigations of the coatings effects on hydrogen isotopes permeation have been done and the results are presented in Chapter 5 and Chapter 6.

Chapter 5

Hydrogen isotopes gas- and plasma-driven permeation through vacuum plasma-sprayed tungsten coated F82H

In the previous chapter, hydrogen isotopes GDP and PDP data through bare F82H have been presented. For a DEMO reactor, having a first wall area of several thousand square meters, one would expect that the uncontrollable gas fueling rate to be of the order of 100 Pa m^3/s at 500 ℃ [169], which is undesirable from the viewpoint of achieving high confinement via plasma-wall boundary control. Therefore, there is a need for surface coatings as a hydrogen permeation barrier. Tungsten (W) has been proposed as a candidate plasma-facing material for the divertor of the International Thermonuclear Experimental Reactor (ITER) because of its beneficial properties such as high melting point, high thermal conductivity and low sputtering yield [170]. For a DEMO reactor, surface coatings made of W are necessary to protect the plasma-facing wall made of reduced activation ferritic steels such as F82H. In this chapter, the plasma-sprayed tungsten (VPS-W) coatings are prepared on the F82H substrate and the effects of VPS-W coatings on hydrogen GDP and PDP are investigated.

5.1 Microstructural characterization of VPS-W

Figure 5.1 shows the surface and cross-section SEM images of the VPS-W coated F82H samples. It is shown that VPS-W coatings have an inhomogeneous microstructure, i.e., a mixture of disorganized areas composed of partially-melted W particles, splats with columnar solidification and void regions (or porosity) [98]. Voids or pores are observed primarily next to the unmelted W particles. The “as-fabricated” VPS-W surface is dull-colored and EDS (dispersive X-ray spectroscopy) analyses indicate surface impurity elemental composition is dominated by carbon. The average density of VPS-W coatings has been evaluated to be ~90% of bulk polycrystalline W.

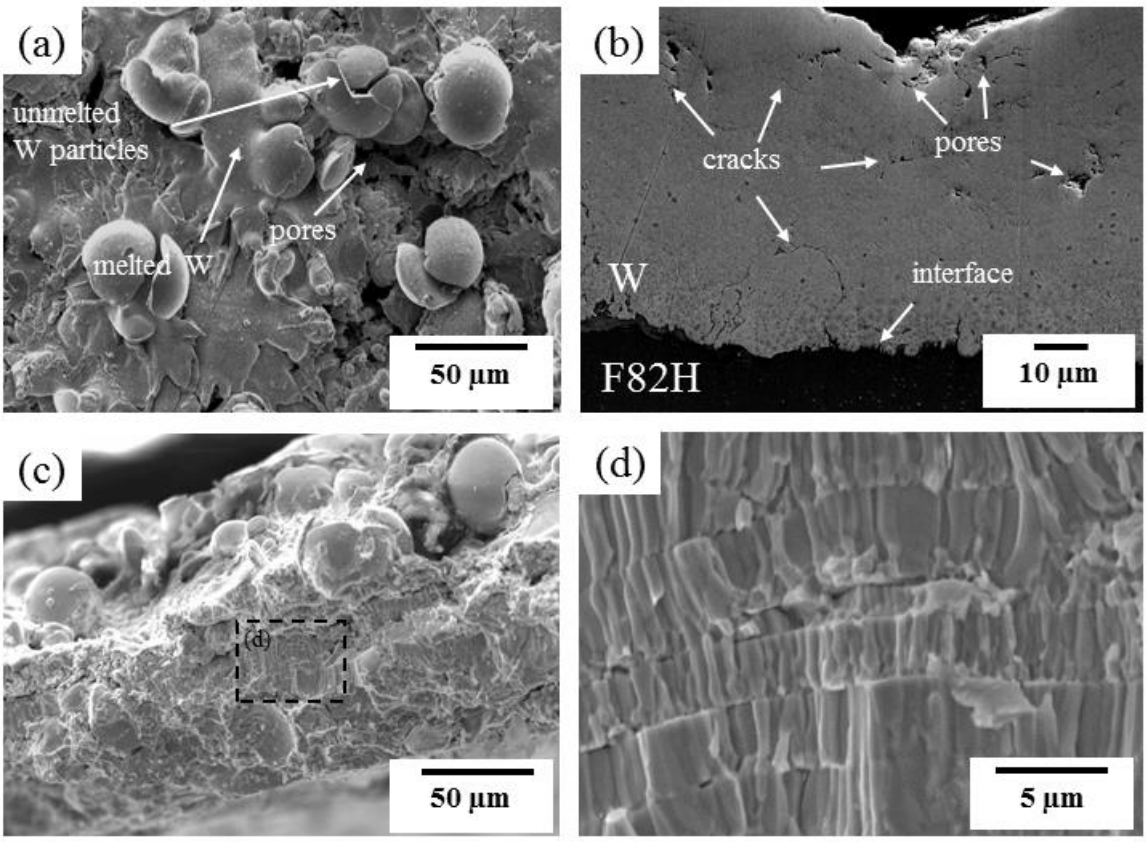

Figure 5.1 (a) VPS-W coatings surface (as-received), (b) polished and (c) fractural cross-section of VPS-W coatings and (d) lamellar structure of columnar tungsten grains.

5.2 Gas-driven permeation

5.2.1 Characteristics of GDP through VPS-W coated F82H

Shown in figure 5.2 are the steady-state hydrogen GDP fluxes through VPS-W coated F82H in the temperature range of 200-500 ℃. In this experiment, the VPS-W coatings side is the GDP upstream. A linear relationship between the GDP fluxes and the square-root of upstream gas pressure has been found, indicating that hydrogen GDP through the VPS-W coated F82H is diffusion-limited.

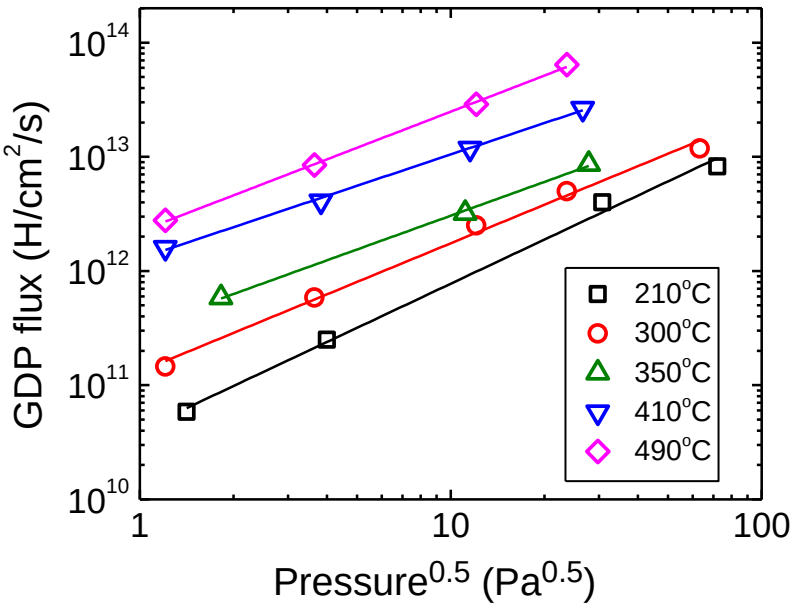

Figure 5.2 Steady-state hydrogen GDP fluxes through a VPS-W coated F82H membrane in the temperature range of 200 - 500 ℃. The thicknesses of VPS-W coatings and F82H substrate are 90 μm and 0.5 mm, respectively.

The effective hydrogen diffusivity D_{eff} for VPS-W coated F82H has been evaluated by the time-lag method (see Section 2.2 of Chapter 2) from 200℃ to 500 ℃, as shown in

figure 5.3. Literature data for F82H [85, 87] and bulk polycrystalline W [95] are shown for comparison. The D_{eff} ($cm^2\ s^{-1}$) from the present work can be expressed as:

$$D_{eff} = 7.9 \times 10^{-4} \exp\left(\frac{-0.20\ eV}{kT}\right). \quad (5.1)$$

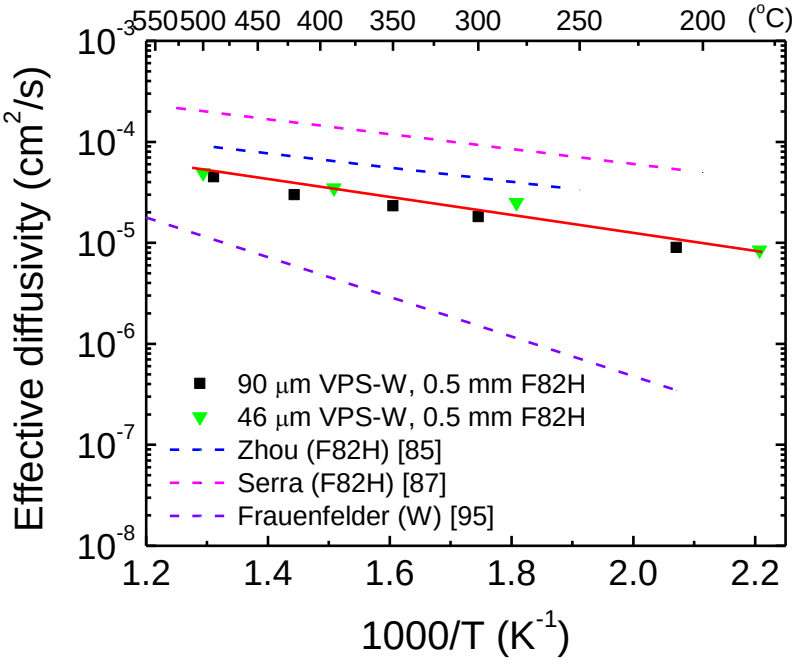

Figure 5.3 Evaluated effective hydrogen diffusivity for VPS-W coated F82H. Zhou's [85], Serra's [87] and Frauenfelder's [95] data are shown for comparison.

As reported by Golubeva et al. [171] that the mechanism of hydrogen permeation through VPS-W coatings is molecular hydrogen gas flow through the system of connected porosity. In this care, the effective surface area plays a key role determining the permeation flux. In order to investigate the effects of effective upstream surface area, hydrogen GDP in two opposite directions (i.e., VPS-W as GDP upstream or F82H as GDP upstream) has been carried out. Figure 5.4 shows the steady-state hydrogen GDP fluxes through the composite VPS-W/F82H sample in two opposite directions. A bare F82H membrane is

used for comparison. The upstream hydrogen pressure is set at ~10^4 Pa. It shows that the GDP fluxes with the VPS-W side on the upstream are reduced by ~93% compared with that of bare F82H. However, the GDP fluxes with the F82H side on the upstream are comparable with that of bare F82H.

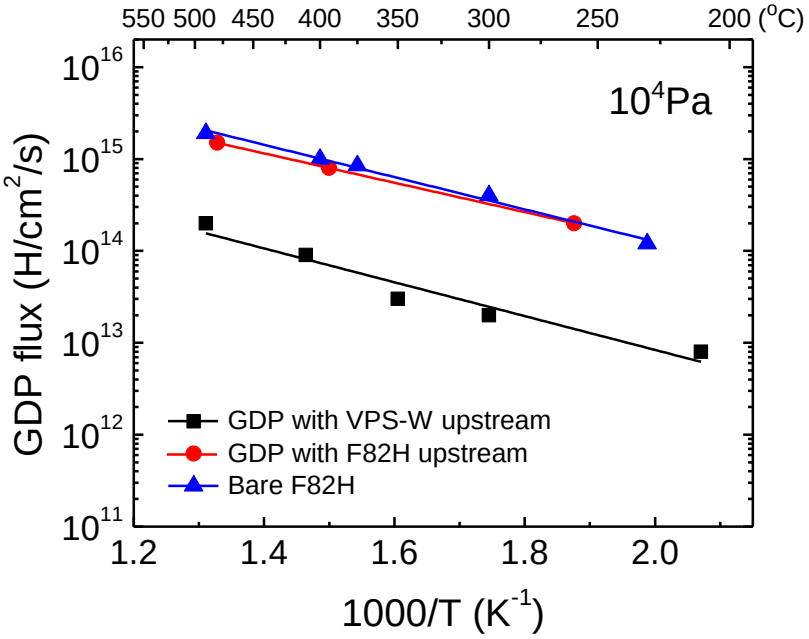

Figure 5.4 Steady-state hydrogen GDP fluxes through VPS-W coated F82H in two opposite directions. The upstream hydrogen pressure is set at ~10^4 Pa. The thicknesses of VPS-W coatings and F82H substrate are 90 μm and 0.5 mm, respectively. A 0.5 mm thick bare F82H membrane is used for comparison.

Figure 5.5 shows the steady-state hydrogen GDP fluxes through 1 mm F82H coated with VPS-W coatings of different thicknesses. In these experiments, the VPS-W coatings side is the GDP upstream. It indicates that the permeation fluxes for these two samples are comparable with each other even though the thickness of W coatings is different about a factor of two from each other.

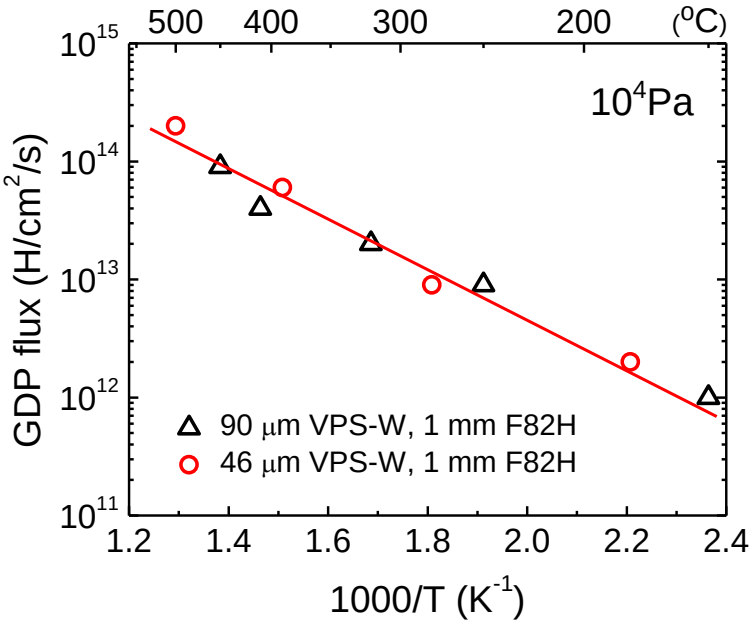

Figure 5.5 Steady-state hydrogen GDP fluxes through 1 mm F82H coated with VPS-W coatings of different thicknesses (VPS-W is the GDP upstream).

5.2.2 Discussion

Usually, hydrogen permeation through materials is affected by both bulk and surface processes. In this study, F82H steel surface is covered by a layer of VPS-W coatings. As it has been mentioned before, the typical VPS-W coatings consists of partially melted W particles, melted W and substantial surface-connected porosity [172]. Even a 200 μm thick layer of VPS-W has an open system of connected pores, which connects the front and rear surfaces of the deposited layer [171]. The density of the prepared VPS-W coating is ~90% of bulk W, which means the porosity is ~10%, including open (or connected) pores and closed pores. Thus, the results obtained in this study can be explained by molecular hydrogen permeation through open pores of VPS-W coatings combined with permeation in a dissociated form through F82H substrate. That means, the open pores allow hydrogen gas reach to the W/F82H interface. Consequently, hydrogen dissolves at the interface and

diffuses into the F82H substrate to allow hydrogen permeation after a certain period of time [66, 173].

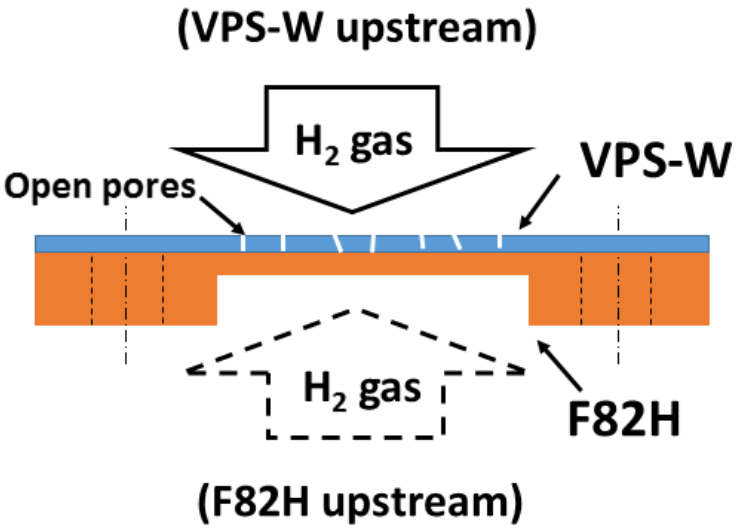

Figure 5.6 A schematic diagram of hydrogen GDP through porous VPS-W coated F82H in two opposite directions.

It is well known that the solubility of hydrogen in bulk polycrystalline W is quite low compared to, for example, steels [174]. Therefore, one might assume that the bulk of W is practically impermeable for hydrogen under the given conditions. An illustrative diagram of hydrogen GDP through porous VPS-W coated F82H in two opposite directions is shown in figure 5.6. The GDP fluxes with the F82H side on the upstream are almost same with that of bare F82H (figure 5.4), which is attributed to the equivalent upstream surface area. Because it has been introduced in Chapter 3 that hydrogen transport in the F82H is rate-limited by the diffusion process of hydrogen atoms, one might assume the hydrogen pressure at the W/F82H interface is almost zero (vacuum) in this case, i.e., hydrogen concentration at the interface is negligible. As a result, hydrogen GDP is not affected by the porous VPS-W coatings. But, the GDP fluxes with the VPS-W side on the upstream are ~7% compared to that of bare F82H, which means the effective surface area of the F82H steel is reduced to ~7% by the porous VPS-W. In other words, the density of open

pores is ~7% and ~93% of F82H steel surface is covered by W (including closed pores). The main effect of the VPS-W coatings on hydrogen permeation is to reduce the incoming flux at the W/F82H interface and the effective area for hydrogen dissolution in the substrate [104]. Therefore, the GDP fluxes through composite VPS-W/F82H membranes are almost independent of the W coating thickness, which is illustrated in figure 5.5.

Although the square-root dependence of GDP fluxes against driving pressure (figure 5.3) suggests the diffusion-limited permeation under the given conditions, the effective hydrogen diffusivity shown in figure 5.3 is smaller than the values reported for F82H [85, 87]. These observations indicate that the permeation in transient states could be affected by also other factors such as surface contamination.

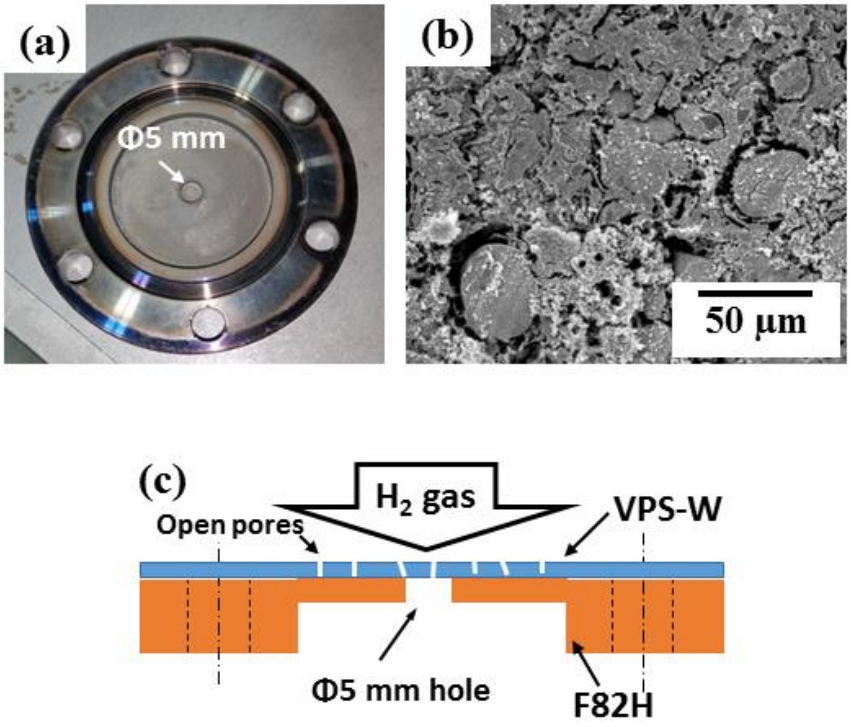

Figure 5.7 (a) a picture of the permeation sample which has been machined down to the W/F82H interface by removing F82H substrate, (b) a SEM image of the W/F82H interface and (c) a schematic diagram of hydrogen gas flows through the porous VPS-W coatings.

A more extensive study on the hydrogen permeation properties through porous VPS-W coatings has been conducted. Shown in figure 5.7(c) is a schematic diagram of hydrogen gas flows through the VPS-W coatings. In this experiment, the F82H substrate has been mechanically removed (figure 5.7(a)), leaving only the VPS-W coatings, the thickness of which is ~170 μm. A SEM image of the W/F82H interface is shown in figure 5.7(b).

The typical dependence of hydrogen permeation flux on pressure gradient over the membrane is presented in figure 5.8. This experiment is performed at room temperature. The hydrogen permeation flux is detected almost immediately after gas loading of the sample, and it increases proportional to the pressure gradient in the range of 0 - 50 Torr. It indicates that gas flux penetrates through the connected pores in the coatings but not through the W bulk.

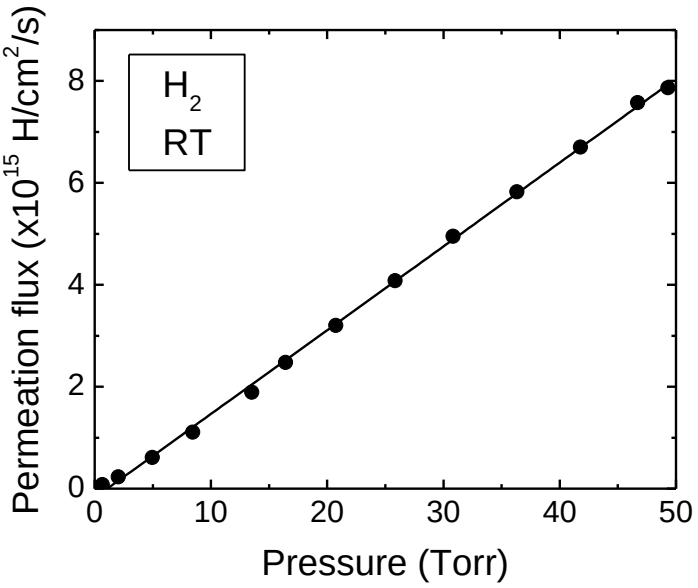

Figure 5.8 Hydrogen gas flows through the VPS-W coatings at room temperature.

5.3 Plasma-driven permeation

Figure 5.9 shows the hydrogen PDP breakthrough curve through a VPS-W coated F82H membrane with an as-deposited W surface at the temperature of ~500 ℃. The thicknesses of VPS-W coatings and F82H substrate are 90 μm and 0.5 mm, respectively. A 0.5 mm thick bare F82H membrane is used for comparison. In these experiments, the ECR power is set at 350 W and the DC bias is -100 V. The electron temperature and density are measured to be ~5 eV and 1.8×10^{10} cm^{-3}, respectively. Time zero in figure 5.9 corresponds to the plasma-on time. The steady-state hydrogen PDP flux has been measured to be ~4.5×10^{12} $H/cm^2/s$ for the VPS-W coated F82H at 500 ℃, which is more than one order of magnitude lower than that for bare F82H. Hydrogen permeation is observed shortly after the plasma-on time and the permeation flux continued to rise gradually until the implantation is terminated.

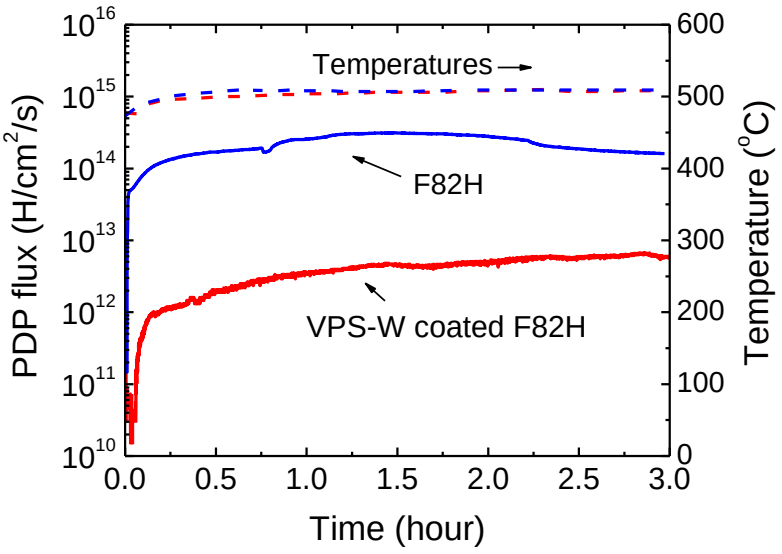

Figure 5.9 Hydrogen PDP breakthrough curves for VPS-W coated F82H and bare F82H membranes at ~500 ℃. The thicknesses of VPS-W coatings and F82H substrate are 90 μm and 0.5 mm, respectively. A 0.5 mm thick bare F82H membrane is used for comparison.

Hydrogen PDP fluxes through VPS-W coated F82H membrane have also been measured as a function of temperature. Shown in figure 5.10 are the temperature dependence of steady-state PDP fluxes for F82H with and without VPS-W coatings. It is shown that VPS-W coatings reduce hydrogen PDP fluxes by more than one order of magnitude relative to that of bare F82H in the temperature range from 250 ℃ to 550 ℃ and the PDP flux increases as temperature increasing. Reduced permeation fluxes are attributed to the complex microstructure and a substantial surface-connected porosity of VPS-W coatings [104, 172].

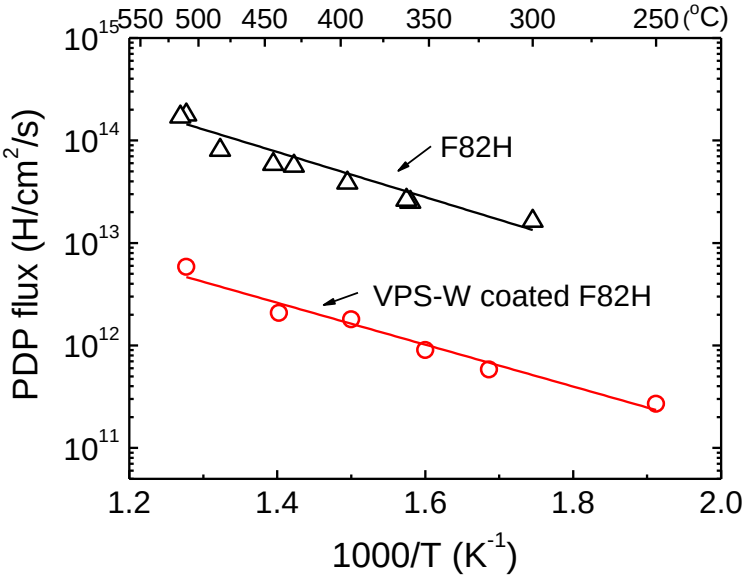

Figure 5.10 Temperature dependence of steady-state hydrogen PDP fluxes through F82H with and without VPS-W coatings. The thicknesses of VPS-W coatings and F82H substrate are 90 μm and 0.5 mm, respectively. The thickness of bare F82H membrane is 0.5 mm.

5.4 Summary

Hydrogen GDP and PDP experiments have been conducted for VPS-W coated F82H membranes. For the GDP experiments, it has been found that the permeation fluxes with the VPS-W side on the upstream are reduced compared to that of bare F82H. However, the permeation fluxes with the F82H side on the upstream are comparable with that of bare F82H. For PDP experiments, VPS-W coatings reduce hydrogen PDP fluxes in the examined temperature range. VPS-W coatings have been proved experimentally to have an open system of connected pores.

For a future fusion reactor, based on these data one predicts that it might be infeasible for VPS-W coatings to be directly used as hydrogen isotopes permeation barrier from the viewpoint of bred tritium gas-driven permeation through the first wall. Further investigations on the coatings effects on hydrogen permeation have been done by employing physical sputter-deposited W coatings and the results are presented in Chapter 6 and Chapter 7.

Chapter 6

Hydrogen isotopes gas- and plasma-driven permeation through sputter-deposited tungsten coated F82H

As presented in the previous chapter, vacuum plasma-sprayed tungsten (VPS-W) coatings reduce hydrogen PDP fluxes significantly. The coatings, however, have been found to have connected pores. Therefore, from the viewpoint of bi-directional permeation, VPS-W coatings are not efficient to suppress the bred tritium GDP from the breeding blankets to the edge plasma. In this chapter, a different type of tungsten coatings, i.e., physical sputter-deposited tungsten (SP-W) coatings are prepared. The microstructure of SP-W is characterized and the results of hydrogen isotopes GDP and PDP through SP-W coated F82H membranes are presented. In these experiments, SP-W shows different permeation properties compared to that of VPS-W.

6.1 Microstructural characterization of SP-W

Figure 6.1 shows the SEM images of the investigated samples. The SP-W coatings surface (figure 6.1(a)) is well-organized with an average crystal size of ~100 nm. EDS analysis yields the as-received surface elemental composition of: C (0.7 wt%), O (0.1 wt%), and W (99.2 wt%). Columnar W grains are observed from the cross-section views as indicated in figure 6.1(b, d). The W/F82H interface is sharp without voids, cracks or other visible defects. The kinetics of SP-W coatings growth is controlled by the mobility of the W atoms on the substrate surface. This mobility can be enhanced by increasing the temperature or by supplying impact energy through ion bombardment. At a given temperature, the sputtering-gas pressure determines the average impact energy of the sputtered W atoms as they arrive on the substrate. As the pressure increases, the impact energy decreases. The readers are referred to reports by Shen et al. [175] and E. Vassallo et al. [176] for the detailed microstructural properties of SP-W coatings.

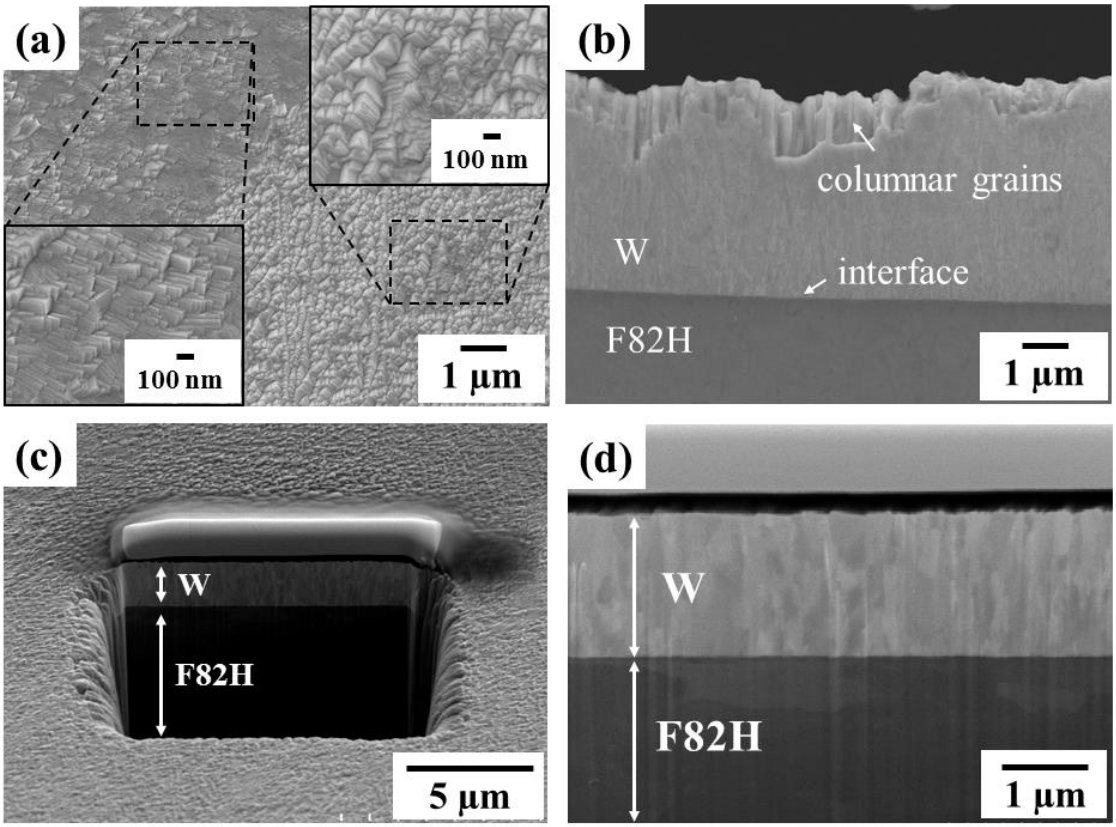

Figure 6.1 (a) SP-W coatings surface (as-deposited), (b) polished cross-section and (c, d) FIB cross-section of SP-W coated F82H.

XRD analysis has also been performed. Shown in figure 6.2(a) is the XRD diffraction pattern of SP-W coatings used in the present work. The XRD diffraction pattern for bulk polycrystalline W (PCW) [177] is shown for comparison. Reflection peaks of (110), (211), and (220) of bcc W phase are mainly observed and SP-W shows a strong (110) preferred orientation.

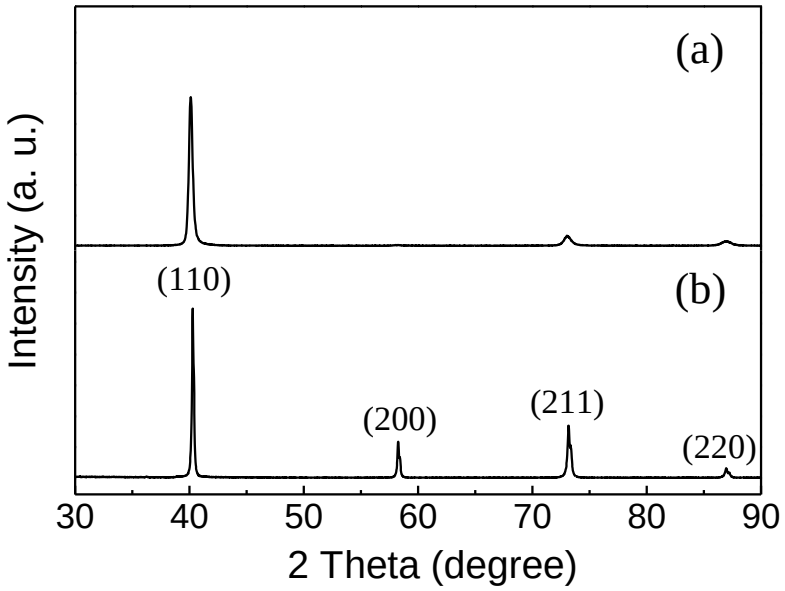

Figure 6.2 XRD diffraction patterns of (a) SP-W coatings and (b) bulk polycrystalline W [177].

6.2 Gas-driven permeation

6.2.1 Characteristics of GDP through SP-W coated F82H

Shown in figure 6.3 are the pressure dependent steady-state hydrogen GDP fluxes through SP-W coated F82H from 250 ℃ to 540 ℃, from which one can find a linear relation between the GDP flux and the square-root of upstream pressure, indicating that hydrogen isotopes GDP through SP-W coated F82H is diffusion limited.

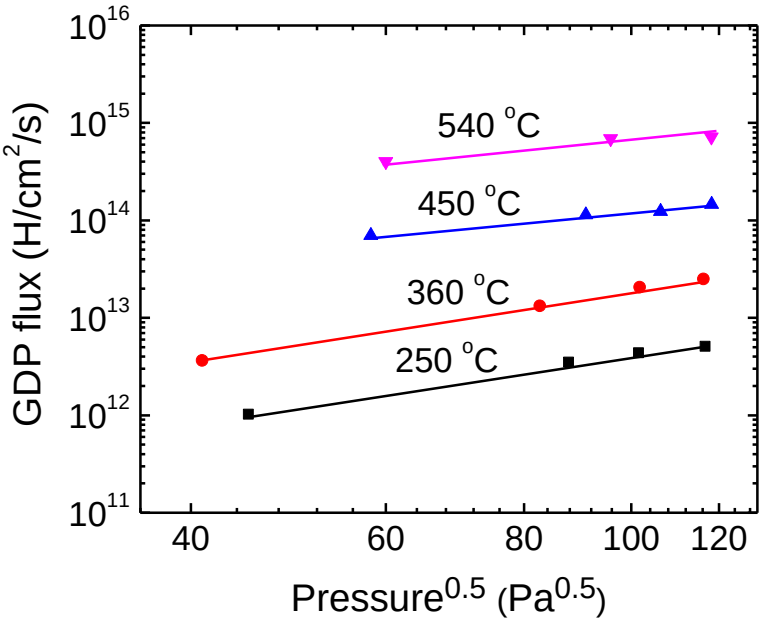

Figure 6.3 Steady-state hydrogen GDP fluxes through a SP-W coated F82H membrane in the temperature range of 250-540 ℃. The thicknesses of SP-W coatings and F82H substrate are 0.5 μm and 0.5 mm, respectively.

Similar to the experiments performed for VPS-W coated F82H samples, the temperature dependent steady-state deuterium GDP fluxes through SP-W coated F82H in two opposite directions have also been measured. The upstream deuterium pressure is set at ~10^4 Pa. The thicknesses of SP-W coatings and F82H substrate are 1.5 μm and 1 mm, respectively. The results are shown in figure 6.4. In the temperature range of 150-550 ℃. The GDP fluxes are reduced significantly by SP-W coatings and the permeation direction does not matter. This is because the SP-W coatings have a dense and pore-free structure, for a two-layer membrane, the effective permeability Φ_{eff} is invariant to relative position of layers (see Eq. (2.18) of Chapter 2), the steady-state permeation, therefore, is not influenced by the order of the layers. The permeation reduction factor (PRF) (see Eq. (2.17) of Chapter 2) has been calculated to be PRF ≈ 50.

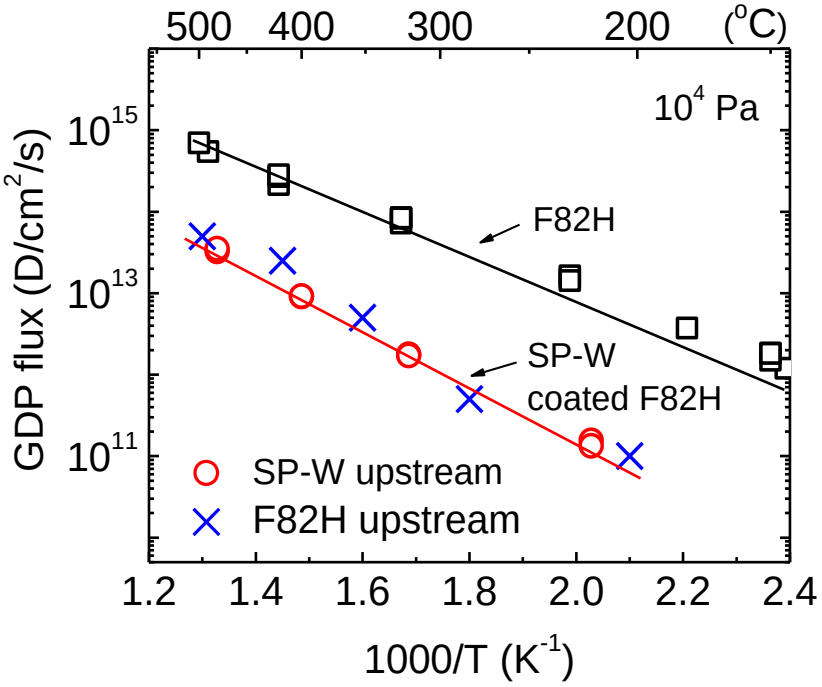

Figure 6.4 Steady-state deuterium GDP fluxes through SP-W coated F82H in two opposite directions. The upstream deuterium pressure is set at ~10^4 Pa. The thicknesses of SP-W coatings and F82H substrate are 1.5 μm and 1 mm, respectively. A 1 mm thick bare F82H membrane is used for comparison.

6.2.2 Permeability, diffusivity and solubility for SP-W

Based on the gas-driven permeation theory for a two-layer membrane (see Section 2.2.2 of Chapter 2), the hydrogen transport parameters including permeability, diffusivity and solubility of the coating material could be evaluated by the measurements of steady-state GDP flux and time-lag of bare and coated membranes.

Using Eq. (2.18) and the steady-state GDP data shown is figure 6.4, the hydrogen and deuterium permeability Φ (mol cm^{-1} s^{-1} Pa$^{-0.5}$) for SP-W is obtained as:

$$\Phi_{(\mathrm{H})} = 6.8 \times 10^{-12} \exp\left(\frac{-0.71\ eV}{kT}\right) \tag{6.1}$$

$$\Phi_{(\mathrm{D})} = 4.1 \times 10^{-12} \exp\left(\frac{-0.71\ eV}{kT}\right). \tag{6.2}$$

where *k* is the Boltzmann's constant and T is the temperature (K).

Shown in figure 6.5 is the measured permeability. The experimental values are comparable to some of the literature data for PCW [95-97, 178] and SP-W [179].

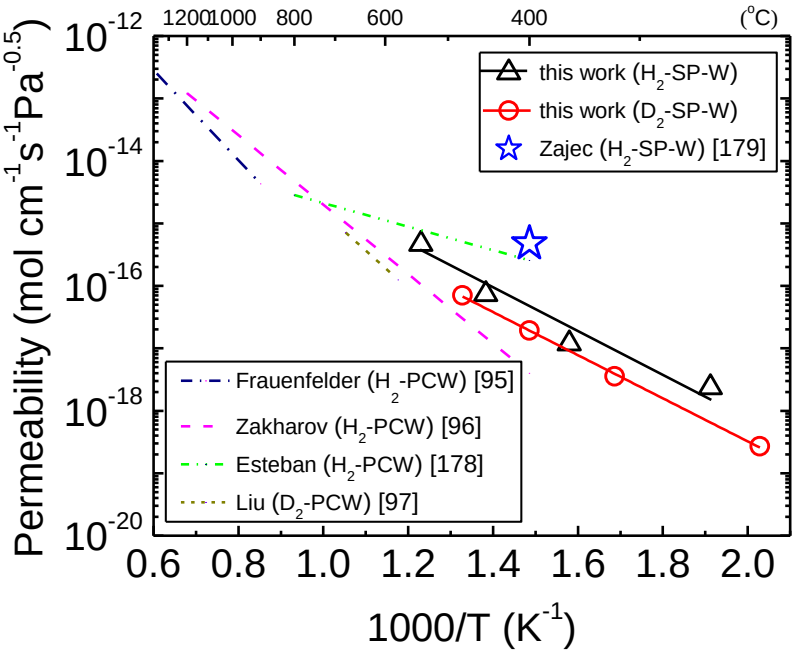

Figure 6.5 Measured hydrogen isotopes permeability for SP-W coatings. Zajec's [179], Frauenfelder's [95], Zakharov's [96], Esteban's [178] and Liu's [97] data are shown for comparison.

A more extensive study on the hydrogen permeation kinetics has been performed where four continuous permeation breakthrough curves are monitored, as shown in figure 6.6. It is evident that the first permeation exhibits considerably different kinetics compared to the following runs while those following runs are similar to each other. This phenomenon has also been reported by other researchers [97, 179-180] and is thought to

be caused by the trapping sites for hydrogen isotopes existing in the samples. After the first run of permeation, the trapping sites are occupied by deuterium, thus the steady-state permeation for the following runs are quickly built up.

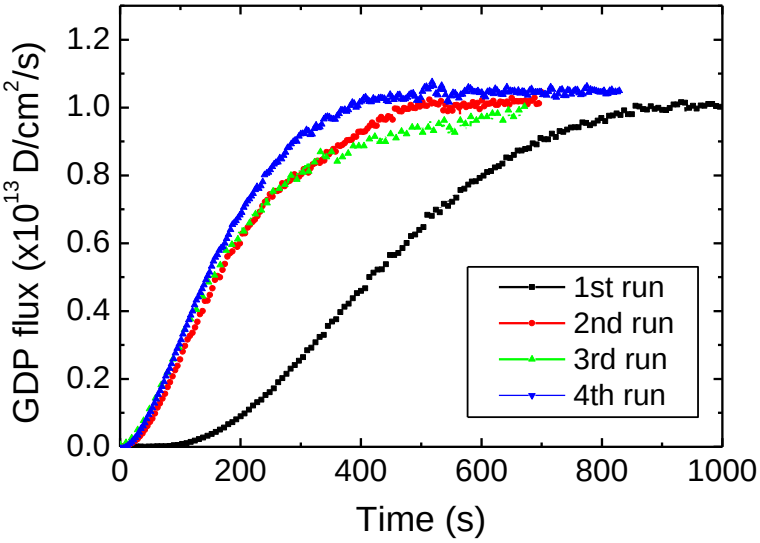

Figure 6.6 Permeation transients of four continuous breakthrough curves through SP-W coated F82H membrane. In this case, the thicknesses of SP-W coatings and F82H substrate are 3.8 μm and 0.2 mm, respectively. Deuterium gas is introduced at $t = 0$ while the pressure is set at ~10^4 Pa and the temperature is kept at 400 ℃.

At 400 ℃, the measured time-lag for SP-W coated F82H varies from ~600 s to ~230 s at different runs of permeation. While the time-lag for bare F82H membrane is below 10 s [181], hence the pinholes or micro-porosity in the SP-W coatings could be neglected. In the opposite case the permeation flux should rapidly increase towards steady-state value.

The hydrogen diffusivity is affected by the trapping sites in the W coatings since the permeation transient changes at different runs of permeation. In this study, the diffusivity is measured from 200 ℃ to 550 ℃ by gradually increasing the sample temperature, which means that during two measurements (~2 h) there is degassing or de-trapping of hydrogen

from the sample. Thus, trapping effects on the hydrogen migration still exist. The evaluated diffusivity is referred as effective diffusivity D_{eff}. Based on Eq. (2.21) of Chapter 2, the hydrogen and deuterium effective diffusivity D_{eff} ($\text{cm}^2\ \text{s}^{-1}$) for SP-W can be obtained as:

$$D_{\text{eff(H)}} = 4.0 \times 10^{-8} \exp\left(\frac{-0.41\ \text{eV}}{k\text{T}}\right) \tag{6.3}$$

$$D_{\text{eff(D)}} = 2.6 \times 10^{-8} \exp\left(\frac{-0.41\ \text{eV}}{k\text{T}}\right). \tag{6.4}$$

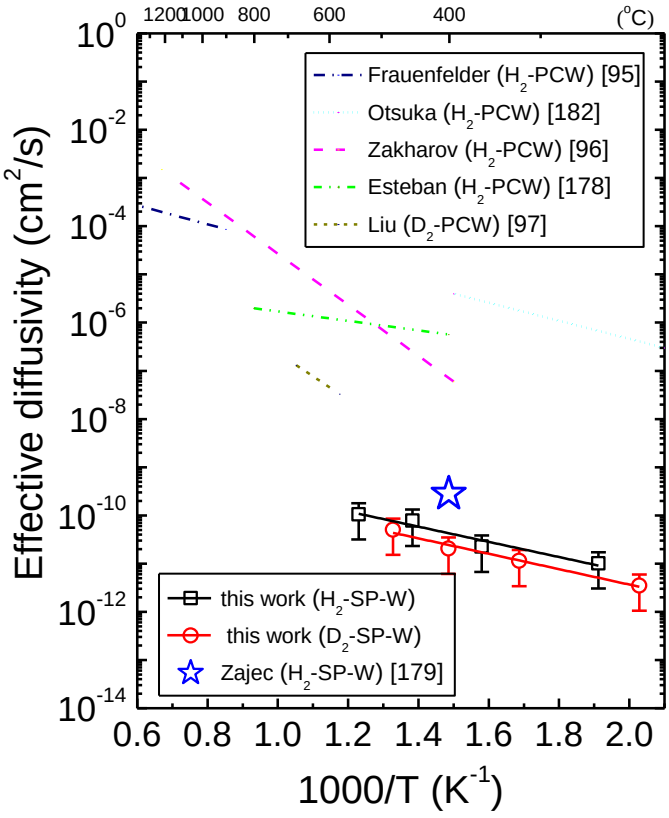

Figure 6.7 Measured effective hydrogen isotopes diffusivity for SP-W coatings. Zajec's [179], Frauenfelder's [95], Otsuka's [182], Zakharov's [96], Esteban's [178] and Liu's [97] data are shown for comparison.

From the expression $\Phi = DS$ the effective solubility S_{eff} (mol cm^{-3} Pa$^{-0.5}$) of hydrogen and deuterium in SP-W can be obtained as:

$$S_{\mathrm{eff(H)}} = 1.7 \times 10^{-4} \exp\left(\frac{-0.30\ \mathrm{eV}}{k\mathrm{T}}\right), \tag{6.5}$$

$$S_{\mathrm{eff(D)}} = 1.6 \times 10^{-4} \exp\left(\frac{-0.30\ \mathrm{eV}}{k\mathrm{T}}\right). \tag{6.6}$$

Shown in figure 6.7 and figure 6.8 are the measured effective diffusivity and solubility for SP-W. Literature data [95-97, 178-179, 182] are also shown for comparison. Despite large scatter of the solubility and diffusivity values of hydrogen isotopes in PCW, the evaluated S_{eff} is several orders of magnitude higher and D_{eff} is several orders of magnitude lower than the published range of values for PCW. Both the evaluated S_{eff} and D_{eff} are comparable to the value shown in Ref. [179] for SP-W.

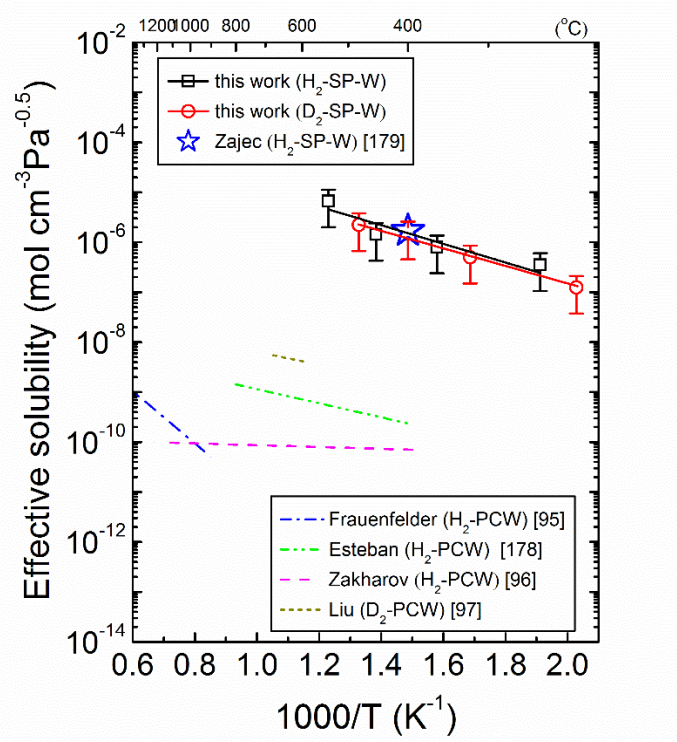

Figure 6.8 Measured effective hydrogen isotopes solubility in SP-W coatings. Zajec's [179], Frauenfelder's [95], Esteban's [178], Zakharov's [96] and Liu's [97] data are shown for comparison.

The probable explanation for high solubility and low diffusivity in SP-W is the presence of trapping sites for hydrogen isotopes. It has been widely accepted that trapping enhances the hydrogen solubility and decreases the diffusivity, while it does not impact the permeability [86, 183-184]. To simulate trapping effects on hydrogen transport, the DIFFUSE-code [185] has been executed employing various trap concentrations. Shown in figure 6.9 is the calculation results of hydrogen GDP breakthrough curves through W coated F82H at 500 ℃. In this case, the thicknesses of W coatings and F82H substrate are 0.5 μm and 0.5 mm, respectively. Because unfortunately it is not included in the DIFFUSE-code database, F82H has been approximated by pure α-Fe for convenience. Hydrogen trapping sites are assumed to be uniformly distributed. As shown in figure 6.9 that as the trap concentration increases, the lag-time increases, reaching the same steady-state permeation fluxes, which indicates that trapping enhances the hydrogen solubility and decreases the diffusivity, but does not influence the permeability.

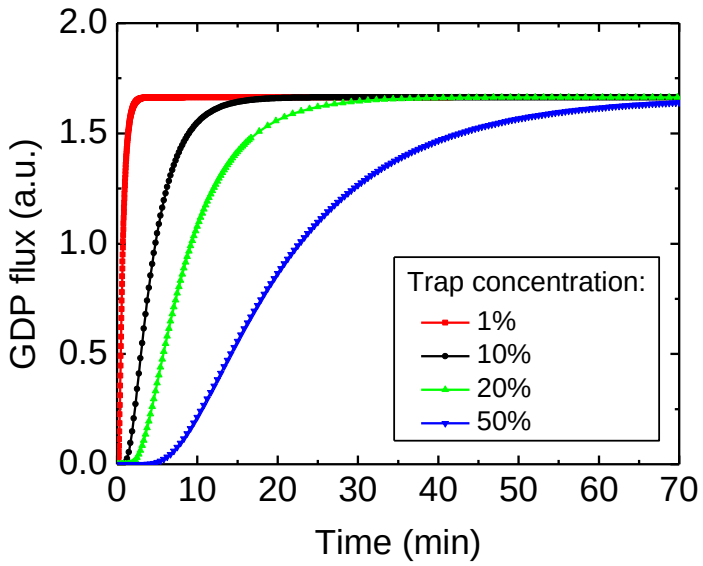

Figure 6.9 DIFFUSE-code calculations of hydrogen GDP breakthrough curves through W coated F82H.

6.2.3 Discussion

The hydrogen diffusion in W is strongly affected by the presence of microstructural inhomogeneities including grain boundaries, dislocations, voids, vacancy clusters and point defects, which are potential hydrogen trapping sites [179]. Whether these microstructural features can induce trapping effects is determined by the binding energy to hydrogen. With increasing the strength of trapping, traps are categorized as reversible and irreversible [186]. In the absence of traps, hydrogen diffusion is controlled by random-jumping process between interstitial lattice sites with a very short residence time for a diffusing hydrogen atom. Hydrogen diffusion is then described by the ideal lattice diffusivity D_L, governed by the activation energy for diffusion associated with the energy barrier between interstitial sites. Reversible trapping sites with high binding energy create an effectively higher barrier to hydrogen movement. Consequently, trapping decreases the rate of hydrogen transport in the lattice and increases the effective activation energy for diffusion. This trap-affected, or effective hydrogen diffusivity D_{eff} can be up to three orders of magnitude lower than D_L, depending on the nature and extent of trapping [187].

In a lattice containing only irreversible traps which can be saturated, hydrogen diffusivity decreases to D_{eff} during hydrogen uptake, until the irreversible traps are completely occupied with hydrogen. Ideal irreversible traps are saturated at a low hydrogen concentration and, once filled, there will be no interact with dissolved hydrogen, consequently, the D_{eff} value increases to D_L. In contrast, reversibly trapped hydrogen is in dynamic equilibrium with hydrogen dissolved in the lattice and represents a permanent impedance to hydrogen transport [188]. Therefore, the D_{eff} value in a lattice containing reversible traps is always less than D_L, and the difference is manifested at lower hydrogen concentration.

To describe the effects of reversible trapping on D_{eff}, Oriani assumed that dynamic equilibrium exists between the reversibly trapped hydrogen population and hydrogen in interstitial lattice sites [183]. In the case of a single type dominant trapping sites, the ratio of D_{eff} versus D_L is given as [183]:

$$\frac{D_{eff}}{D_L} = \frac{1}{1+\frac{C_T}{C_L}(1-\Theta_T)}, \quad (6.7)$$

where C_T and C_L are the trapped and lattice hydrogen concentrations and $\Theta_T = C_T/n_T$ is the occupancy of trapping sites. Since the evaluated $S_{eff} \gg S_L$ that the majority of dissolved hydrogen atoms in the W coating are in traps and the total hydrogen concentration $C_{tot.} = C_T + C_L$ is almost equal to the concentration of the trapped population $C_{tot.} \approx C_T (C_L \ll C_T)$. Therefore $C_T/C_L \approx S_{eff}/S_L$. By solving Eq. (6.7) using the hydrogen transport parameters in pure annealed polycrystalline W [95-97, 163, 178, 182] one can obtain $\Theta_T \approx 0.7$, hence the traps are mostly occupied. In a perfect lattice, solubility is determined by the heat of solution [189]. However, the effective hydrogen solubility S_{eff} can be increased dramatically by traps, where hydrogen accumulation alters the local heat of solution. For example, the hydrogen solubility in martensitic AISI 4135 steel is about four orders of magnitude higher than that in pure iron at 25 ℃ [190].

In this study, the significantly high S_{eff} and low D_{eff} are believed to be attributed to the trapping sites resulting from the characteristic microstructure of SP-W material. The average crystal size of SP-W coatings is ~100 nm as shown in figure 6.1, while for PCW it is roughly 100 μm [178], suggesting that most trapping sites might be located at grain boundaries, dislocations and vacancy clusters. Nevertheless, further investigations are still needed to address these issues.

6.3 Plasma-driven permeation

6.3.1 Permeation measurements

Shown in figure 6.10 are the deuterium PDP breakthrough curves through F82H with and without SP-W coatings at ~320 ℃. The thicknesses of SP-W coatings and F82H substrate are 1.5 μm and 1 mm, respectively. The deuterium PDP data through a 1 mm thick bare F82H membrane is shown for comparison. In these experiments, the ECR power

is set at 350 W and the ion bombarding energy is set at -100 V. The electron temperature and density are measured to be ~5 eV and ~1.2 × 10^{10} cm^{-3}, respectively. The net implantation flux is estimated to be ~1.2 × 10^{16} $D/cm^2/s$. The samples are in-situ degassed at 500 ℃ for 8 hours before experiments. Prior to deuterium PDP, argon plasma bombardment is conducted for 10 min at -50 V to reduce surface contamination. Time zero in figure 6.10 corresponds to the plasma-on time. The steady-state deuterium PDP flux has been measured to be ~6 × 10^{13} $D/cm^2/s$ for the SP-W coated F82H at 320 ℃, which is nearly two orders of magnitude higher than that for bare F82H. The deuterium breakthrough time for the SP-W coated F82H is evaluated to be ~760 s, which is significantly longer than that for bare F82H. It is believed to be attributed to the trapping effects on deuterium migration, i.e., the trapping sites in SP-W coatings extend the time of deuterium uptake.

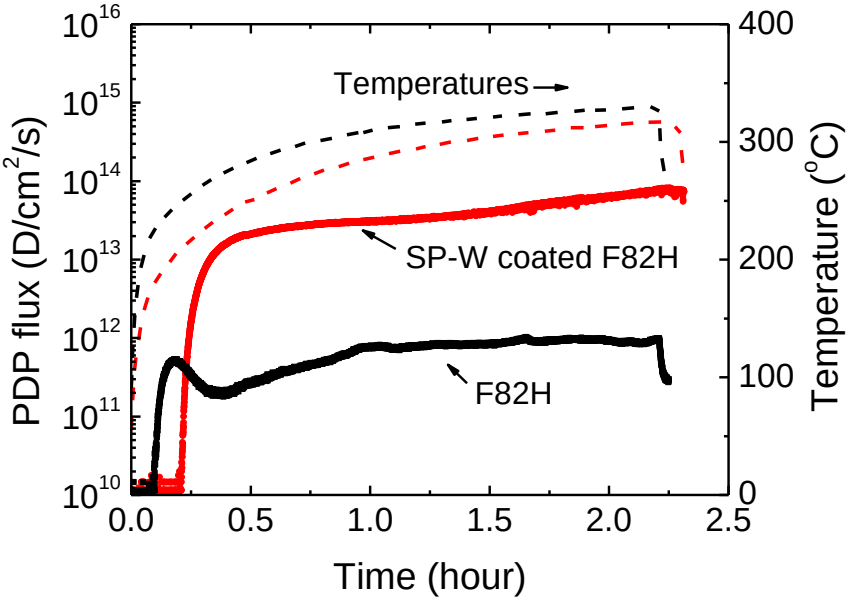

Figure 6.10 Deuterium PDP breakthrough curves through F82H with and without SP-W coatings at ~320 ℃. The thicknesses of SP-W coatings and F82H substrate are 1.5 μm and 1 mm, respectively. The thickness of the bare F82H membrane is 1 mm.

Deuterium PDP fluxes through SP-W coated F82H have also been measured as a function of temperature. Shown in figure 6.11 are the temperature dependence of steady-state deuterium PDP fluxes from 300 ℃ to 550 ℃.

The data for SP-W coated F82H indicate enhanced permeation fluxes [191]. Notice, however, that the permeation flux decreases with increasing temperature. Not presented here are similar data taken on hydrogen PDP through SP-W coated α-Fe membranes. Generally, the coatings leads to the reduction of hydrogen permeation through the metals in conditions of interaction with molecular hydrogen. However, experimental results on hydrogen ions or plasma permeation through the metals with coatings could be contradictory. There are a number of experimental studies [172, 192] showing that coatings can also increase the permeation flux when exposed to ions or plasma, which is in agreement with our results obtained in this work.

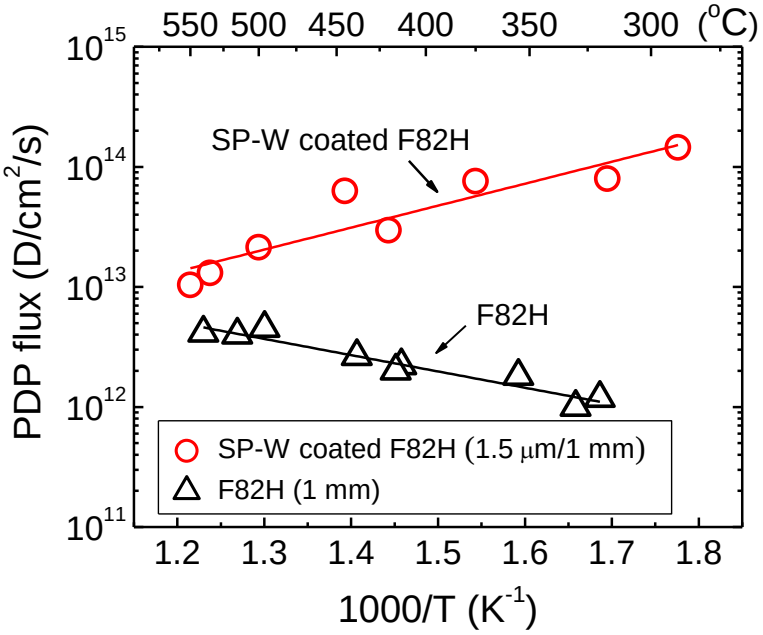

Figure 6.11 Temperature dependence of steady-state deuterium PDP fluxes through F82H with and without SP-W coatings.

Hydrogen ions or plasma reaching either surface are not guaranteed immediate release. At the plasma-facing surface, with the exception of extremely high temperatures, recombination of the atoms into molecules must occur before release is possible. The hydrogen recombination process is defined by the expression [115]:

$$J_{-} = K_r C^2, \tag{6.8}$$

where J_{-} is the recombination flux, K_r is the recombination coefficient and C is the hydrogen concentration at the plasma-facing surface. A material with a high recombination coefficient promotes rapid release from the surface, keeping the overall hydrogen concentration low throughout the material. A material with a low recombination coefficient prevents rapid release, elevating the hydrogen concentration throughout the material. The low recombination coefficient leads to higher hydrogen inventory in the material with potentially higher release rates out of the backside of the plasma-facing material (permeation).

6.3.2 Surface recombination coefficient for SP-W

Surface recombination coefficient of deuterium for SP-W is estimated by a one-dimensional steady-state permeation model with the input data taken from experiments. Shown in figure 6.12 is the effective deuterium diffusivity D_{eff} evaluated from the time-lag method [121] using the gas permeation technique. The D_{eff} (cm^2s^{-1}) for SP-W coated F82H from 250 ℃ to 550 ℃ is given as:

$$D_{\text{eff}} = 4.9 \times 10^{-4} \exp\left(\frac{-0.24\ \text{eV}}{k\text{T}}\right). \tag{6.9}$$

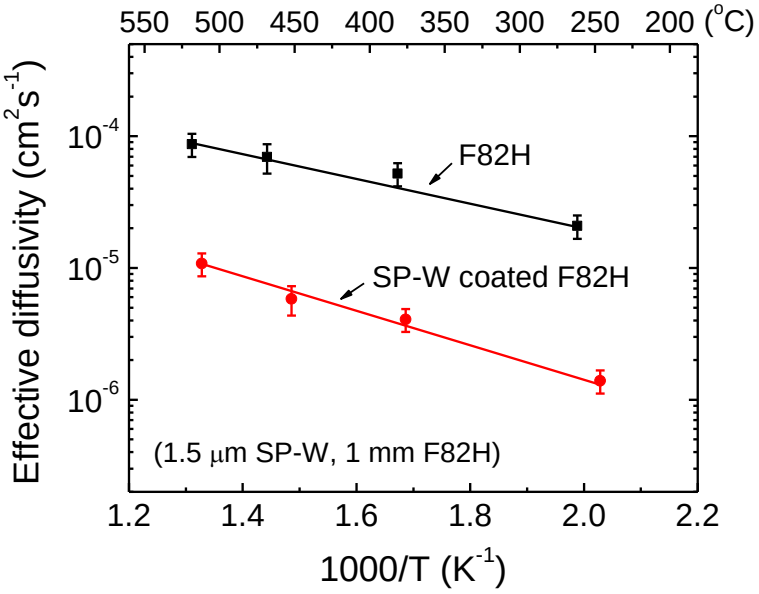

Figure 6.12 Effective deuterium diffusivity for SP-W coated F82H. The data for bare F82H is shown for comparison.

Based on our previous work [74-75], deuterium PDP under the given conditions takes place in the RD-regime [130], which is recombination-limited hydrogen release from the upstream surface and the diffusion-limited hydrogen release from the downstream surface. The steady-state hydrogen PDP flux J_+ is given by:

$$J_+ = \frac{D_{\text{eff}}}{L}\sqrt{\frac{J_0}{K_r}}\,, \tag{6.10}$$

where L is the membrane thickness and J_0 is the net implantation flux. Eq. (5.10) suggests that using the data on D_{eff} shown in figure 6.12, the recombination coefficient K_r can be obtained from the measured data on J_0 and J_+.

Shown in figure 6.13 is the evaluated K_r (cm^4 s^{-1}) of deuterium for SP-W and F82H which can be expressed as:

$$K_r = 1.2 \times 10^{-10}\exp\left(\frac{-1.21\ \text{eV}}{k\text{T}}\right). \tag{6.11}$$

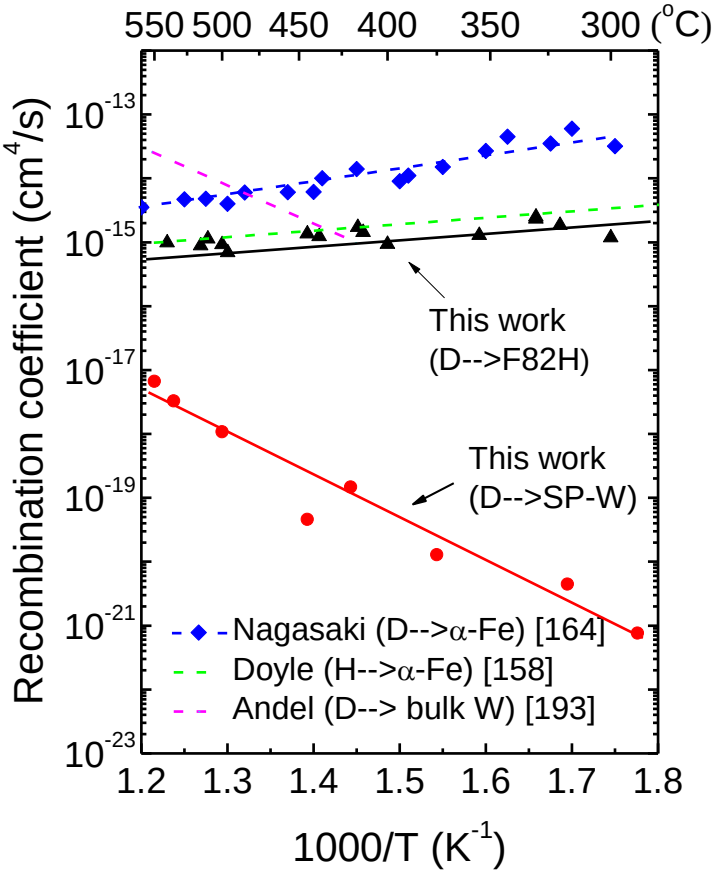

Figure 6.13 Evaluated surface recombination coefficient of deuterium for SP-W. Nagasaki's [164], Doyle's [158] and Andel's [193] data are shown for comparison.

To allow a comparison, literature data are also shown for comparison [158, 164, 193]. It has been found that the K_r for SP-W is orders of magnitude different from that reported for bulk polycrystalline W [193], meaning that the SP-W shows a considerably different surface recombination kinetics. The K_r for SP-W increases with increasing temperature from 300 ℃ to 550 ℃. This explains the temperature dependence of PDP fluxes shown in figure 6.11, i.e., deuterium PDP flux decreases with increasing temperature. SP-W has a significantly low K_r compared to F82H, which leads to the enhanced PDP fluxes.

6.3.3 Deuterium retention

Deuterium retention analysis has been performed by the thermal desorption spectroscopy (TDS) after steady-state deuterium PDP experiments. The implantation fluence is ~1×10^{20} D/cm^2. After plasma exposure, the samples are cooled down inside the VEHICLE-1 test chamber. TDS is conducted in a separate vacuum system with delays of 18 ± 2 h between implantation and desorption. Thus, only static deuterium retention is measured. During TDS measurements, samples are heated by an infrared heater from room temperature to 600 ℃ at a ramp rate of ~0.3 ℃/s and then held at 600 ℃ for a further period of 1 h to ensure deuterium is entirely released. The temperature is measured by a thermocouple. The amount of deuterium retained in the samples is determined by integrating the partial pressures of D_2 and HD during thermal desorption.

Shown in figure 6.14 are the deuterium thermal desorption spectra released from SP-W coated F82H and bare F82H. For SP-W coated F82H, the TDS spectra are characterized by desorption peaks positioned at 400-530 ℃ depending on the target temperature. For bare F82H, the TDS spectra are similar to each other in the temperature range of 330-540 ℃ and desorption peaks are observed primarily at ~550 ℃ independent of the target temperature. A second low-intensity peak at ~350 ℃ is observed only in the spectrum for the bare F82H at target temperature of 330 ℃.

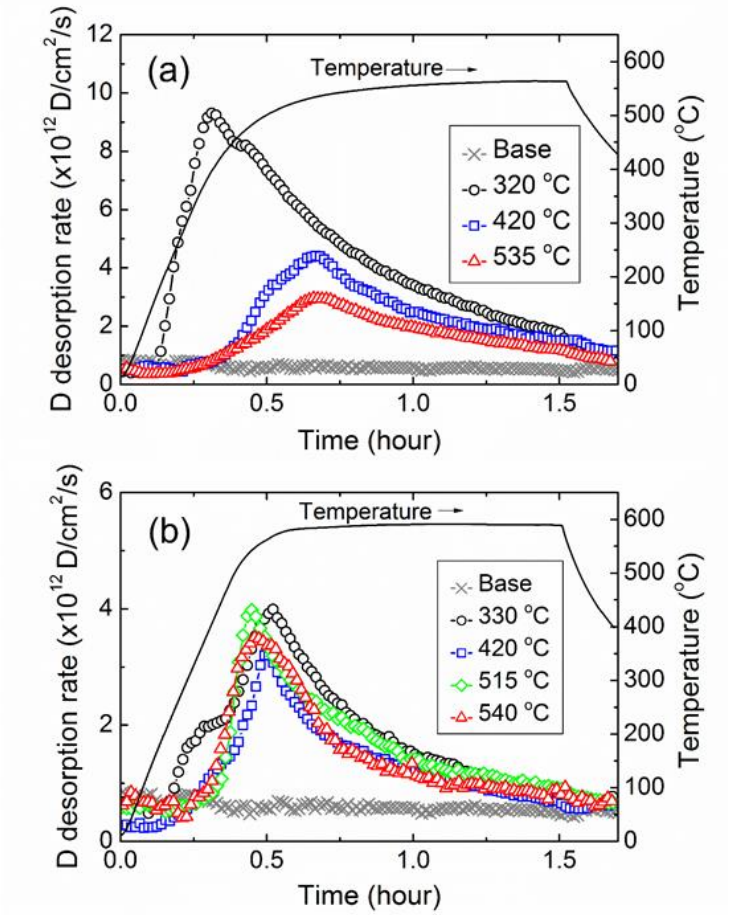

Figure 6.14 Thermal desorption spectra of deuterium released from (a) SP-W coated F82H and (b) bare F82H after plasma exposure at various temperatures. The thicknesses of SP-W coatings and F82H substrate are 1.5 μm and 1 mm, respectively.

Shown in figure 6.15 is the temperature dependence of deuterium retention in F82H with and without SP-W coatings. Experimental data by nuclear reaction analysis (NRA) method up to 7 μm in PCW [194-195] and by TDS method in single crystalline W (SCW) [196] are also shown for comparison. All data show the same tendency that a reduction of the deuterium retention in W with increasing temperature. The amount of retained deuterium in SP-W coated F82H is about a factor of 3 higher than that of bare F82H in the temperature range of 320-420 ℃ and the differences become smaller with increasing

temperature. Also indicated in figure 6.15 is that the deuterium retention in SP-W coatings is higher than some of the reported data for PCW and SCW. Note that, since NRA allows measuring only the deuterium near the implantation side up to a limited depth, the total amount of deuterium is significantly underestimated compared to TDS, especially at elevated temperatures and long-time implantation when more deuterium diffuses into the bulk of the sample. The high deuterium retention in SP-W coated F82H is presumably due to the trapping sites for hydrogen isotopes in SP-W coatings. Figure 6.16 shows an illustrative structure of the physical sputter-deposited W. The possible trapping sites might be located at the grain boundaries, dislocations and vacancy or vacancy clusters.

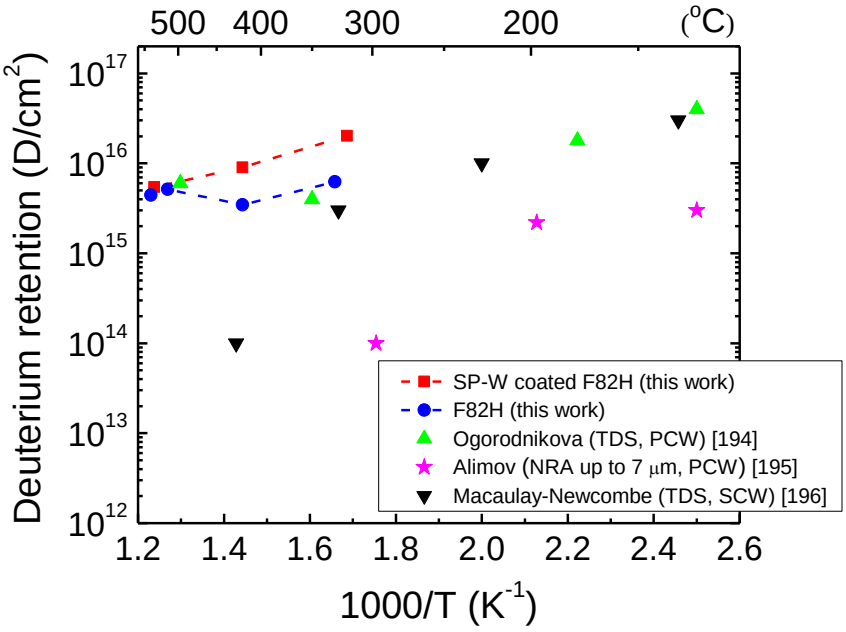

Figure 6.15 Deuterium retention in F82H with and without SP-W coatings exposed to 100 eV D^+ at different temperatures up to a fluence of 1×10^{20} D/cm^2. Experimental data by Ogorodnikova et al. [194] for PCW irradiated with 200 eV D^+, Alimov et al. [195] for PCW irradiated with 200 eV D^+ and Macaulay-Newcombe et al. [196] for SCW irradiated with 500 eV D^+ are also shown for comparison.

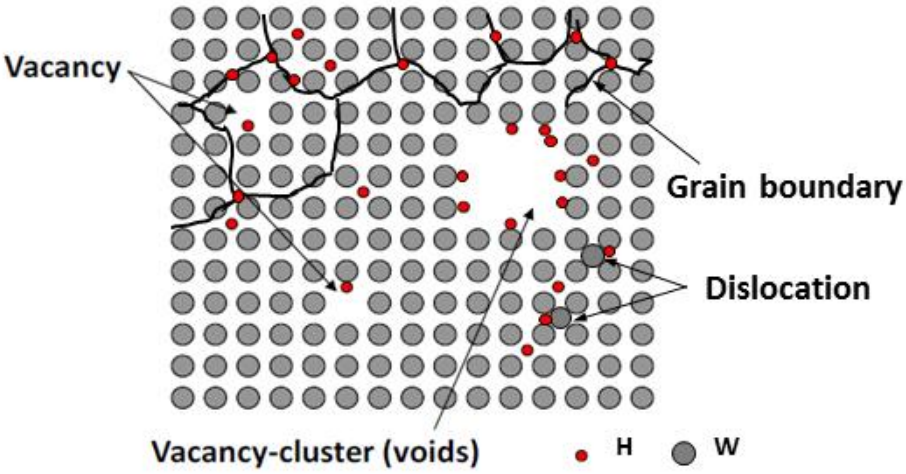

Figure 6.16 A schematic diagram of possible trapping sites in SP-W coatings.

6.3.4 Deuterium depth concentration profile

The deuterium depth concentration profile in the SP-W coated F82H membrane has been measured by the secondary ion mass spectrometry (SIMS) technique after steady-state deuterium PDP experiments. In this case, the thicknesses of SP-W coatings and F82H substrate are 1 μm and 1 mm, respectively. The membrane temperature is kept at ~250 ℃ during PDP. The implantation fluence is ~1×10^{20} D/cm^2. After plasma exposure the flange sample is cooled down inside the VEHICLE-1 test chamber and then cut into small specimens with a size of 7 × 7 × 1 mm for TDS and SIMS separately. The deuterium static retention in the sample has been measured by TDS to be ~1.2×10^{16} D/cm^2, which is comparable with the data shown in figure 6.15.

The SIMS depth profile is obtained by the ATOMICA SIMS-4000 instrument using a 5 keV O_2^+ primary ion beam and collecting positive ions of D^+, $^{186}W^+$, $^{56}Fe^+$, $^{52}Cr^+$ and $^{12}C^+$, etc. The beam is raster-scanned over an area of 150 μm × 150 μm. The beam current is set

at 250 nA during profiling. The main characteristics and the measurement setup of the SIMS apparatus are summarized in table 6.1.

Table 6.1 Analytical parameters for SIMS analysis in this work.

Instrumentation	ATOMICA SIMS-4000
Primary beam	O_2^+
Primary beam impact energy	5 keV
Primary beam intensity	250 nA
Primary beam diameter	5 µm
Vacuum pressure	4×10^{-8} Pa
Secondary ion polarity	(+)
Analyzed secondary ions	D^+, $^{186}W^+$, $^{56}Fe^+$, $^{52}Cr^+$, $^{12}C^+$, etc.
Raster-scanned area	150 µm × 150 µm
Sputtering rate	~0.18 nm/s in W

In secondary ion mass spectrometry the emission of secondary ions from a surface under ion bombardment can be described as [197]:

$$I_m = I_p Y_m \alpha \theta_m \eta, \tag{6.12}$$

where I_m is the secondary ion current of species m, I_p is the primary ion flux, Y_m is the sputtering yield, α is the ionization probability, θ_m is the fractional concentration of m in the surface layer and η is the transmission of the analysis system.

The two fundamental parameters are Y_m and α. Y_m is the total yield of sputtered particles of species m, neutral and ionic, per primary ion impact. It increases linearly with primary ion flux. It also increases with primary ion mass and energy although not linearly. Ionization occurs at the emission of sputtered particles with the consequence that the matrix participates in the electronic process. This means that the secondary ion yield is strongly

influenced by the electronic state of the material being analyzed and it is very sensitive to the electronic state of the atom or molecule to be ionized and to the matrix from which they are emitted. As a matter of fact, the secondary ion yield sputtered from the same matrix is a function of the ionization potential of the sputtered atom but it can be greatly enhanced by the presence of electronegative species, e.g. oxygen, at the surface. This is the well-known matrix effect [198-199] and it might bring significant complications when a quantification of SIMS data is required.

For compounds with a multi-layer structure, the use of SIMS to monitor elemental distributions through these layers and interfaces of varying composition is extremely difficult due to the changing matrix effects. Proper calibration of ion yield and sputtering yield, however, can make qualitative concentration and depth measurements possible for these samples. In the present SIMS analysis of W/F82H bi-layer structure, regardless of the system factor, the ratio of secondary ion yields of Fe^+ and W^+ can be expressed as:

$$\frac{I_{\mathrm{Fe}^+}}{I_{\mathrm{W}^+}} \propto \frac{Y_{\mathrm{Fe}}}{Y_{\mathrm{W}}} \cdot \frac{\alpha_{\mathrm{Fe}^+}}{\alpha_{\mathrm{W}^+}}, \tag{6.13}$$

in which the sputtering yields for Fe (Y_{Fe}) and W (Y_{W}) can be calculated by Monte Carlo simulation codes such as TRIM [109] and EDDY [111], etc.

To the first order of approximation, it is assumed that the ratio of deuterium ionization probability in the F82H and W matrixes is equal to the ratio of ionization probability for Fe and W, while the interaction potential [200] and the local thermal equilibrium [201] might be some hidden factors:

$$\frac{\alpha_{\mathrm{D}^+(\mathrm{Fe})}}{\alpha_{\mathrm{D}^+(\mathrm{W})}} = \frac{\alpha_{\mathrm{Fe}^+}}{\alpha_{\mathrm{W}^+}}. \tag{6.14}$$

Therefore, the intensity of secondary D^+ ions has been converted qualitatively to the deuterium concentration using the above hypothesis approach, i.e., normalizing the D^+ intensity to the matrix species ($^{186}W^+$ and $^{56}Fe^+$). The result is shown in figure 6.17(a), in which the deuterium concentration is referred to the left axis. Deuterium is observed with

the highest concentration at the near surface. It is retained at a high level until the depth of ~1 μm in the W coatings, after which the concentration has dropped by about two orders of magnitude in the F82H substrate.

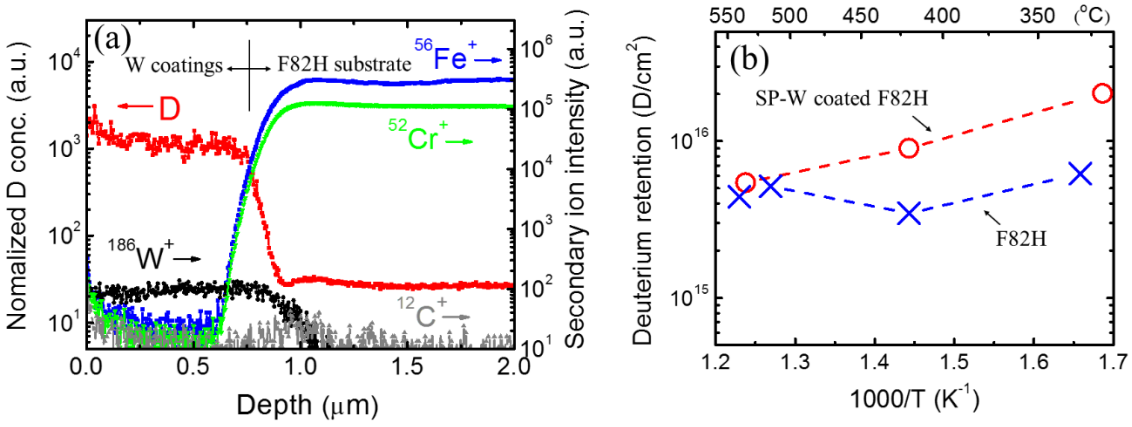

Figure 6.17 (a) Deuterium depth concentration profile of SP-W coated F82H by SIMS and (b) deuterium retention in F82H with and without SP-W coatings (replotted from figure 6.15).

According to the theory of thermodynamics, the diffusion is introduced by the different chemical potential of each component. Atoms transport from the high chemical potential area to the low chemical potential area. The real driving force for diffusion is not the concentration gradient but the chemical potential gradient. Therefore, the hydrogen chemical potential is continuous throughout the multi-layer membrane but not the concentration gradient. The hydrogen concentration ratio at the interface is expressed as (Eq. (2.19)) [127]:

$$\frac{C_{1,i}}{C_{2,i}} = \frac{S_1}{S_2}, \tag{6.15}$$

where index *i* denotes the position at the interface. Based on the data obtained in this work, the effective deuterium solubility in SP-W coatings (figure 6.8) is about two orders of

magnitude higher than that in F82H substrate (figure 4.12) at 250 ℃, which is in agreement with the theoretical prediction of Eq. (6.15). Such a deuterium depth profile has also been reported in Ref. [202] for multi-layer coatings of Fe/Er_2O_3/F82H evaluated by the $D(^3He, p)^4He$ nuclear reaction analysis (NRA). Notice that, the increase of the deuterium and carbon signals at the W/F82H interface may be due to an impurity layer formed at the beginning of the W deposition process.

The deuterium retention data is shown in figure 6.17(b) for a comparison. It is indicated that the increased deuterium retention in SP-W coated F82H corresponds to the high deuterium concentration in the W coatings.

6.4 Summary

Hydrogen and deuterium GDP and PDP experiments have been conducted for SP-W coated F82H. SP-W coatings have been found to reduce GDP fluxes, the PDP fluxes, however, are enhanced by SP-W. Characterization analyses indicate that microstructure and surface properties of the coatings significantly alter PDP flux. Surface recombination is a key process determining the PDP flux.

Transport parameters including diffusivity, permeability, solubility and surface recombination coefficient have been evaluated for SP-W coatings. It has been found that the permeability for SP-W is close to the literature data for PCW. However, the effective diffusivity and solubility are different from the literature data by several orders of magnitude, indicating that the traps influence on hydrogen migration in W.

Static deuterium retention in SP-W coated and uncoated F82H has been measured by TDS. Increased deuterium retention in SP-W coated F82H has been observed compared with that in bare F82H. SIMS depth profile shows a good agreement with the retention data and exhibits a sign of “uphill diffusion” of deuterium in the W/F82H bi-layer structure.

For a future fusion reactor, based on the present data one predicts that SP-W coatings might increase hydrogen isotopes PDP fluxes and fuel retention as well in the first wall. As a proof-of-principle experiment, a permeation probe employing SP-W coated F82H membrane has been installed in the QUEST spherical tokamak and the data are presented in Chapter 7.

Chapter 7

Hydrogen plasma-driven permeation through SP-W coated F82H in the QUEST spherical tokamak

As presented in the previous chapter, SP-W coatings tend to enhance plasma-driven hydrogen permeation flux. In order to investigate SP-W coatings effects on hydrogen PDP in a fusion device, a permeation probe of SP-W coated F82H membrane has been installed in the QUEST spherical tokamak at Kyushu University. Presented in this chapter are the results of the measurements during conditioning steady-state discharge hydrogen plasma heated with 2.45 GHz electron cyclotron resonance (ECR). These data have been compared with our previous experimental results by a permeation probe of bare F82H membrane in QUEST [203].

7.1 QUEST spherical tokamak

QUEST (Q-shu University Experiment with Steady State Spherical Tokamak, as shown in figure 7.1 [204]) is a medium size spherical tokamak which aims to achieve the steady-state operation with the capability to attain high β rather than conventional tokamaks [205]. The major radius and the minor radius of QUEST are R = 0.68 m and a = 0.4 m, respectively [206].

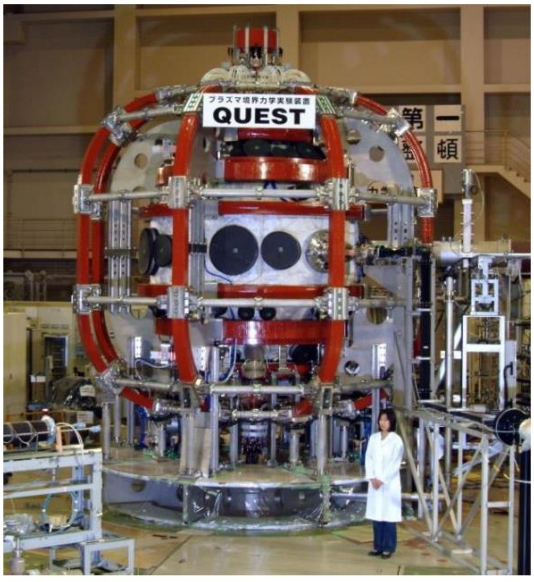

Figure 7.1 The QUEST spherical tokamak [204].

The vacuum chamber of QUEST is made of stainless steel 304 L with a wall thickness of 8-12 mm. The chamber radius and height are ~1.4 m and ~2.8 m, respectively. The total surface area of the chamber wall is ~35.5 m^2 and the volume is ~13 m^3 including the extension ports. Outboard limiters made of tungsten are installed on the outside walls at a major radius of R = 1.35 m. The pumping system for the QUEST chamber, which consists of a turbo-molecular pump and 3 cryopumps, has a pumping speed of 3.8 $m^3 s^{-1}$. Hydrogen plasmas can be produced by ECR with three kinds of RF sources: 2.45 GHz, 8.2 GHz and 28 GHz.

7.2 Permeation setup in QUEST

In the present work, hydrogen plasma-driven permeation experiments have been performed for the low temperature, low density slab plasma in discharge cleaning experiments. The slab plasma means plasma produced in the electron cyclotron resonance region without poloidal field (i.e., no closed flux surface, as shown in figure 7.2).

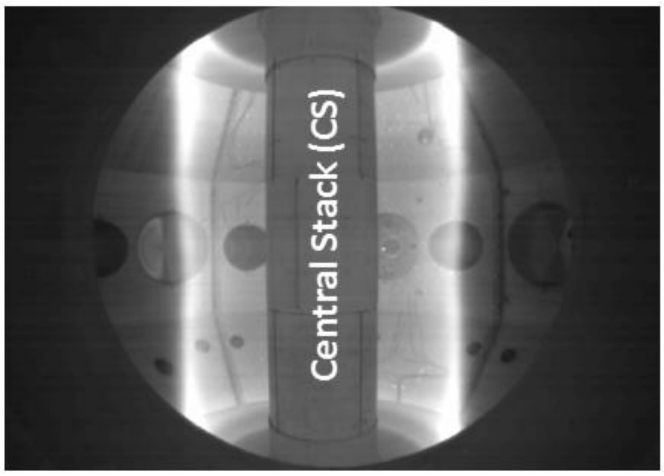

Figure 7.2 ECR cleaning plasma in QUEST (slab plasma).

Schematic view of the QUEST tokamak cross-section and the probe position are shown in figure 7.3(a). The hydrogen working gas is supplied from a nozzle at the central

stack. Gas puff is done in a pulse mode, the opening time of which varies in the range of 5-100 ms with the fueling rate of 2.0×10^{21} H s^{-1}. The interval between puffs is in the range from 1 s to 50 s. The fueling gas pressure in the vessel is set in the range of $1\text{-}10 \times 10^{-3}$ Pa. Hydrogen plasma is produced by ECR waves alone at 2.45 GHz (<10 kW) in this work. The annular slab plasma is indicated in pink in figure 7.3(a). The plasma diameter can be adjusted by changing the toroidal magnetic field. Plasma parameters are measured by an array of Langmuir probes at the "top plate". In addition, upper and lower oblique plates and vertical plates (radiation shield) are installed and denoted by grey lines. The wall temperature is kept at ~ 100 ℃ during experiments.

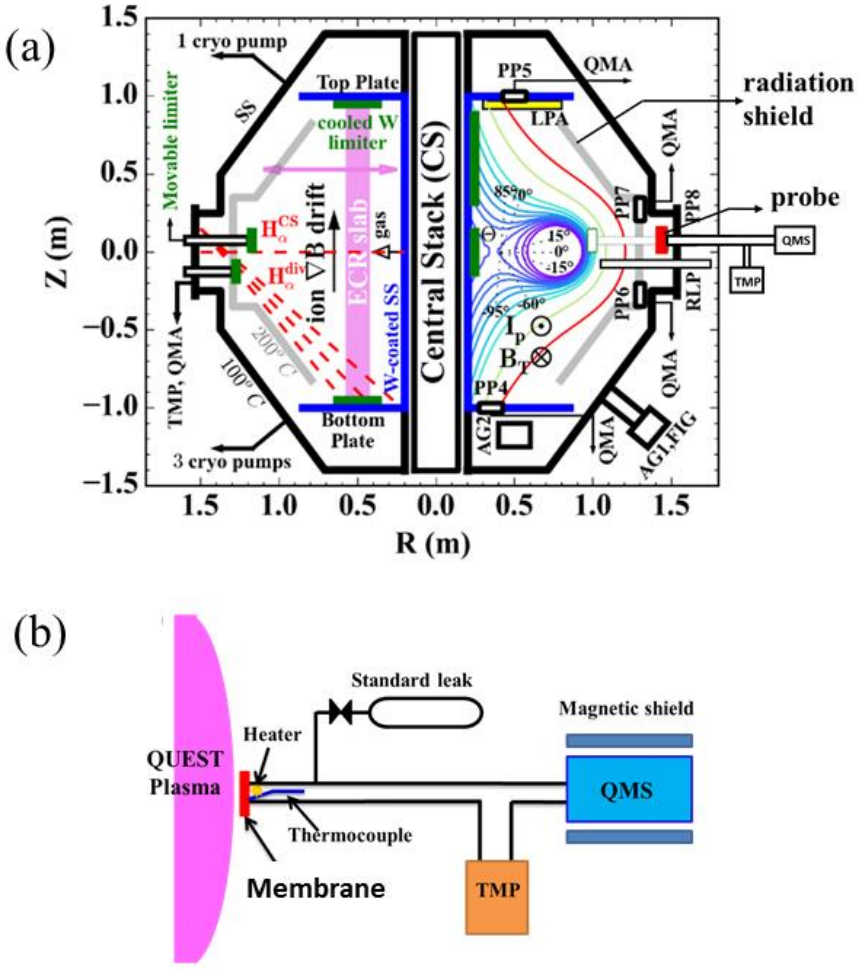

Figure 7.3 (a) Schematic view of QUEST cross-section and (b) schematic diagram of the PDP setup.

Shown in figure 7.3(b) is a schematic diagram of the PDP setup. In the present work, a SP-W coated F82H sample is used. The permeation probe has been installed inside the closed port at the mid-plane and the membrane is 15 cm recessed from the radiation shield. A resistive heater is set behind the membrane to keep the sample temperature in the range of 300-350 ℃. The temperature is measured by a thermocouple attached to the downstream surface. Hydrogen permeation flux is measured by a quadrupole mass spectrometer (QMS) which has been calibrated by a hydrogen standard leak.

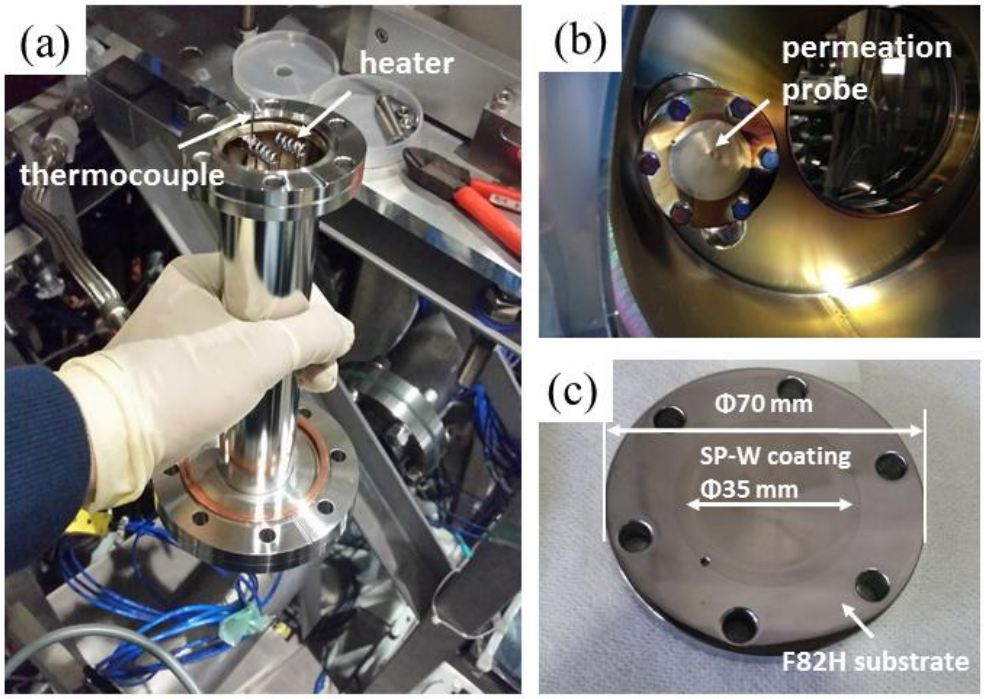

Figure 7.4 (a) The permeation probe showing the position of resistive heater and thermocouple, (b) a picture of the probe fixed in QUEST chamber and (c) the SP-W coated F82H permeation sample used in this work.

Shown in figure 7.4 are pictures of the permeation probe. A SP-W coated F82H sample is used which is prepared in the same dimensions as those commercially available conflat flanges with an outer diameter of 70 mm. The permeation area is 35 mm in diameter. The

thicknesses of SP-W coatings and F82H substrate are 0.5 μm and 0.25 mm, respectively. The F82H steel substrate is also cut from the F82H plates used in the JFT-2M tokamak at JAEA [151] and the SP-W coatings are prepared in the same way as those used in VEHICLE-1. Therefore, the surface conditions of the sample is the basically the same with those used in VEHICLE-1 (as shown in figure 7.5).

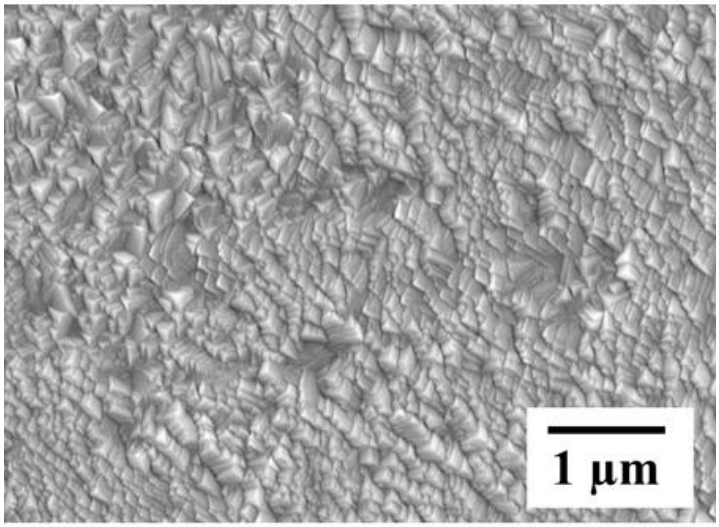

Figure 7.5 A SEM image of the surface of the SP-W coated F82H sample used in QUEST.

7.3 Results and discussion

7.3.1 Hydrogen PDP through SP-W coated F82H in QUEST

Figure 7.6 shows the time-evolution of hydrogen permeation data through the SP-W coated F82H membrane exposed to continuous wall conditioning discharges from shot #33474 to #33491 in QUEST. The plasma is produced by the 2.45 GHz RF system with an input power of 7.5 kW and the toroidal filed coil current is kept at 17 kA. This condition is same with that of the previous work [203]. Under these conditions, the steady-state

permeation flux for the SP-W coated F82H membrane has been measured to be ~2.1 × 10^{13} H/cm^2/s at 300 ℃.

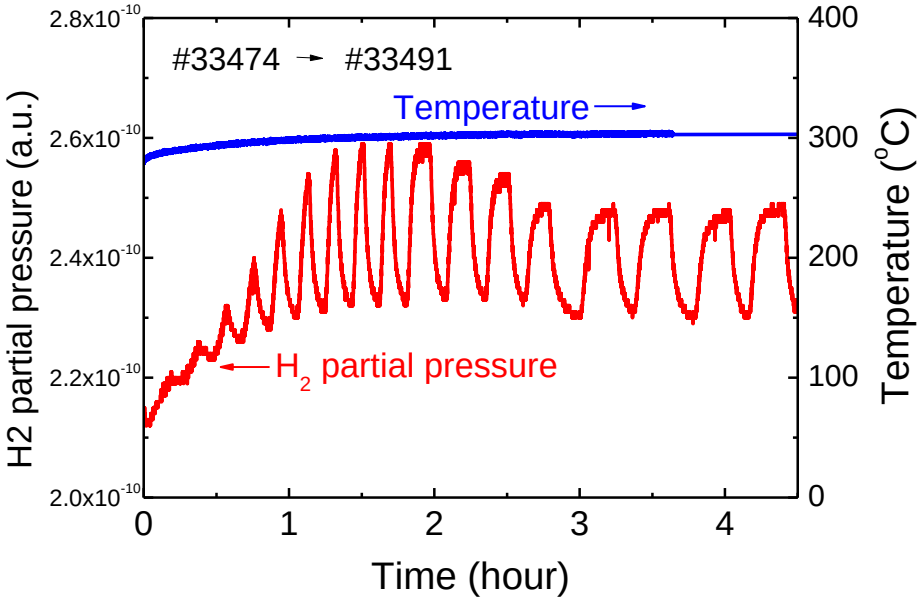

Figure 7.6 Hydrogen permeation through SP-W coated F82H at the temperature of 300 ℃ in QUEST (from shot #33474 to #33491). The thicknesses of SP-W coatings and F82H substrate are 0.5 μm and 0.25 mm, respectively.

In our previous work [203], the steady-state permeation flux was measured to be ~2.4 × 10^{13} H/cm^2/s at 270 ℃ using a 0.2 mm thick bare F82H membrane. Notice, however, that there was no radiation shield during that QUEST campaign. Therefore, to evaluate the effects of the radiation shield on hydrogen permeation, some calibration data are necessary. Shown in figure 7.7 are the radial profiles of hydrogen incident flux (Γ_{inc}) measured by a reciprocate PdCu permeation probe (indicated as PP8 in figure 7.3(a)) and ion flux (Γ_{ion}) measured by a reciprocate Langmuir probe (indicated as RLP in figure 7.3(a)) [207]. The PdCu membrane is selected for the probe calibration system from favorable viewpoints including the faster response time, wider permeation regime, and higher sensitivity

independent of the incident hydrogen flux. The characteristics of the PdCu permeation probe have already been experimentally investigated by Onaka et al. [208]. It has been found that hydrogen permeation through PdCu membrane is limited by the surface recombination process, in which case the steady-state permeation flux is proportional to the implantation (incident) flux.

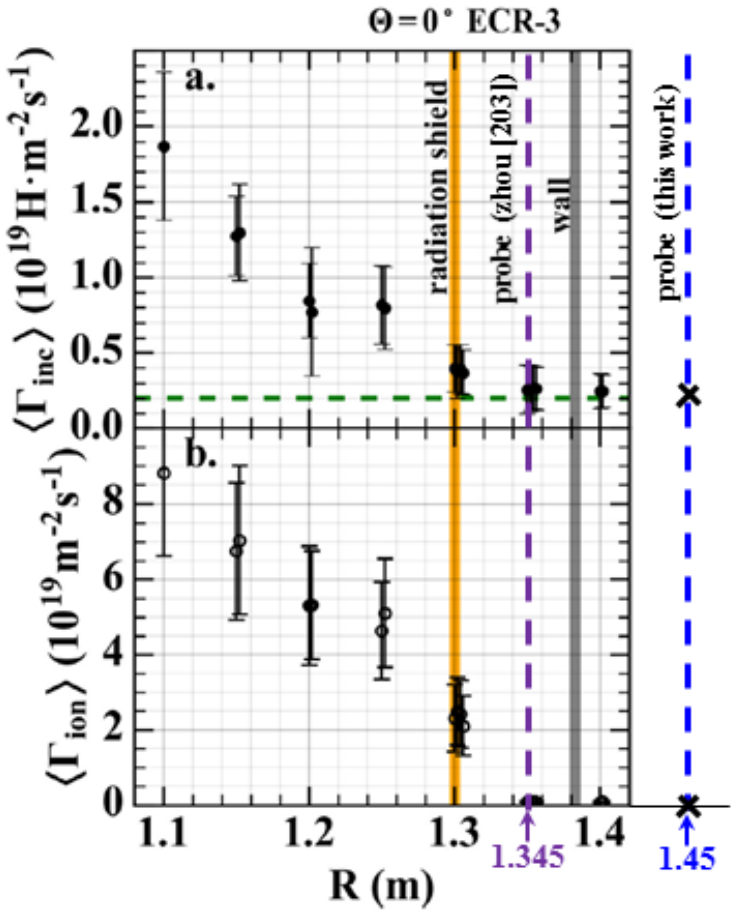

Figure 7.7 Radial profiles of hydrogen incident flux (Γ_{inc}) by a reciprocate PdCu permeation probe (indicated as PP8 in figure 7.3(a)) and ion flux (Γ_{ion}) by a reciprocate Langmuir probe in QUEST (indicated as RLP in figure 7.3(a)) (reedit from [207]).

In QUEST, two regions, i.e., the plasma region and inside the closed port section, are separated by the radiation shield at R = 1.3 m (as shown in figure 7.7). For R < 1.3 m, both Γ_{inc} and Γ_{ion} are smoothly increasing towards the slab plasma. The radial scale lengths and the relative radial profiles of Γ_{inc} and Γ_{ion} are consistent with each other, while a factor of 4-5 difference is shown. It should be noted that these radial profiles inside the plasma side reflect the radially diffusing plasma profile well. There are steep gradients in both Γ_{inc} and Γ_{ion} near R = 1.3 m, indicating that the diffusing plasma is terminated by the radiation shield around the torus. For R > 1.3 m, the Γ_{inc} profile is almost constant, ~0.2×10^{19} H/m^2/s, while Γ_{ion} immediately becomes zero. Thus, it can be concluded the ion flux is dominate in the plasma region (R < 1.3 m) but the atomic hydrogen plays an essential role on the permeation behind the radiation shield or inside the closed port section (R > 1.3 m).

In the present work, the permeation membrane is 15 cm recessed from the radiation shield. In the previous work, however, the membrane is 3.5 cm away from the outboard wall, the positions of the probes are shown in figure 7.7. It can be seen that without the radiation shield, the hydrogen incident flux Γ_{inc} measured by the PdCu probe is extrapolated to be ~0.8×10^{19} H/m^2/s at R = 1.345 m, while with the radiation shield, Γ_{inc} at R = 1.345 is reduced by a factor of ~4 to be the value of ~0.2×10^{19} H/m^2/s. For hydrogen PDP taken in the RD regime (recombination-limited hydrogen release from the upstream surface and the diffusion-limited hydrogen release from the downstream surface), the permeation flux J_+ (atoms/cm^2/s) is proportional to the square-root of implantation (incident) flux J_0 (atoms/cm^2/s) and inversely proportional to the membrane thickness L (cm):

$$J_+ = \frac{D}{L}\sqrt{\frac{J_0}{K_r}}\ , \tag{7.1}$$

where D (cm^2/s) is the diffusion coefficient. K_r (cm^4/s) is the hydrogen recombination coefficient on the plasma-facing surface.

To the first order of approximation, the membrane temperature (300 ℃ in this work and 270 ℃ in [203]) effects on D is negligible [181]. The membrane temperature effects

on J_+ for SP-W coated F82H has been shown in [191], J_+ has been found to decrease with increasing the temperature, which means that J_+ is supposed to be even higher than the present measured value for the membrane temperature at 270 ℃ during experiments. Therefore, from Eq. (7.1) one obtains that the permeation flux will be reduced at least by a factor of ~2.5 taking into account the effects of the incident flux and membrane thickness. The steady-state hydrogen permeation flux has been re-estimated to be ~5.3×10^{13} H/cm^2/s at 300 ℃ in the present work.

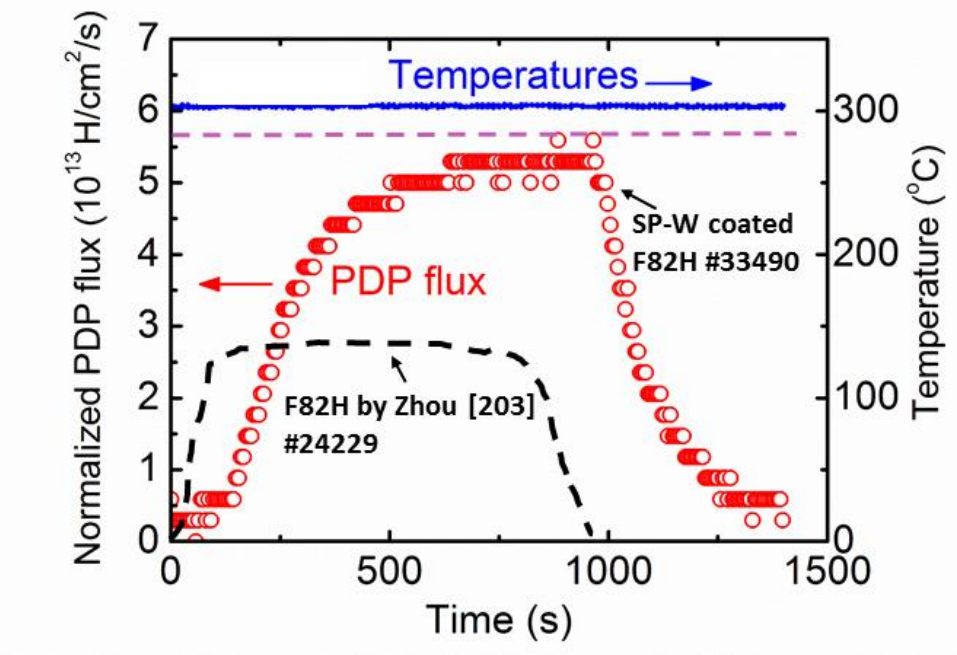

Figure 7.8 Comparison of hydrogen PDP through SP-W coated F82H and bare F82H membranes in 910 s steady-state wall conditioning discharges. The thicknesses of SP-W coatings and F82H substrate are 0.5 μm and 0.25 mm, respectively.

Shown in figure 7.8 is a comparison of hydrogen PDP through the SP-W coated F82H and bare F82H membranes. The normalized PDP flux means that the different incident flux

due to the radiation shield and the different membrane thickness have been considered so as to compare with the data in [203]. It can be seen that the permeation flux for bare F82H reaches steady-state within 100 s, while it take ~700 s for SP-W coated F82H. It is believed to be attributed to the trapping effects of W coatings on hydrogen migration which have already discussed in the previous chapter. The steady-state permeation flux through SP-W coated F82H in QUEST is about a factor of 2 higher than that through bare F82H, i.e., SP-W coatings enhance hydrogen PDP, which is in agreement with the data taken in the linear plasma facility VEHICLE-1 except that the increase in permeation flux is relatively smaller. In VEHICLE-1, the permeation flux through SP-W coated F82H is about one order of magnitude higher than that through bare F82H in the temperature range of 300-550 ℃ [191]. The difference could be due to the different particle bombarding energies in QUEST (no DC bias) and VEHICLE-1 (DC bias, -100 V). Besides, the permeation flux measured in QUEST is mainly a result of atomic hydrogen permeation, which is different from the plasma condition in VEHICLE-1. Nevertheless, further investigations are still needed to address this issue.

7.3.2 Effect of gas fueling rate

Shown in figure 7.9 is the hydrogen pressure dependence of PDP flux and time-integrated H_α intensity for the permeation probe at ~300 ℃ in QUEST. Hydrogen pressure is controlled by the gas fueling rate. It indicates that in the current range of hydrogen pressure, the PDP flux increases with increasing hydrogen pressure. The time-integrated H_α intensity, however, decreases with increasing hydrogen pressure which is assumably due to the decrease of the plasma temperature.

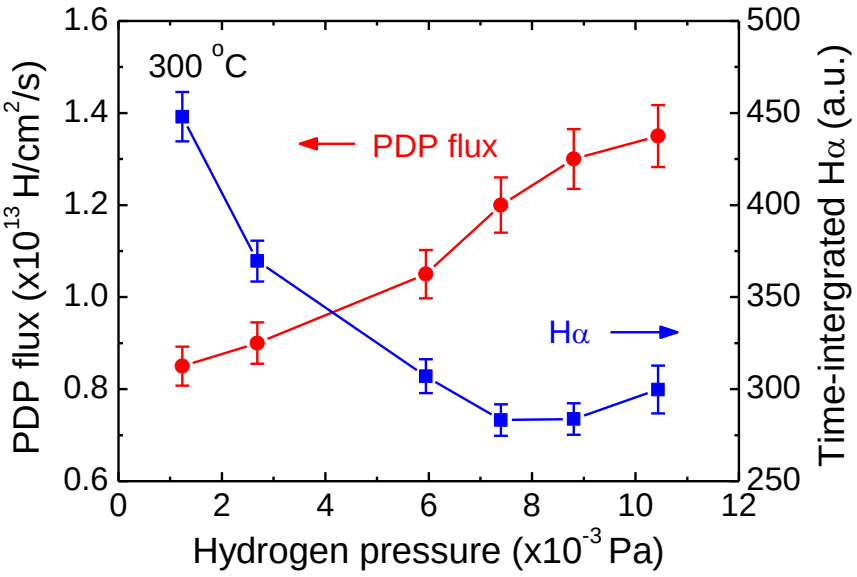

Figure 7.9 Hydrogen pressure dependence of PDP flux and time-integrated H_α intensity for SP-W coated F82H membrane at ~300 ℃ in QUEST.

7.4 Summary

Hydrogen PDP flux measurements have been conducted in the QUEST spherical tokamak for SP-W coated F82H membrane and the present data has been compared with our previous results for bare F82H membrane. A much longer PDP breakthrough time and higher steady-state permeation flux have been found for SP-W coated F82H than that of bare F82H. It is concluded that SP-W coatings enhance hydrogen PDP not only in the VEHICLE-1 linear plasma device but also in the QUEST spherical tokamak.

Chapter 8

Summary and implications to reactors design

8.1 Summary

The first wall is defined as the plasma-facing surfaces of the blanket units, whereby hydrogen isotopes flow in and out in two opposite directions simultaneously through the first wall: in one direction by plasma-driven permeation (PDP) and in the other direction by gas-driven permeation (GDP). In this PhD thesis work, hydrogen isotopes permeation behavior through the first wall of a magnetic fusion power reactor has been studied.

A steady-state laboratory-scale plasma device VEHICLE-1 has been used to investigate the bi-directional hydrogen isotopes permeation by PDP and GDP under conditions to be seen in the first wall environment. The hydrogen transport parameters data taken for α-Fe have been found to be in good agreement with the literature data, which means that the experimental setup in VEHICLE-1 is valid for the evaluation of other first wall candidate materials.

Both GDP and PDP of hydrogen isotopes through F82H have been found to be diffusion-limited. The hydrogen and deuterium transport parameters such as permeability, diffusivity, solubility and surface recombination coefficient have been successfully measured for F82H. In particular, the surface recombination coefficient of deuterium on F82H has been experimentally measured for the first time. Isotopic effects on hydrogen transport have been discussed. Simultaneous bi-directional hydrogen isotopes (H/D) plasma- and gas-driven permeation has been demonstrated experimentally for the first time under controlled experimental conditions. Hydrogen GDP has been found to take place in the opposite direction of deuterium PDP.

Hydrogen GDP and PDP experiments have been conducted for VPS-W and SP-W coated F82H membranes. VPS-W coatings have been found to be porous and have an open system of connected pores. The main effect of the VPS-W coatings on hydrogen permeation is to reduce the incoming flux at the W/F82H interface owing to pore diffusion in the coating and to reduce the effective surface area for hydrogen dissolution in the substrate.

SP-W coatings have a dense and pore-free structure. It has been found that SP-W coatings reduce GDP fluxes but tend to enhance PDP which has been observed not only in the VEHICLE-1 facility but also in the QUEST spherical tokamak. Characterization analyses indicate that microstructure and surface properties of the coatings significantly alter PDP fluxes. Surface recombination is an important process determining the PDP flux. Transport parameters including diffusivity, permeability, solubility and surface recombination coefficient have been evaluated for SP-W coatings. The permeability for SP-W is close to the literature data for bulk polycrystalline W. However, the effective diffusivity and solubility are different from the literature data by several orders of magnitude, indicating that the traps influence on hydrogen migration in W. Static deuterium retention has been measured by TDS. Increased deuterium retention in SP-W coated F82H has been observed compared with that in bare F82H. SIMS depth profile shows a good agreement with the retention data and exhibits a sign of "uphill diffusion" of deuterium in the W/F82H bi-layer structure.

8.2 Implications to reactors design

This PhD thesis work has established some fundamental knowledge databases for fusion reactors design, which makes a contribution to magnetic fusion research in the field of fusion engineering. Using these data and methods, it is possible to analyze the hydrogen isotopes permeation behavior through the first wall under some of the reactor-relevant conditions. From the viewpoint of bi-directional hydrogen isotopes permeation of a future fusion reactor, two implications of this PhD thesis work to reactors design are listed (as shown in figure 8.1):

(1) VPS-W and SP-W coatings might be overlaid protecting F82H, so that bi-directional hydrogen permeation would be reduced.

(2) One can also combine VPS-W coatings on the plasma-facing side and Al_2O_3 (Er_2O_3 etc.) insulator, which is intended to reduce magnetohydrodynamic (MHD) drag, on the breeding blanket side to reduce the bi-directional permeation. Since the Al_2O_3 is an

efficient permeation barrier for hydrogen isotopes [174] that one might use VPS-W coatings as an armor to protect the first wall from the viewpoint of energetic ion sputtering.

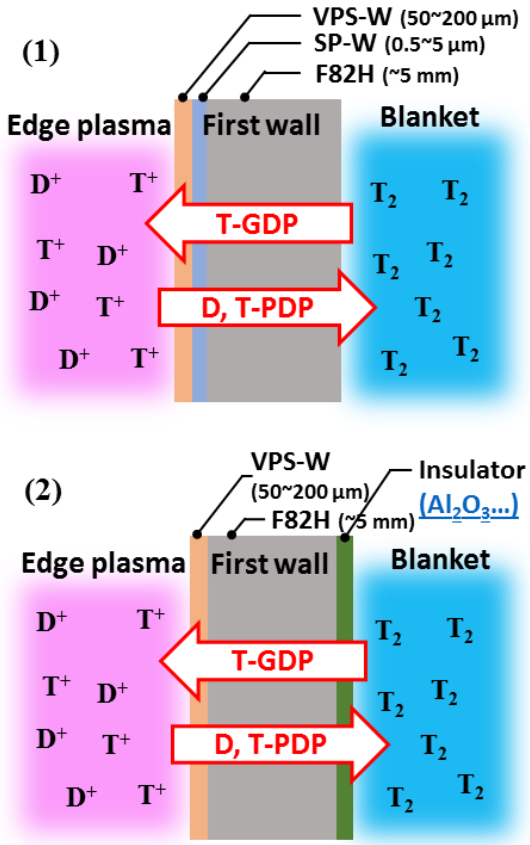

Figure 8.1 Applications of tungsten coatings in fusion reactors.

References

[1] J. Wesson, *Tokamaks*, 3rd edition, Oxford University Press, 2004.

[2] M. Kikuchi, *Frontiers in fusion research: physics and fusion*, Springer Science & Business Media, 2011.

[3] K. Miyamoto, *Plasma Physics for Controlled Fusion*, 2nd edition, Springer, 2016; Vol. 92.

[4] https://en.wikipedia.org/wiki/Nuclear_cross_section.

[5] J. P. Freidberg, *Plasma physics and fusion energy*, Cambridge university press, 2008.

[6] M. Kikuchi, K. Lackner, M. Q. Tran, *Fusion physics*, 2012.

[7] F. F. Chen, *An indispensable truth: how fusion power can save the planet*, Springer Science & Business Media, 2011.

[8] J. D. Lawson, *Some criteria for a power producing thermonuclear reactor*, Proceedings of the Physical Society. Section B **70** (1957) 6.

[9] H. Yamada, Fusion Energy. In *Handbook of Climate Change Mitigation*, Chen, W.-Y.; Seiner, J.; Suzuki, T.; Lackner, M., Eds. Springer US: New York, 2012; pp 1183-1215.

[10] https://www.euro-fusion.org/jet/.

[11] http://www.jt60sa.org/b/index.htm.

[12] https://fusion.gat.com/global/DIII-D.

[13] http://www.ipp.mpg.de/16195/asdex.

[14] J. Li, *Recent Progress on EAST*, Fusion Science and Technology **64** (2013) 417-423.

[15] G. Lee, M. Kwon, C. Doh, B. Hong, K. Kim, et al., *Design and construction of the KSTAR tokamak*, Nuclear Fusion **41** (2001) 1515.

[16] K. Hanada, K. Sato, H. Zushi, K. Nakamura, M. Sakamoto, et al., *Steady-state operation scenario and the first experimental result on QUEST*, Plasma and Fusion Research **5** (2010) S1007-S1007.

[17] A. Komori, H. Yamada, S. Imagawa, O. Kaneko, K. Kawahata, et al., *Goal and achievements of large helical device project*, Fusion Science and Technology **58** (2010) 1-11.

[18] M. Gasparotto, *W7-X progress*, Fusion Science and Technology **47** (2005) 339-344.

[19] http://www.iter.org/.

[20] J. F. Ahearne, R. Fonck, *Burning plasma: bringing a star to earth*, National Academies Press, 2004.

[21] S. Tanaka, H. Takatsu, *Japanese perspective of fusion nuclear technology from ITER to DEMO*, Fusion Engineering and Design **83** (2008) 865-869.

[22] Y. Shimomura, *ITER towards the construction*, Fusion Engineering and Design **74** (2005) 9-16.

[23] E. Gibne, *Five-year Delay Would Spell End of ITER*, Nature Publishing Group **31** (2014).

[24] K. Tobita, S. Nishio, M. Enoeda, H. Kawashima, G. Kurita, et al., *Compact DEMO, SlimCS: design progress and issues*, Nuclear Fusion **49** (2009) 075029.

[25] D. Maisonnier, I. Cook, S. Pierre, B. Lorenzo, G. Luciano, et al., *DEMO and fusion power plant conceptual studies in Europe*, Fusion Engineering and Design **81** (2006) 1123-1130.

[26] F. Najmabadi, A. Abdou, L. Bromberg, T. Brown, V. Chan, et al., *The ARIES-AT advanced tokamak, advanced technology fusion power plant*, Fusion Engineering and Design **80** (2006) 3-23.

[27] A. Sagara, O. Mitarai, S. Imagawa, T. Morisaki, T. Tanaka, et al., *Conceptual design activities and key issues on LHD-type reactor FFHR*, Fusion Engineering and Design **81** (2006) 2703-2712.

[28] Y. T. Song, S. T. Wu, J. G. Li, B. N. Wan, Y. X. Wan, et al., *Concept design of CFETR tokamak machine*, IEEE Transactions on Plasma Science **42** (2014) 503-509.

[29] B. Wan, S. Ding, J. Qian, G. Li, B. Xiao, et al., *Physics design of CFETR: determination of the device engineering parameters*, IEEE Transactions on Plasma Science **42** (2014) 495-502.

[30] Y. K. M. Peng, *Fusion nuclear science facility (FNSF) before upgrade to component test facility (CTF)*, Fusion Science and Technology **60** (2011) 441-448.

[31] J. D. Lindl, P. Amendt, R. L. Berger, S. G. Glendinning, S. H. Glenzer, et al., *The physics basis for ignition using indirect-drive targets on the National Ignition Facility*, Physics of Plasmas (1994-present) **11** (2004) 339-491.

[32] S. Pfalzner, *An introduction to inertial confinement fusion*, CRC Press, 2006.

[33] G. H. Miller, E. I. Moses, C. R. Wuest, *The National Ignition Facility: enabling fusion ignition for the 21st century*, Nuclear Fusion **44** (2004) S228.

[34] O. Hurricane, D. Callahan, D. Casey, P. Celliers, C. Cerjan, et al., *Fuel gain exceeding unity in an inertially confined fusion implosion*, Nature **506** (2014) 343-348.

[35] H. Azechi, K. Mima, S. Shiraga, S. Fujioka, H. Nagatomo, et al., *Present status of fast ignition realization experiment and inertial fusion energy development*, Nuclear Fusion **53** (2013) 104021.

[36] H. Azechi, K. Mima, Y. Fujimoto, S. Fujioka, H. Homma, et al., *Plasma physics and laser development for the Fast-Ignition Realization Experiment (FIREX) Project*, Nuclear Fusion **49** (2009) 104024.

[37] H. Azechi, *The FIREX program on the way to inertial fusion energy*, Journal of Physics: Conference Series **112** (2008) 012002.

[38] W. M. Stacey, *Fusion: an introduction to the physics and technology of magnetic confinement fusion*, John Wiley & Sons, 2010.

[39] T. Tanabe, *Tritium issues to be solved for establishment of a fusion reactor*, Fusion Engineering and Design **87** (2012) 722-727.

[40] A. Sagara, *NIFS-MEMO-64*, (2013).

[41] K. Shiba, A. Hishinuma, A. Tohyama, K. Masamura *Properties of low activation ferritic steel F82H IEA heat. Interim report of IEA round-robin tests (1)*; Japan Atomic Energy Research Institute: 1997.

[42] T. Muroga, *Vanadium alloys for fusion blanket applications*, Materials transactions **46** (2005) 405-411.

[43] T. Dolan, G. Butterworth, *Vanadium recycling*, Fusion Technology **26** (1994).

[44] G. Kalinin, W. Gauster, R. Matera, A.-A. Tavassoli, A. Rowcliffe, et al., *Structural materials for ITER in-vessel component design*, Journal of Nuclear Materials **233** (1996) 9-16.

[45] N. Baluc, R. Schäublin, P. Spätig, M. Victoria, *On the potentiality of using ferritic/martensitic steels as structural materials for fusion reactors*, Nuclear Fusion **44** (2003) 56.

[46] V. Ghetta, D. Gorse, D. Mazière, V. Pontikis, *Materials Issues for Generation IV Systems: Status, Open Questions and Challenges,* Springer Science & Business Media, 2008.

[47] B. Raj, M. Vijayalakshmi, *Ferritic steels and advanced ferritic-martensitic steels,* Comprehensive Nuclear Materials, Elsevier, 2012.

[48] A. Hishinuma, A. Kohyama, R. Klueh, D. Gelles, W. Dietz, et al., *Current status and future R&D for reduced-activation ferritic/martensitic steels*, Journal of Nuclear Materials **258** (1998) 193-204.

[49] Y. Ueda, K. Tobita, Y. Katoh, *PSI issues at plasma facing surfaces of blankets in fusion reactors*, Journal of Nuclear Materials **313** (2003) 32-41.

[50] A.-A. F. Tavassoli, *Present limits and improvements of structural materials for fusion reactors–a review*, Journal of Nuclear Materials **302** (2002) 73-88.

[51] A. Sagara, H. Yamanishi, T. Uda, O. Motojima, T. Kunugi, et al., *Studies on Flibe blanket designs in helical reactor FFHR*, Fusion Technology **39** (2001) 753-757.

[52] L. Giancarli, M. Ferrari, M. Fütterer, S. Malang, *Candidate blanket concepts for a European fusion power plant study*, Fusion Engineering and Design **49** (2000) 445-456.

[53] S. Konishi, S. Nishio, K. Tobita, D. The, *DEMO plant design beyond ITER*, Fusion Engineering and Design **63** (2002) 11-17.

[54] Y. Gohar, S. Majumdar, D. Smith, *High power density self-cooled lithium–vanadium blanket*, Fusion Engineering and Design **49** (2000) 551-558.

[55] C. Wong, C. Baxi, R. Cerbone, E. Cheng, E. Reis, *A helium-cooled blanket design of the low aspect ratio reactor,* Fusion Engineering and Design **48** (2000) 389-396.

[56] H. Golfier, G. Aiello, M. Fütterer, A. Gasse, L. Giancarli, et al., *Performance of the TAURO blanket system associated with a liquid-metal cooled divertor*, Fusion Engineering and Design **49** (2000) 559-565.

[57] L. Boccaccini, U. Fischer, S. Gordeev, S. Malang, *Advanced helium cooled pebble bed blanket with SiC f/SiC as structural material*, Fusion Engineering and Design **49** (2000) 491-497.

[58] R. Hawryluk, K. Bol, N. Bretz, D. Dimock, D. Eames, et al., *The effect of current profile evolution on plasma-limiter interaction and the energy confinement time*, Nuclear Fusion **19** (1979) 1307.

[59] H. Nakamura, T. Ando, H. Yoshida, S. Niikura, T. Nishitani, et al., *Divertor experiment on particle and energy control in neutral beam heated JT-60 discharges*, Nuclear Fusion **28** (1988) 43.

[60] T. Group, *TFR, the tokamak of Fontenay-aux-Roses*, Nuclear Fusion **25** (1985) 1025.

[61] B. Lipschultz, D. Pappas, B. LaBombard, J. Rice, D. Smith, et al., *A study of molybdenum influxes and transport in Alcator C-Mod*, Nuclear Fusion **41** (2001) 585.

[62] F. Alladio, F. Group, *Results from the Frascati tokamak FT*, Nuclear Fusion **25** (1985) 1069.

[63] D. Smith, *Physical sputtering model for fusion reactor first-wall materials*, Journal of Nuclear Materials **75** (1978) 20-31.

[64] P. Andrew, D. Brennan, J. Coad, J. Ehrenberg, M. Gadeberg, et al., *Tritium recycling and retention in JET*, Journal of Nuclear Materials **266** (1999) 153-159.

[65] V. Philipps, *Tungsten as material for plasma-facing components in fusion devices*, Journal of Nuclear Materials **415** (2011) S2-S9.

[66] T. Otsuka, T. Tanabe, K. Tokunaga, *Retention and release mechanisms of tritium loaded in plasma-sprayed tungsten coatings by plasma exposure*, Journal of Nuclear Materials **438** (2013) S1048-S1051.

[67] I. Smid, M. Akiba, G. Vieider, L. Plöchl, *Development of tungsten armor and bonding to copper for plasma-interactive components*, Journal of Nuclear Materials **258** (1998) 160-172.

[68] D. Post, R. Behrisch, *Physics of plasma-wall interactions in controlled fusion*, Plenum Press, New York, 1984.

[69] K.-U. Riemann, *The Bohm criterion and sheath formation*, Journal of Physics D: Applied Physics **24** (1991) 493.

[70] F. C. Francis, *Introduction to Plasma Physics and Controlled Fusion*, Plasma Physics (1984).

[71] P. C. Stangeby, *The plasma boundary of magnetic fusion devices*, Institute of Physics Publishing Bristol, 2000; Vol. 224.

[72] R. Behrisch, G. Federici, A. Kukushkin, D. Reiter, *Material erosion at the vessel walls of future fusion devices*, Journal of Nuclear Materials **313** (2003) 388-392.

[73] B. LaBombard, M. Umansky, R. Boivin, J. Goetz, J. Hughes, et al., *Cross-field plasma transport and main-chamber recycling in diverted plasmas on Alcator C-Mod*, Nuclear Fusion **40** (2000) 2041.

[74] Y. Hirooka, H. Zhou, N. Ashikawa, T. Muroga, A. Sagara, *Plasma-and gas-driven hydrogen isotope permeation through the first wall of a magnetic fusion power reactor*, Fusion Science and Technology **64** (2013) 345-350.

[75] H. Zhou, Y. Hirooka, N. Ashikawa, T. Muroga, A. Sagara, *Hydrogen Plasma-Driven Permeation Through a Reduced Activation Ferritic Steel Alloy F82H*, Fusion Science and Technology **63** (2013) 361-363.

[76] R. Kerst, W. Swansiger, *Plasma driven permeation of tritium in fusion reactors*, Journal of Nuclear Materials **123** (1984) 1499-1510.

[77] R. Causey, R. Kerst, B. Mills, *The effect of surface composition on plasma driven permeation of deuterium through 304 stainless steel*, Journal of Nuclear Materials **123** (1984) 1547-1552.

[78] M. Takizawa, K. Kiuchi, M. Okamoto, Y. Fujii, *Surface condition effects on plasma driven permeation*, Journal of Nuclear Materials **248** (1997) 15-18.

[79] M. Takizawa, K. Kiuchi, H. Ishizuka, M. Okamoto, Y. Fujii, *Estimation of permeation probability in plasma driven permeation*, Fusion Engineering and Design **39** (1998) 923-928.

[80] R. Causey, M. Baskes, *Plasma-driven permeation of deuterium in nickel*, Journal of Nuclear Materials **145** (1987) 284-287.

[81] A. Busnyuk, Y. Nakamura, Y. Nakahara, H. Suzuki, N. Ohyabu, et al., *Membrane bias effects on plasma-driven permeation of hydrogen through niobium membrane*, Journal of Nuclear Materials **290** (2001) 57-60.

[82] R. Kerst, W. Swansiger, *Comparison of plasma and gas driven permeation of deuterium through titanium diboride*, Journal of Nuclear Materials **135** (1985) 77-81.

[83] A. Skovoroda, V. Svishchov, A. Spitsyn, V. Stolyarov, Y. M. Pustovoit, et al., *Plasma-driven superpermeation of hydrogen through Nb membranes: bulk effects*, Journal of Nuclear Materials **306** (2002) 232-240.

[84] S. Fukada, Y. Edao, S. Yamaguti, T. Norimatsu, *Tritium recovery system for Li–Pb loop of inertial fusion reactor*, Fusion Engineering and Design **83** (2008) 747-751.

[85] H. Zhou, Y. Hirooka, N. Ashikawa, T. Muroga, A. Sagara, *Gas-and plasma-driven hydrogen permeation through a reduced activation ferritic steel alloy F82H*, Journal of Nuclear Materials **455** (2014) 470-474.

[86] E. Serra, A. Perujo, G. Benamati, *Influence of traps on the deuterium behaviour in the low activation martensitic steels F82H and Batman*, Journal of Nuclear Materials **245** (1997) 108-114.

[87] E. Serra, G. Benamati, *Hydrogen behaviour in aged low activation martensitic steel F82H for fusion reactor applications*, Materials science and technology **14** (1998) 573-578.

[88] A. Pisarev, V. Shestakov, S. Kulsartov, A. Vaitonene, *Surface effects in diffusion measurements: deuterium permeation through Martensitic steel*, Physica Scripta **T94** (2001) 121-127.

[89] Y. N. Dolinsky, Y. N. Zouev, I. Lyasota, I. Saprykin, V. Sagaradze, *Permeation of deuterium and tritium through the martensitic steel F82H*, Journal of Nuclear Materials **307** (2002) 1484-1487.

[90] T. V. Kulsartov, K. Hayashi, M. Nakamichi, S. E. Afanasyev, V. P. Shestakov, et al., *Investigation of hydrogen isotope permeation through F82H steel with and without a ceramic coating of Cr_2O_3–SiO_2 including $CrPO_4$ (out-of-pile tests)*, Fusion Engineering and Design **81** (2006) 701-705.

[91] E. Serra, A. Perujo, *Influence of the surface conditions on permeation in the deuterium–MANET system*, Journal of Nuclear Materials **240** (1997) 215-220.

[92] T. Tanabe, Y. Yamanishi, K. Sawada, S. Imoto, *Hydrogen transport in stainless steels*, Journal of Nuclear Materials **123** (1984) 1568-1572.

[93] R. Miller, J. Hudson, G. Ansell, *Permeation of hydrogen through alpha iron*, Metallurgical Transactions A **6** (1975) 117-121.

[94] N. Quick, H. Johnson, *Hydrogen and deuterium in iron, 49–506 C*, Acta Metallurgica **26** (1978) 903-907.

[95] R. Frauenfelder, *Solution and diffusion of hydrogen in tungsten*, Journal of Vacuum Science and Technology **6** (1969) 388-397.

[96] A. P. Zakharov, V. M. Sharapov, E. I. Evko, *Hydrogen permeability of polycrystalline and monocrystalline molybdenum and tungsten*, Materials Science **9** (1973) 149-153.

[97] F. Liu, H. Zhou, X. Li, Y. Xu, Z. An, et al., *Deuterium gas-driven permeation and subsequent retention in rolled tungsten foils*, Journal of Nuclear Materials **455** (2014) 248-252.

[98] T. Tokunaga, H. Watanabe, N. Yoshida, T. Nagasaka, R. Kasada, et al., *Development of high-grade VPS-tungsten coatings on F82H reduced activation steel*, Journal of Nuclear Materials **442** (2013) S287-S291.

[99] H. Kim, J. El-Awady, V. Gupta, N. Ghoniem, S. Sharafat, *Interface strength measurement of tungsten coatings on F82H substrates*, Journal of Nuclear Materials **386** (2009) 863-865.

[100] H. Tanigawa, K. Ozawa, Y. Morisada, S. Noh, H. Fujii, *Modification of vacuum plasma sprayed tungsten coating on reduced activation ferritic/martensitic steels by friction stir processing*, Fusion Engineering and Design **98** (2015) 2080-2084.

[101] Y. Yahiro, M. Mitsuhara, K. Tokunakga, N. Yoshida, T. Hirai, et al., *Characterization of thick plasma spray tungsten coating on ferritic/martensitic steel F82H for high heat flux armor*, Journal of Nuclear Materials **386** (2009) 784-788.

[102] T. Nagasaka, R. Kasada, A. Kimura, Y. Ueda, T. Muroga, *Theromophysical Properties and Microstructure of Plasma-Sprayed Tungsten Coating on Low Activation Materials*, Fusion Science and Technology **56** (2009) 1053-1057.

[103] Y. Kikuchi, I. Sakuma, D. Iwamoto, Y. Kitagawa, N. Fukumoto, et al., *Surface cracking and melting of different tungsten grades under transient heat and particle*

loads in a magnetized coaxial plasma gun, Journal of Nuclear Materials **438** (2013) S715-S718.

[104] T. Otsuka, T. Tanabe, K. Tokunaga, *Behaviour of tritium in plasma-sprayed tungsten coating on steel exposed to tritium plasma*, Physica Scripta **T145** (2011) 014035.

[105] T. Otsuka, T. Hoshihira, T. Tanabe, *Visualization of hydrogen depth profile by means of tritium imaging plate technique: determination of hydrogen diffusion coefficient in pure tungsten*, Physica Scripta **2009** (2009) 014052.

[106] R. A. Langley, J. Bohdansky, W. Eckstein, P. Mioduszewski, J. Roth, et al., *Data compendium for plasma-surface interactions*, Nuclear Fusion **24** (1984) S9.

[107] W. Möller, J. Roth, Implantation, retention and release of hydrogen isotopes in solids. In *Physics of plasma-wall interactions in controlled fusion*, Springer: 1986; pp 439-494.

[108] M. T. Robinson, I. M. Torrens, *Computer simulation of atomic-displacement cascades in solids in the binary-collision approximation*, Physical Review B **9** (1974) 5008.

[109] W. Eckstein, *IPP Report 9/132*, Max-Planck-Institut für Plasmaphysik, Garching, Germany (2002).

[110] Y. Yamamura, Y. Mizuno, *Low-energy sputterings with the Monte Carlo program ACAT*, Institute of Plasma Physics, Nagoya University (1985).

[111] J. Kawata, K. Ohya, *Ion backscattering and sputtering of plasma-irradiated carbon and tungsten surfaces in an oblique magnetic field*, Japanese journal of applied physics **34** (1995) 6237.

[112] F. Waelbroeck, I. Ali-Khan, K. J. Dietz, P. Wienhold, *Hydrogen solubilisation into and permeation through wall materials*, Journal of Nuclear Materials **85–86** (1979) 345-349.

[113] K. Wilson, M. Baskes, *Deuterium trapping in irradiated 316 stainless steel*, Journal of Nuclear Materials **76** (1978) 291-297.

[114] C. San Marchi, B. P. Somerday, S. L. Robinson, *Permeability, solubility and diffusivity of hydrogen isotopes in stainless steels at high gas pressures*, International Journal of Hydrogen Energy **32** (2007) 100-116.

[115] R. A. Causey, *Hydrogen isotope retention and recycling in fusion reactor plasma-facing components*, Journal of Nuclear Materials **300** (2002) 91-117.

[116] M. Baskes, *A calculation of the surface recombination rate constant for hydrogen isotopes on metals*, Journal of Nuclear Materials **92** (1980) 318-324.

[117] M. Pick, K. Sonnenberg, *A model for atomic hydrogen-metal interactions—application to recycling, recombination and permeation*, Journal of Nuclear Materials **131** (1985) 208-220.

[118] P. M. Richards, *Surface-limited hydrogen release and uptake in metals*, Journal of Nuclear Materials **152** (1988) 246-258.

[119] X. Sun, J. Xu, Y. Li, *Hydrogen permeation behaviour in austenitic stainless steels*, Materials Science and Engineering: A **114** (1989) 179-187.

[120] J. Crank, *The Mathematics of Diffusion, 2nd Edition*, Clarendon Press Oxford, London, 1975.

[121] M. A. V. Devanathan, Z. Stachurski, *The adsorption and diffusion of electrolytic hydrogen in palladium*, Proc. R. Soc. Lond. A **270** (1962) 90-102.

[122] I. Ali-Khan, K. Dietz, F. Waelbroeck, P. Wienhold, *The rate of hydrogen release out of clean metallic surfaces*, Journal of Nuclear Materials **76** (1978) 337-343.

[123] A. Pisarev, A. Bacherov, *Hydrogen gas driven permeation through asymmetric membranes in diffusion limited and surface limited regimes: Interplay between analytical and numerical calculations*, Physica Scripta **2004** (2004) 124.

[124] E. Marenkov, I. Tsvetkov, A. Pisarev, *Hydrogen permeability through sandwich membranes*, Bulletin of the Russian Academy of Sciences: Physics **74** (2010) 245-251.

[125] P. J. McGuiness, M. Čekada, V. Nemanič, B. Zajec, A. Rečnik, *Hydrogen permeation through TiAlN-coated Eurofer '97 steel*, Surface and Coatings Technology **205** (2011) 2709-2713.

[126] N. Takano, Y. Murakami, F. Terasaki, *Hydrogen diffusion in a thin film of Pd, Ni and Cu deposited on iron*, Scripta metallurgica et materialia **32** (1995) 401-406.

[127] A. Mezin, J. Lepage, P. Abel, *An analytical solution for non-steady-state diffusion through thin films*, Thin Solid Films **272** (1996) 124-131.

[128] R. Ash, R. Barrer, D. Palmer, *Diffusion in multiple laminates*, British Journal of Applied Physics **16** (1965) 873.

[129] D. Schultheiß, *Permeation barrier for lightweight liquid hydrogen tanks*, Ph.D. thesis, Universität Augsburg, Augsburg, Germany (2007).

[130] B. L. Doyle, *A simple theory for maximum h inventory and release: A new transport parameter*, Journal of Nuclear Materials **111–112** (1982) 628-635.

[131] D. K. Brice, B. Doyle, *Steady state hydrogen transport in solids exposed to fusion reactor plasmas: part I: theory*, Journal of Nuclear Materials **120** (1984) 230-244.

[132] D. K. Brice, *Steady state hydrogen transport in solids exposed to fusion reactor plasmas, part III: Isotope effects*, Journal of Nuclear Materials **123** (1984) 1531-1535.

[133] G. Longhurst *TMAP7: Tritium Migration Analysis Program, User Manual, Idaho National Laboratory*; INEEL/EXT-04-02352: 2004.

[134] Y. Hirooka, H. Ohgaki, Y. Ohtsuka, M. Nishikawa, *A new versatile facility: Vehicle-1 for innovative PFC concepts evaluation and its first experiments on hydrogen recycling from solid and liquid lithium*, Journal of Nuclear Materials **337–339** (2005) 585-589.

[135] M. A. Lieberman, A. J. Lichtenberg, *Principles of plasma discharges and materials processing*, second edtion, John Wiley & Sons, 2005.

[136] A. J. Dempster, *New methods in mass spectroscopy*, Proceedings of the American Philosophical Society **75** (1935) 755-767.

[137] P. H. Dawson, *Quadrupole mass spectrometry and its applications*, Elsevier, 2013.

[138] L. Johnson, E. Hinnov, *Ionization, recombination, and population of excited levels in hydrogen plasmas*, Journal of Quantitative Spectroscopy and Radiative Transfer **13** (1973) 333-358.

[139] Y. Hirooka, H. Fukushima, N. Ohno, S. Takamura, *Proof-of-principle experiments on the concept of moving-surface plasma-facing components—hydrogen recycling over a titanium-gettered rotating drum*, Fusion Engineering and Design **65** (2003) 413-421.

[140] R. L. Merlino, *Understanding Langmuir probe current-voltage characteristics*, American Journal of Physics **75** (2007) 1078-1085.

[141] F. F. Chen In *Langmuir probe diagnostics*, IEEE-ICOPS Meeting, Jeju, Korea, 2003.

[142] L. Conde, *An introduction to Langmuir probe diagnostics of plasmas*, Madrid: Dept. Física. ETSI Aeronáut ngenieros Aeronáuticos Universidad Politécnica de Madrid (2011) 1-28.

[143] A. T. Price, *Effects of Laser Light on Argon Plasma in a GEC rf Reference Cell*, Master thesis, The Graduate Faculty of Baylor University (2011).

[144] H. Zhou, *A study on bi-directional hydrogen isotopes permeation through the first wall of a magnetic fusion power reactor*, Ph.D. thesis, The Graduate University for Advanced Studies, Japan (2014).

[145] Y. Hirooka, S. Hosaka, M. Nishiura, Y. Ohtsuka, M. Nishikawa, *Helium ash removal by moving-surface plasma-facing components*, Journal of Nuclear Materials **363** (2007) 775-780.

[146] P. Redhead, *Thermal desorption of gases*, Vacuum **12** (1962) 203-211.

[147] P. Williams, *Secondary ion mass spectrometry*, Annual Review of Materials Science **15** (1985) 517-548.

[148] https://en.wikipedia.org/wiki/Secondary_ion_mass_spectrometry#cite_note-8.

[149] http://www.peabody-scientific.com/page14.html.

[150] F. Ghezzi, R. Caniello, D. Giubertoni, M. Bersani, A. Hakola, et al., *Deuterium depth profile quantification in a ASDEX Upgrade divertor tile using secondary ion mass spectrometry*, Applied Surface Science **315** (2014) 459-466.

[151] H. Kimura, M. Sato, H. Kawashima, N. Isei, K. Tsuzuki, et al., *Progress of advanced material tokamak experiment (AMTEX) program on JFT-2M*, Fusion Engineering and Design **56** (2001) 837-841.

[152] http://www.pvd-coating-kobelco.com/technologies/method_of_deposition.html.

[153] K. Forcey, I. Iordanova, D. Ross, *Investigation of structure dependence of diffusivity, solubility, and permeability of hydrogen in hot rolled low carbon steels*, Materials science and technology **6** (1990) 357-363.

[154] Y. Yamanishi, T. Tanabe, S. Imoto, *Hydrogen Permeation and Diffusion through Pure Fe, Pure Ni and Fe–Ni Alloys*, Transactions of the Japan institute of metals **24** (1983) 49-58.

[155] H. Birnbaum, C. Wert, *Diffusion of hydrogen in metals*, Berichte der Bunsengesellschaft für physikalische Chemie **76** (1972) 806-816.

[156] N. Quick, H. Johnson, *Permeation and diffusion of hydrogen and deuterium in 310 stainless steel, 472 K to 779 K*, Metallurgical Transactions A **10** (1979) 67-70.

[157] E. Serra, M. Kemali, A. Perujo, D. Ross, *Hydrogen and deuterium in Pd-25 pct Ag alloy: permeation, diffusion, solubilization, and surface reaction*, Metallurgical and Materials Transactions A **29** (1998) 1023-1028.

[158] B. L. Doyle, D. K. Brice, *Steady state hydrogen transport in solids exposed to fusion reactor plasmas, part II: Applications of theory*, Journal of Nuclear Materials **123** (1984) 1523-1530.

[159] I. Peñalva, G. Alberro, F. Legarda, R. Vila, C. Ortiz, *Influence of Cr content on the diffusive transport parameters and trapping of hydrogen in Fe alloys*, Fusion Engineering and Design **89** (2014) 1628-1632.

[160] K. Forcey, I. Iordanova, M. Yaneva, *The diffusivity and solubility of deuterium in a high chromium martensitic steel*, Journal of Nuclear Materials **240** (1997) 118-123.

[161] T. Ihli, T. Basu, L. Giancarli, S. Konishi, S. Malang, et al., *Review of blanket designs for advanced fusion reactors*, Fusion Engineering and Design **83** (2008) 912-919.

[162] V. Shestakov, A. Pisarev, V. Sobolev, S. Kulsartov, I. Tazhibaeva, *Gas driven deuterium permeation through F82H martensitic steel*, Journal of Nuclear Materials **307** (2002) 1494-1497.

[163] T. Tanabe, *Review of hydrogen retention in tungsten*, Physica Scripta **2014** (2014) 014044.

[164] T. Nagasaki, M. Saidoh, R. Yamada, H. Ohno, *Ion-driven permeation and surface recombination coefficient of deuterium for ion*, Journal of Nuclear Materials **202** (1993) 228-238.

[165] H. Zhou, Y. Hirooka, H. Zushi, A. Kuzmin, *Effects of surface conditions on the plasma-driven permeation behavior through a ferritic steel alloy observed in VEHICLE-1 and QUEST*, Journal of Nuclear Materials **463** (2015) 1066-1070.

[166] S. Myers, W. Wampler, *Trapping and surface permeation of deuterium in helium-implanted stainless steel*, Journal of Nuclear Materials **111** (1982) 579-583.

[167] O. Ogorodnikova, *Surface effects on plasma-driven tritium permeation through metals*, Journal of Nuclear Materials **290** (2001) 459-463.

[168] J. Winter, F. Waelbroeck, P. Wienhold, T. Schelske, *Permeation probes for the characterization of the atomic hydrogen flux to a tokamak wall*, Journal of Nuclear Materials **111** (1982) 243-247.

[169] Y. Hirooka, H. Zhou, *Laboratory Experiments and Modeling on Bi-Directional Hydrogen Isotopes Permeation Through the First Wall of a Magnetic Fusion DEMO Reactor*, Fusion Science and Technology **66** (2014) 63-69.

[170] R. Pitts, S. Carpentier, F. Escourbiac, T. Hirai, V. Komarov, et al., *A full tungsten divertor for ITER: physics issues and design status*, Journal of Nuclear Materials **438** (2013) S48-S56.

[171] A. Golubeva, A. Spitsyn, M. Mayer, D. Cherkez, T. Schwarz-Selinger, et al., *Gas-driven hydrogen permeation through tungsten-coated graphite*, Journal of Nuclear Materials **415** (2011) S688-S691.

[172] R. A. Anderl, R. J. Pawelko, M. R. Hankins, G. R. Longhurst, R. A. Neiser, *Hydrogen permeation properties of plasma-sprayed tungsten*, Journal of Nuclear Materials **212-215** (1994) 1416-1420.

[173] Y. Xu, Y. Hirooka, T. Nagasaka, J. Yagi, *Hydrogen gas-driven permeation through F82H steel coated with vacuum plasma-sprayed tungsten*, Plasma and Fusion Research **11** (2016) 2405064.

[174] E. Serra, G. Benamati, O. Ogorodnikova, *Hydrogen isotopes transport parameters in fusion reactor materials*, Journal of Nuclear Materials **255** (1998) 105-115.

[175] Y. Shen, Y. Mai, Q. Zhang, D. McKenzie, W. McFall, et al., *Residual stress, microstructure, and structure of tungsten thin films deposited by magnetron sputtering*, Journal of Applied Physics **87** (2000) 177-187.

[176] E. Vassallo, R. Caniello, M. Canetti, D. Dellasega, M. Passoni, *Microstructural characterisation of tungsten coatings deposited using plasma sputtering on Si substrates*, Thin Solid Films **558** (2014) 189-193.

[177] Y. Xu, *Research on the manufacturing of flat-type W/Cu PFMCs for EAST*, Master thesis, The University of Chinese Academy of Sciences, Hefei, China (2014).

[178] G. A. Esteban, A. Perujo, L. A. Sedano, K. Douglas, *Hydrogen isotope diffusive transport parameters in pure polycrystalline tungsten*, Journal of Nuclear Materials **295** (2001) 49-56.

[179] B. Zajec, V. Nemanič, C. Ruset, *Hydrogen diffusive transport parameters in W coating for fusion applications*, Journal of Nuclear Materials **412** (2011) 116-122.

[180] A. Turnbull, M. Carroll, D. Ferriss, *Analysis of hydrogen diffusion and trapping in a 13% chromium martensitic stainless steel*, Acta Metallurgica **37** (1989) 2039-2046.

[181] Y. Xu, Y. Hirooka, T. Nagasaka, *Bi-directional hydrogen isotopes permeation through a reduced activation ferritic steel F82H*, Fusion Engineering and Design https://doi.org/10.1016/j.fusengdes.2017.04.022 (2017).

[182] T. Otsuka, T. Ishihara, T. Tanabe, Physica Scripta **38** (2010) 014052.

[183] R. A. Oriani, *The diffusion and trapping of hydrogen in steel*, Acta Metallurgica **18** (1970) 147-157.

[184] R. Kirchheim, *Hydrogen solubility and diffusivity in defective and amorphous metals*, Progress in Materials Science **32** (1988) 261-325.

[185] M. I. Baskes, "DIFFUSE83" Sandia Rep. **SAND83-8231**.

[186] J. P. Hirth, *Effects of hydrogen on the properties of iron and steel*, Metallurgical Transactions A **11** (1980) 861-890.

[187] R. L. S. Thomas, D. Li, R. P. Gangloff, J. R. Scully, *Trap-governed hydrogen diffusivity and uptake capacity in ultrahigh-strength AERMET 100 steel*, Metallurgical and Materials Transactions A **33** (2002) 1991-2004.

[188] L. Raymond, *Hydrogen embrittlement: prevention and control,* ASTM International, 1988; Vol. 962.

[189] C. A. Wert, G. Alefeld, J. Völkl*, Topics in Applied Physics*, Hydrogen in Metals II **29** (1978) 305.

[190] R. P. Gangloff Corrosion Prevention and Control: Proceedings of the 33rd Sagamore Army Materials Research Conference. US Army Laboratory Command, Watertown, MA, 1986; pp 64-111.

[191] Y. Xu, Y. Hirooka, T. Nagasaka, N. Ashikawa, *Hydrogen Isotopes Plasma-Driven Permeation through Tungsten Coated Reduced Activation Ferritic Steel F82H*, Plasma and Fusion Research **12** (2017) 1205009.

[192] R. A. Anderl, D. F. Holland, G. R. Longhurst, *Hydrogen transport behavior of metal coatings for plasma-facing components*, Journal of Nuclear Materials **176–177** (1990) 683-689.

[193] R. Anderl, D. Holland, G. Longhurst, R. Pawelko, C. Trybus, et al., *Deuterium Transport and Trapping in Polycrystalline Tungsten a*, Fusion Science and Technology **21** (1992) 745-752.

[194] O. Ogorodnikova, J. Roth, M. Mayer, *Ion-driven deuterium retention in tungsten*, Journal of Applied Physics **103** (2008) 034902.

[195] V. K. Alimov, J. Roth, M. Mayer, *Depth distribution of deuterium in single-and polycrystalline tungsten up to depths of several micrometers*, Journal of Nuclear Materials **337** (2005) 619-623.

[196] R. G. Macaulay-Newcombe, M. Poon, A. A. Haasz, J. W. Davis In *Proceedings of Seventh International Workshop on Hydrogen Isotopes in Fusion Reactor Materials*, Sebasco Harbor Resort, Sebasco Harbor Resort, 20–21 May, 2004.

[197] A. Benninghoven, R. J. Colton, D. S. Simons, H. W. Werner, *Secondary ion mass spectrometry SIMS V: proceedings of the fifth international conference, Washington, DC, September 30–October 4, 1985,* Springer Science & Business Media, 2012; Vol. 44.

[198] A. A. Galuska, G. H. Morrison, *Matrix calibration for the quantitative analysis of layered semiconductors by secondary ion mass spectrometry*, Analytical Chemistry **55** (1983) 2051-2055.

[199] A. Tolstoguzov, U. Bardi, S. Chenakin, *Depth profiling using secondary ion mass spectrometry and sample current measurements*, Journal of Surface Investigation: X-ray, Synchrotron and Neutron Techniques **1** (2007) 734-740.

[200] G. Blaise, A. Nourtier, *Experimental and theoretical approaches to the ionization process in secondary-ion emission*, Surface Science **90** (1979) 495-547.

[201] D. S. Simons, J. E. Baker, C. A. Evans, *Evaluation of the local thermal equilibrium model for quantitative secondary ion mass spectrometric analysis*, Analytical Chemistry **48** (1976) 1341-1348.

[202] S. Horikoshi, J. Mochizuki, Y. Oya, T. Chikada, *Deuterium permeation and retention behaviors in erbium oxide-iron multilayer coatings*, Fusion Engineering and Design, http://dx.doi.org/10.1016/j.fusengdes.2017.03.123 (2017).

[203] H. Zhou, Y. Hirooka, H. Zushi, A. Kuzmin, *First Wall Particle Flux Measurements by an F82H Permeation Probe in QUEST*, Plasma and Fusion Research **9** (2014) 340541.

[204] http://www.triam.kyushu-u.ac.jp/.

[205] K. Hanada, H. Zushi, K. Nakamura, M. Sakamoto, I. Hiroshi, et al., *Steady-state operation scenario and the first experimental result on QUEST*, Plasma and Fusion Research **5** (2010) S1007-S1007.

[206] K. Hanada, H. Zushi, H. Idei, K. Nakamura, M. Ishiguro, et al., *Non-inductive start up of QUEST plasma by RF power*, Plasma Science and Technology **13** (2011) 307.

[207] A. Kuzmin, H. Zushi, I. Takagi, S. K. Sharma, M. Kobayashi, et al., *Spatial distribution of atomic and ion hydrogen flux and its effect on hydrogen recycling in long duration confined and non-confined plasmas*, Nuclear Materials and Energy, http://dx.doi.org/10.1016/j.nme.2017.03.027 (2017).

[208] M. Onaka, I. Takagi, T. Kobayashi, T. Sasaki, A. Kuzmin, et al., *Characteristic of a PdCu membrane as atomic hydrogen probe for QUEST*, Nuclear Materials and Energy **9** (2016) 104-108.

Publications

1. **Y. Xu**, Y. Hirooka, T. Nagasaka, J. Yagi, *Hydrogen Gas-driven Permeation through F82H Steel Coated with Vacuum Plasma-Sprayed Tungsten*, Plasma and Fusion Research, 11 (2016) 2405064.

2. **Y. Xu**, Y. Hirooka, T. Nagasaka, *Bi-directional hydrogen isotopes permeation through a reduced activation ferritic steel F82H*, Fusion Engineering and Design, DOI: 10.1016/j.fusengdes.2017.04.022 (2017).

3. **Y. Xu**, Y. Hirooka, T. Nagasaka, N. Ashikawa, *Hydrogen Isotopes Plasma-Driven Permeation through Tungsten Coated Reduced Activation Ferritic Steel F82H*, Plasma and Fusion Research, 12 (2017) 1205009.

4. **Y. Xu**, Y. Hirooka, N. Ashikawa, T. Nagasaka, *Hydrogen isotopes transport in sputter-deposited tungsten coatings*, Fusion Engineering and Design, DOI: 10.1016/j.fusengdes.2017.07.021 (2017).

5. **Y. Xu**, A. Kuzmin, Y. Hirooka, K. Hanada and the QUEST group, *Hydrogen Permeation through Sputter-Deposited Tungsten Coated F82H in QUEST*, Plasma and Fusion Research, 12 (2017) 1305038.

6. **Y. Xu**, Y. Hirooka, N. Ashikawa, T. Nagasaka, *Hydrogen isotopes plasma-driven permeation through sputter-deposited tungsten coated F82H*, IEEE Transactions on Plasma Science, under review (2017).